TopBP1 utilises a bipartite GINS binding mode to support genome replication

Matthew Day[*2,8+], Bilal Tetik[*1], Milena Parlak[*1], Yasser Almeida-Hernández[3,4], Markus Räschle[5], Farnusch Kaschani[6,7], Heike Siegert[1], Anika Marko[1], Elsa Sanchez-Garcia[3,4], Markus Kaiser[6,7], Isabel A. Barker[2], Laurence H. Pearl[2,9+], Antony W. Oliver[2+], Dominik Boos[1+]

[1], Molecular Genetics II, Center of Medical Biotechnology, University of Duisburg-Essen, Universitätsstraße 2-5, 45141 Essen, Germany

[2], Cancer Research UK DNA Repair Enzymes Group, Genome Damage and Stability Centre, School of Life Sciences, University of Sussex, Falmer, Brighton BN1 9RQ, UK

[3], Computational Bioengineering, Fakultät Bio- und Chemieingenieurwesen, Technical University Dortmund, Emil-Figge Str. 66, 44227 Dortmund, Germany

[4], Computational Biochemistry, Center of Medical Biotechnology, University of Duisburg-Essen, Universitätsstraße 2-5, 45141 Essen, Germany

[5], Molecular Genetics, Technical University Kaiserslautern, Paul-Ehrlich Straße 24, 67663 Kaiserslautern, Germany

[6], Analytics Core Facility Essen, Center of Medical Biotechnology, University of Duisburg-Essen, Universitätsstraße 2-5, 45141 Essen, Germany

[7] Chemical Biology, Center of Medical Biotechnology, University Duisburg-Essen, Fakultät Biologie, Essen, Germany

[8] School of Biological and Behavioural Sciences, Blizard Institute, Queen Mary University of London, London, E1 2AT, UK

[9] Division of Structural Biology, Institute of Cancer Research, Chester Beatty Laboratories, 237 Fulham Road, London SW1E 6BT, UK

[*] equal contribution
[+] corresponding author

Abstract

Activation of the replicative Mcm2-7 helicase by loading GINS and Cdc45 is crucial for replication origin firing, and as such for faithful genetic inheritance. Our biochemical and structural studies demonstrate that the helicase activator GINS interacts with TopBP1 through two separate binding surfaces, the first involving a stretch of highly conserved amino acids in the TopBP1-GINI region, the second a surface on TopBP1-BRCT4. The two surfaces bind to opposite ends of the A domain of the GINS subunit Psf1. Mutation analysis revealed that either surface is able to support TopBP1-GINS interaction, albeit with reduced affinity. Consistently, either surface is sufficient for replication origin firing in *Xenopus* egg extracts and becomes essential in the absence of the other. The TopBP1-GINS interaction appears sterically incompatible with simultaneous binding of DNA polymerase epsilon (Polε) to GINS when bound to Mcm2-7-Cdc45, although TopBP1-BRCT4 and the Polε subunit PolE2 bind to largely distinct neighbouring sites in Psf1. Our TopBP1-GINS model improves our understanding of the recently characterised metazoan pre-loading complex. It further predicts the coordination of three molecular origin firing processes, DNA polymerase epsilon arrival, TopBP1 ejection and GINS integration into Mcm2-7-Cdc45.

Introduction

Duplicating the genome accurately and exactly once each cell cycle lies at the heart of faithful genetic inheritance. The effective execution and regulation of DNA replication origin firing is pivotal to accurate genome duplication. Our understanding of how origin firing in eukaryotes generates replisomes from pre-replicative complexes (pre-RCs), their inactive precursors, has increased. However, how the two helicase activators GINS and Cdc45 are loaded onto pre-RCs remains less well understood.

Pre-RCs form during origin licensing in the G1 phase of the cell cycle when the activity level of cyclin-dependent kinases (CDKs) are low [1]. A set of essential licensing factors loads two copies of the Mcm2-7 helicase onto origin DNA such that a head-two-head double Mcm2-7 hexamer forms with tightly interacting N-terminal faces. Double-stranded DNA passes through the central channels of these helicase-inactive pre-RCs [2, 3, 4]. In the following S phase, high CDK activity induces origin firing, converting each pre-RC into two bi-directional replisomes; the Mcm2-7 double hexamer separates, helicase activity is switched on, the dsDNA running inside the hexamers is unwound, and what will become the single lagging strand DNA template is excluded from each hexamer (supplementary Fig. S1). The two active helicases to pass each other, engaging with the DNA fork with their respective N-terminal faces [5, 6].

Mcm2-7 helicase activation involves the loading of Cdc45 and GINS onto pre-RCs to form the CMG (Cdc45-Mcm2-7-GINS) helicase that shows robust in vitro helicase activity in contrast to pre-RCs [7, 8, 9, 10]. CMG assembly requires ADP-ATP exchange in the active nucleotide binding sites of the Mcm2-7 AAA ATP binding domains and occurs tightly coupled with partial Mcm2-7 double hexamer splitting and limited untwisting of the dsDNA inside the

central CMG channels [6, 11, 12]. The subsequent extensive dsDNA unwinding, CMG bypass and assembly of mature replisomes depends on the Mcm10 protein and on many additional replisome components [6, 10].

In budding yeast, Cdc45 and GINS integration requires Dbf4-dependent kinase (DDK), S-CDK, the Sld3-Sld7 protein complex (Treslin-MTBP in higher eukaryotes), Dpb11 (TopBP1), Sld2 (potential orthologue RecQL4) and DNA polymerase epsilon (DNA Polε) [10, 13, 14]. DDK binds pre-RCs and phosphorylates the Mcm2-7 helicase, allowing Sld3-Sld7$^{\text{Treslin-MTBP}}$ association [15, 16, 17]. Pre-RC-bound Sld3-Sld7$^{\text{Treslin-MTBP}}$ recruits Cdc45 involving a direct Sld3^{Treslin}-Cdc45 interaction [14, 18, 19]. Sld3-Sld7$^{\text{Treslin-MTBP}}$ is also involved in recruiting Dpb11$^{\text{TopBP1}}$. For this, S-CDK phosphorylates Sld3^{Treslin} on conserved CDK consensus sites, which can then bind to the N-terminal BRCT (breast cancer type 1 susceptibility) domains of Dpb11$^{\text{TopBP1}}$ [20, 21, 22] (Fig. 1a(i)). The interaction between Sld3^{Treslin} and Dpb11$^{\text{TopBP1}}$ serves to recruit the pre-loading complex (pre-LC) to pre-RCs, comprising Dpb11$^{\text{TopBP1}}$, GINS, Sld2$^{\text{RecQL4}}$ and DNA Polε [23]. Pre-LC recruitment is mediated by a CDK phosphorylation-mediated interaction between phospho-threonine 84 of Sld2$^{\text{RecQL4}}$ and the C-terminal BRCT-pair of Dpb11$^{\text{TopBP1}}$ (Fig. 1a(i)). Sld2$^{\text{RecQL4}}$, Dpb11$^{\text{TopBP1}}$ and Sld3-Sld7$^{\text{Treslin-MTBP}}$ then detach from the origin-bound CMG [13, 24], leaving GINS and Cdc45 behind to form the CMG helicase. DNA Polε associates with CMG in a dynamic fashion to form the CMGE complex (CMG-DNA Polε) [25]. The N-terminus of the Dpb2 subunit of DNA Polε and its vertebrate equivalent PolE2 bind to the Psf1 subunit of GINS [26, 27]. It has been suggested that this interaction represents the essential activity of DNA Polε in replication origin firing [25].

The precise molecular mechanism underpinning how TopBP1$^{\text{Dpb11}}$, Treslin/$^{\text{Sld3}}$ and MTBP$^{\text{Sld7}}$ deliver GINS and Cdc45 to the Mcm2-7 helicase remains unclear. TopBP1$^{\text{Dpb11}}$ is a multi-BRCT domain scaffold protein containing nine BRCT domains [28] (Fig. 1a(i)). The triple-BRCT module at the N-terminus of TopBP1$^{\text{Dpb11}}$ plus the BRCT4/5 pair share homology with budding yeast Dpb11 [29]. As detailed above, TopBP1 and Dpb11 facilitate the coupling of origin firing to the cell cycle using their respective N-terminal BRCT modules [21, 22, 30]. TopBP1$^{\text{Dpb11}}$-BRCT4/5 was, however, found to be non-essential to replication in *Xenopus* egg extracts [30]; perhaps surprisingly as the equivalent BRCT module of Dpb11$^{\text{TopBP1}}$ (BRCT3/4) is essential [23] (Fig. 1a(i)). The minimal fragment of TopBP1$^{\text{Dpb11}}$ that supports replication includes BRCT0/1/2, BRCT3 (not conserved in Dpb11) and a short segment C-terminal to BRCT3 termed the GINS interaction or 'GINI' region [30, 31]. Yeast-two hybrid experiments showed that the GINI regions of TopBP1 and Dpb11, which have little sequence identity, both bind to GINS [31] (Fig. 1a(i)). As both TopBP1 and Dpb11 are limiting factors for origin firing [32, 33, 34], it is likely that they are released and recycled to facilitate replication from multiple different origins [35]. Both association and disassociation of Dbp11$^{\text{TopBP1}}$ are therefore important processes.
Recent evidence showed that, in metazoa, TopBP1$^{\text{Dpb11}}$ and GINS are members of a pre-LC-like complex that also contains DNA polε and a new metazoa-specific origin firing factor, DONSON, which interacts with TopBP1$^{\text{Dpb11}}$ [36, 37, 38, 39]. Pre-LC integrity appears to be important for metazoan origin firing because the interactions of DONSON with TopBP1 and

118 GINS with Mcm3 are necessary for efficient origin firing. The TopBP1-GINS interaction was
119 not characterised in detail in these recent publications.
120
121 Here, we have used purified proteins to address how TopBP1 loads GINS onto pre-RCs to
122 activate the Mcm2-7 helicase during replication origin firing. Our structural, biochemical, and
123 functional studies uncover the binding mode of GINS to TopBP1 and reveal an important role
124 for the TopBP1-BRCT4 domain in replication, previously thought to be dispensable. Our data
125 provide a model and framework for future investigation of CMG formation through GINS and
126 Cdc45 loading by TopBP1 and the Treslin-MTBP complex. Moreover, our study provides
127 insight how TopBP1 acts at a molecular level. Such detailed understanding of TopBP1 is key
128 to unravelling how this important scaffold protein can integrate its many different cellular roles
129 in chromosome biology [28].
130
131
132 **Results**
133
134 **TopBP1 interacts with GINS *in vivo* and *in vitro***
135 As previous yeast two-hybrid experiments showed an interaction of the human and *Xenopus*
136 TopBP1-GINI region with GINS (Psf1 and Psf3) [31], we tested if a similar interaction could be
137 detected in human cells. Three proximity biotinylation experiments using cells expressing
138 APEX2-tagged TopBP1 resulted in a specific enrichment of Psf3 upon streptavidin pulldown
139 and mass spectrometry, amongst a range of other known TopBP1 interactors (supplementary
140 Fig. S2a). Psf2 was also detected in one experiment. Immunoprecipitation from lysates of cells
141 transfected with TopBP1-BRCT0-5 (aa, amino acids 1-766) showed a weak but specific signal
142 for the GINS subunit Sld5 (supplementary Fig. S2b,c). These experiments suggest that TopBP1
143 and GINS interact in human cells.
144 In addition, purified recombinant TopBP1-BRCT0-5 (TopBP1-0-5-WT) co-eluted with the
145 GINS complex from a size exclusion column at a higher apparent molecular mass, when
146 compared to either TopBP1 or the GINS complex alone (Fig. 1b; supplementary Fig. S3a).
147 These results demonstrate that a TopBP1 fragment spanning the BRCT repeats 0-5 is sufficient
148 to interact with GINS both *in vivo* and *in vitro*.
149
150 **Two binding motifs within TopBP1 contribute to GINS binding**
151 We then used deletion and mutation analysis to narrow down the GINS binding region within
152 the TopBP1-BRCT0-5 fragment (Fig. 1a(ii)). Removing the Treslin-binding BRCT0-2 module
153 (TopBP1-ΔBRCT0/1/2) or BRCT3 (TopBP1-ΔBRCT3) from TopBP1 did not affect binding
154 (supplementary Fig. S3b,c). In contrast, deleting BRCT4/5 downstream of the GINI region
155 (TopBP1-ΔBRCT4/5) strongly impaired GINS interaction (Fig. 1c). We confirmed that the
156 phospho-binding pocket of BRCT5 was not required for this interaction, using a triple point
157 mutant that compromises its phospho-binding ability (B5mut) [40] (Fig 1a(ii), supplementary
158 Fig. S3d,e)). Our observations strongly suggested that a second GINS-binding motif, in
159 addition to the GINI region, is present in the BRCT4/5 module. This was interesting, as no
160 replication role for TopBP1-BRCT4/5 had been defined previously.

161
162 **Cryo-EM structure of TopBP1-BRCT4/5 in complex with GINS**
163 To reveal how TopBP1 interacts with the GINS complex, peak fractions of TopBP1-
164 BRCTΔ0/1/2 in complex with GINS eluting from the size exclusion column (supplementary
165 Fig. S3b) were used for cryo-EM. Movies were collected on an FEI Titan Krios microscope
166 equipped with a Gatan K3 camera. 18,945 movies were processed using a combination of
167 CryoSPARC [41] and RELION [42] (supplementary Fig. S4) to produce a final 3-dimensional
168 reconstruction, derived from 208,115 particles at 4.6 Å based on Fourier shell correlation (FSC)
169 values. Density corresponding to the GINS tetramer could be readily identified in the resultant
170 map, allowing facile placement of an X-ray crystal structure by rigid-body docking
171 (PDB:2E9X) (Fig. 2a). As features of the individual GINS subunits were clearly identifiable,
172 this also allowed unambiguous orientation of the pseudo-symmetric complex. The crystal
173 structure appeared to account for all the density seen with the exception of a protrusion away
174 from the main body of the GINS complex. This remaining density was too large to represent
175 just the B domain of Psf1 (absent from the docked X-ray crystal structure), or the single BRCT3
176 of TopBP1, but was readily accounted for by docking of the X-ray crystal structure for
177 TopBP1-BRCT4/5 (PDB:3UEN). The two BRCT domains were arranged such that BRCT4
178 interacted directly with the Psf1 subunit of GINS.
179
180 The GINS interacting region within the BRCT4 repeat of TopBP1 faces towards the A domain
181 of Psf1 and the linker region connecting domains A and B (Fig. 2a,b), close to where the B
182 domain docks to the CMG helicase (B domain not resolved). Note that some ambiguity exists
183 as to the precise molecular details due to the moderate resolution. In BRCT4, the interaction
184 surface involves a region around beta strands β3 and β4. This region diverts from the canonical
185 BRCT fold in that it lacks an alpha helix (α2) [42] as if to create space for GINS binding
186 (supplementary Fig. S5a,b). The region shows high sequence conservation in BRCT4
187 equivalents across a wide range of metazoans (supplementary Fig. S5c). The GINS interaction
188 surface in BRCT4 consists of residues found at the edge of the central four-stranded β-sheet,
189 with additional interactions made by residues in the loops connecting the strands, including
190 amino acids in the variant region between strands β3 and β4. Together, TopBP1-BRCT4 binds
191 to the A domain of Psf1 and involves the linker region located towards the B domain. To our
192 knowledge, this represents a novel mode for a BRCT domain-mediated interaction.
193
194 TopBP1 residues Val590, Thr606 and Val610 appeared to be involved in the interface,
195 providing a series of direct hydrophobic interactions with the side chains of Trp92 and Ile97 in
196 Psf1 (Fig. 2b). We mutated the three TopBP1 residues to glutamate, arginine and glutamate,
197 respectively, and tested if the resulting protein (TopBP1-B4mut; Fig. 1a(ii)) co-purified with
198 GINS. Here, TopBP1-B4mut was strongly compromised in its ability to bind GINS (Fig. 2c)
199 but could still interact with phospho-53BP1 (supplementary Fig. S6a). We also altered the
200 opposing Psf1 interface by mutating Ile97 to an arginine (Psf1-I97R). Recombinant Psf1-I97R
201 bound TopBP1 weaker than the wild type protein (Fig. 2d), but could still form GINS tetramers
202 (supplementary Fig. S6b).
203

204 **TopBP1 requires the conserved core of the GINI region for GINS binding**
205 As the predicted interface between the TopBP1-GINI region and GINS [31] was not evident in
206 our cryo-EM map we used additional interaction experiments to validate a role for this motif
207 in GINS binding. The GINI region had been loosely defined as sitting between TopBP1-
208 BRCT3 and BRCT4 (Fig. 1a(i)). Multiple sequence alignment across this region revealed a
209 high degree of conservation between vertebrate species with the section from Glu484 to
210 tyrosine 494 consisting of almost completely identical amino acids (Fig. 3a, supplementary
211 Fig. S7). We mutated this core, and other regions of conservation, to generate the mutants
212 TopBP1-Gcc (GINI centre core), Gcore (GINI core) and RI-III (regions I-III) (Fig. 3a,
213 supplementary Fig. S7). Pull-down experiments revealed that TopBP1-Gcc and Gcore, but not
214 RI-III, were compromised in GINS interaction (Fig. 3b). Secondary structure prediction and
215 AlphaFold2 models of TopBP1 suggested the presence of a short helix within this core region
216 for some vertebrate species. By mutation of the central leucine-leucine motif to two
217 consecutive prolines to break the helix (TopBP1-Gpp; Fig. 3a) we could show that the
218 interaction with GINS was strongly compromised, with no effect on binding to 53BP1
219 (supplementary Figs. S6a, Fig 3c)). To test if this helix constituted a GINS-interaction surface,
220 we used fluorescence polarisation (FP). A fluorescently labelled GINI-core peptide (Ala478-
221 Gly497) bound the GINS tetramer with a dissociation constant of K_d of ~8 μM (Fig. 3d). A
222 peptide harbouring the PP mutation failed to bind (Fig. 3d). We therefore concluded that the
223 GINI region is a GINS interaction site in its own right, but with moderate binding affinity.
224
225 **The GINI-core helix binds Psf1 and 3**
226 We next sought to identify the site in GINS that interacts with the TopBP1-GINI region.
227 Structural prediction using AlphaFold2-Multimer suggested that the GINI-core helix interacted
228 with the distal part of the Psf1 A domain (Fig 4a, supplementary Fig. S8). Moreover, 'blind'
229 molecular docking simulations with the GINI core region (487-DEDLLSQY-494) resulted in
230 the top-10 solutions clustering in the region of the AlphaFold-predicted GINI binding site
231 (supplementary Fig. S9).
232
233 A BS^3-crosslinking mass spectrometry experiment with purified recombinant TopBP1-GINS
234 also confirmed the predicted proximity of the TopBP1-GINI core helix region (residues 487-
235 494) and the Psf1-A domain. Several GINI-core-proximal residues crosslinked with Psf1-
236 Lys63 and Thr61 (supplementary Fig. S10a, supplementary table 1); both crosslinked Psf1
237 residues are situated at the distal end of the Psf1 A domain (supplementary Fig. S10b,c). The
238 GINI-core-proximal residues also crosslinked with lysines 74 and 80 of Psf3; each Psf3 residue
239 also being in close proximity to the predicted site of interaction. Given that the GINI-core helix
240 itself contains no lysine residues, our data are consistent with the hypothesis that this helix
241 binds to both the distal region of the Psf1 A domain and the adjacent region of Psf3
242 (supplementary Fig. S10 provides a detailed description).
243
244 With all this information in hand, we could improve the resolution of our cryo-EM data, using
245 an alternative GINS-expression construct, which omits the Psf1-B domain, and served to
246 improve detail around the predicted interaction region (supplementary Fig. S11). The resultant
247 map allowed a short helical element to be incorporated into our model, consistent with the

248 AlphaFold2-Multimer predictions (Fig. 4b). The hydrophobic side of the amphipathic GINI-
249 core helix can be seen to pack across two helices of the Psf1-A domain, making interactions
250 with the side chains of Leu490 and Leu491 of the GINI region and Val47, Lys51, Ile59, Ile62,
251 Lys63 and His66 of Psf1. Additionally, the side chain of Tyr494 in the GINI region is inserted
252 into a small pocket on the surface of Psf1 formed by Tyr40, Asn43 and Leu69 with the hydroxyl
253 group picking up a hydrogen bond with the side chain of His66.
254
255 For validation, we mutated Asn43 and Lys51, to Ala and Glu, respectively. Asn43 forms part
256 of the pocket accepting Tyr494 from the GINI region, whilst Lys51 is positioned such that it
257 could form a salt bridge with either Asp487 or Glu495 and part of the hydrophobic grove that
258 accommodates the leucines of the GINI-core helix. Psf1-N43A/K51E readily formed the GINS
259 tetramer (supplementary Fig. S6b) but was severely compromised in its ability to interact with
260 TopBP1-BRCT0-5-WT (Fig. 4c), again consistent with binding of the GINI region to the distal
261 end of the Psf1-A domain and the adjacent regions in Psf3.
262
263 **Simultaneous inactivation of the GINI core region and BRCT4 is required to suppress**
264 **replication origin firing**
265 Our pulldown interaction studies with GINS and TopBP1-BRCT0-5 carried out at 150 mM
266 sodium chloride suggested that the GINS interacting regions GINI and BRCT4 of TopBP1 are
267 individually required for GINS interaction (Figs. 1c,3c). However, pulldowns in 100 mM
268 sodium acetate revealed specific interactions of the individual interaction regions, albeit at
269 reduced levels compared to TopBP1-WT (Fig 5a, supplementary Fig. S12a). Here, the GINI
270 region bound to GINS more efficiently than BRCT4. Consistently, estimation of binding free
271 energies suggested that the affinities are lower when the surfaces interact individually rather
272 than simultaneously (Fig. 5b). Together, this suggests a model in which both interactions have
273 relatively moderate binding affinities, but cooperate to form a composite interaction surface
274 with high avidity.
275
276 We next asked how the GINI and BRCT4 regions contribute to genome replication, by testing
277 if mutational inactivation of the TopBP1-GINI and BRCT4 regions (Fig. 5c) could suppress
278 replication in *Xenopus* egg extracts. Immunodepleting TopBP1 with two independent
279 antibodies (anti-TopBP1-#1 and #2) effectively removed the endogenous TopBP1 (Fig. 5d(i)),
280 but neither GINS, MTBP, DNA Polε nor Cdc45 (Fig. 5d(ii), from the extracts. TopBP1
281 depletion strongly reduced incorporation of radioactive α-^{32}P-dCTP when compared to a
282 'mock' IgG depletion control (Fig. 5e). Adding recombinant TopBP1-BRCT0-5-WT
283 effectively rescued replication in depleted extracts (Fig. 5e), whereas addition of either
284 TopBP1-BRCT0-5-Gcc or TopBP1-BRCT0-5-Gpp (BRCT4 intact) showed moderate
285 reductions in replication when compared with WT (Fig. 5f, supplementary Fig. S13a),
286 consistent with the observed reduced affinity of BRCT4 for GINS (Fig. 5a). TopBP1-
287 ΔBRCT4/5 and TopBP1-B4mut (GINI domain intact) were not detectably compromised in
288 their abilities to support replication (Fig. 5f; supplementary Fig. S13b), as observed before [30,
289 31], consistent with the GINI region binding GINS stronger than BRCT4. Combination of
290 BRCT4/5 deletion or mutation (B4mut) with either TopBP1-BRCT0-5-Gcc or -Gpp decreased

291 replication to nearly background levels (Fig. 5f, supplementary Fig. S13), consistent with these
292 double mutants eliminating GINS binding (Fig. 5a/b). These results indicate that both TopBP1
293 binding regions, GINI and BRCT4, are individually capable of supporting replication, whilst
294 simultaneous inactivation of the GINS binding regions strongly suppresses replication.
295
296 We next tested if the TopBP1-GINS interaction is required for replication origin firing. We
297 isolated chromatin from *Xenopus* egg extracts upon immuno-depletion and add-back of
298 TopBP1-BRCT0-5-WT or mutants, 75 minutes after starting replication (a time point when
299 genome replication has progressed significantly). To increase signals, we added aphidicolin,
300 which prevents termination, allowing replisomes to accumulate on chromatin. Mass
301 spectrometry using the CHROMASS protocol [43] and immunoblotting showed geminin-
302 sensitive chromatin binding of Mcm2-7 subunits when buffer was added, indicating that
303 licensing is independent of TopBP1 (Fig. 6, supplementary Fig. S14, supplementary table 2).
304 Several replisome markers, including GINS and Cdc45, were detected on chromatin in extracts
305 containing TopBP1-WT, but were significantly reduced when buffer or the TopBP1-Gcc-
306 ΔBRCT4/5 mutant were added. Thus, the GINS binding sites in TopBP1 are required for origin
307 firing (replisome formation), more precisely for a step between pre-RC formation and CMG
308 formation. Chromatin samples upon complementation with the single mutants TopBP1-Gcc
309 and TopBP1-ΔBRCT4/5 showed stronger and milder replisome formation defects, respectively
310 (Fig. 6d, supplementary Fig S12b), consistent with the GINI domain mediating stronger GINS
311 interaction than BRCT4. The TopBP1-Gcc-ΔBRCT4/5 double mutant did not increase
312 replisome markers over geminin control samples, whereas TopBP1-Gcc increased the levels
313 of individual replisome markers weakly but detectably (PolE2 in Fig 6d and Cdc45 in
314 supplementary Fig. S12b). Together, we conclude that both GINS binding sites in TopBP1 act
315 in concert to assemble the CMG helicase. We noticed a surprisingly strong origin firing defect
316 with the TopBP1-Gcc mutant, given that it supports replication to a significant level. It is
317 feasible that compensatory fork acceleration partially compensates for decreased replisome
318 numbers in the Gcc mutant. We cannot formally rule out that the BRCT4-GINS interaction has
319 a role downstream of origin firing that aggravates the DNA synthesis defects of GINI site
320 mutants.
321
322 **Mutually exclusive binding of TopBP1 and DNA Polε to GINS in the context of CMG**
323 We next explored the relationship between the interactions of TopBP1 and DNA Polε with
324 GINS. These proteins are part of the recently characterised metazoan pre-LC [36, 37, 38, 39]. We
325 find evidence that, in pre-LC, GINS may simultaneously bind DNA Polε and TopBP1. The N-
326 terminal region of PolE2 (PolE2-N; aa 1-75) binds GINS mainly at the Psf1-B domain, with
327 minor interactions with residues in the A-domain that partly overlap with the TopBP1-BRCT4
328 interaction surface (Fig. 7a-c). Pulldowns with GINS lacking the Psf1-B domain indicated that
329 the B domain is dispensable for TopBP1 interaction, suggesting that BRCT4 and PolE2-N
330 binding surfaces on GINS are at least partly distinct (supplementary Fig S15a). Consistently,
331 we found no competition between TopBP1 and PolE2-N in GINS pulldown experiments
332 (supplementary Fig S15b). Next, we analysed the CMGE helicase. The accessibility of both
333 TopBP1 binding sites in the CMG helicase suggests that TopBP1 could bind GINS in the CMG

334 context (Fig. 7a,b) [27]. However, the binding of DNA Polε and TopBP1 seem mutually
335 exclusive. Superposition of CMGE and CMG-TopBP1 revealed potential major steric clashes
336 between TopBP1 and PolE2 around the BRCT4 interaction region (Fig. 7a-c). Thus, despite
337 the lack of direct competition for the binding surface, we speculate that TopBP1-BRCT4 must
338 disengage before DNA Polε associates to form CMGE. Our finding that both TopBP1-GINS
339 binding surfaces must cooperate for a strong interaction suggests that BRCT4 disengagement
340 will significantly weaken the TopBP1-GINS interaction, aiding full dissociation of TopBP1.
341
342 The transition of GINS from TopBP1-bound to a stable CMG requires reconfiguration of the
343 Psf1-B domain [44]. In CMG, the Psf1-B domain adopts a discrete conformation tightly packing
344 against Cdc45 (Fig. 7a) [27]. In contrast, the B domain appears flexible in the GINS tetramer and
345 in the TopBP1-GINS complex, because our cryo-EM data did not detect the B domain at the
346 same map contour level as the rest of GINS (supplementary Fig. S15c,d). A previous
347 crystallization study of the GINS tetramer also suggested Psf1-B domain flexibility [45]. Thus,
348 integration of GINS in the CMG appears to order the B domain. In this conformation, the B
349 domain binds to the N-terminus of PolE2 once DNA Polε associates to form CMGE [27].
350
351 Together, we envision that the Psf1-B domain reconfigures into a well-ordered state upon CMG
352 assembly. TopBP1-BRCT4 must then dissociate to exchange with DNA Polε for CMGE
353 formation, which likely helps TopBP1 dissociate. Once CMG has formed, DNA Polε seems to
354 dynamically associate with CMG [25]. These observations suggest that the three processes 1)
355 handover of GINS from TopBP1 to pre-RCs, 2) DNA Polε association and 3) TopBP1
356 dissociation may be mechanistically intertwined.
357
358
359 **Discussion**
360
361 Our data provide an understanding of the interaction between TopBP1^{Dpb11} and GINS at the
362 molecular level, and how this supports replication origin firing. Recent insight into origin firing
363 has largely come from studies focussed on understanding how the yeast Mcm2-7 helicase
364 operates as a molecular machine to build replication forks [6, 10, 11, 12, 14, 16, 17, 19, 46, 47, 48, 49]. The
365 aspect of how GINS and Cdc45 are loaded to activate the helicase through formation of the
366 CMG complex has only recently been addressed in more detail by describing the metazoan
367 pre-LC [36, 37, 38, 39]. Our studies here reveal an important aspect of pre-LC, namely the essential
368 role of the TopBP1^{Dpb11}-GINS interaction (supplementary Fig. S16).
369 Formation of the CMG complex serves as a key regulatory step of origin firing. In metazoa
370 and yeast, CMG formation involves the factors Treslin/Sld3, MTBP/Sld7, RecQL4/Sld2,
371 TopBP1/Dpb11 and the Mcm2-7 helicase itself. Apart from coupling origin firing to the S
372 phase via S-CDK and DDK, these signal integrators are targeted by the DNA damage
373 checkpoint and other regulatory pathways to mediate DNA damage-dependent origin firing
374 control, execution of the temporal replication program and fine-tuning of origin firing [50, 51, 52,
375 53, 54, 55, 56, 57, 58, 59, 60, 61, 62, 63, 64]. Such regulation helps avoid replication stress that is key to
376 structural and numerical chromosomal instability in cancer cells [65].

377
378 TopBP1^{Dpb11} is a scaffold protein. To mediate S phase coupling of origin firing, the N-terminal
379 triple BRCT0-2 module of TopBP1^{Dpb11} binds Treslin^{Sld3}, in a strictly phospho-dependant
380 manner, via two CDK sites that are also conserved in budding yeast Sld3^{Treslin} [21, 22]. Despite
381 this level of conservation, some aspects of origin firing in vertebrates are likely to have changed
382 mechanistically when compared to the yeast paradigm: 1) DDK strengthens the interaction
383 between TopBP1^{Dpb11} and the Treslin-MTBP$^{Sld3\text{-}Sld7}$ complex, albeit via an unclarified
384 mechanism [66], whereas a similar role for DDK in yeast has not been reported. 2) an N-terminal
385 fragment that excludes the BRCT4/5 module of TopBP1^{Dpb11} effectively supports replication
386 in *Xenopus* egg extracts [30, 31], whereas the equivalent BRCT3/4 module of Dpb11^{TopBP1} is
387 essential, thorough CDK-mediated binding to phospho-Sld2^{RecQL4} [23]. The metazoan-specific
388 DONSON protein may replace some roles of Sld2 [36, 37, 38, 39]. These mechanistic differences
389 exemplify evolutionary flexibility in S-phase coupling, supported by findings in the *C. elegans*
390 and fission yeast model organisms where the contributions of Treslin^{Sld3} and RecQL4^{Sld2}
391 equivalents have changed during evolution [67, 68]. Such flexibility may be supported by the
392 partially redundant roles of S phase kinases (S-CDK and DDK) and their substrates (Treslin^{Sld3},
393 RecQL4^{Sld2}, Mcm2-7).
394 TopBP1^{Dpb11} supports CMG formation via an interaction with the GINS complex. In budding
395 yeast, Dpb11^{TopBP1} and GINS are recruited to pre-RCs as part of a 'pre-loading complex' (pre-
396 LC) comprising Dpb11^{TopBP1}, GINS, DNA Polε and Sld2^{RecQL4} [69]. Dpb11^{TopBP1} appears to
397 'dock' the pre-LC onto Sld3^{Treslin}-Sld7^{MTBP}-Cdc45 via the CDK-mediated Dpb11^{TopBP1}-
398 Sld3^{Treslin} interaction; DDK is required for initial binding of Sld3^{Treslin}-Sld7^{MTBP}-Cdc45 onto
399 pre-RCs [14, 19]. In metazoans, RecQL4^{Sld2} is not part of the stable protein complex defined as
400 pre-LC, which instead contains DONSON. DONSON is a scaffold protein with a series of
401 interaction sites for TopBP1^{Dpb11}, GINS, DNA Polε and Mcm3 (supplementary Fig. S16a) [36,
402 37, 38, 39]. Our described TopBP1^{Dpb11}-GINS interaction probably plays a role in the context of
403 pre-LCs.
404
405 The GINI region of TopBP1^{Dpb11} that had been broadly defined as the region between BRCT3
406 and BRCT4, bound to Psf1 and 3 in Y2H experiments [31]. We show here that a short alpha-helix
407 found at the core of the conserved GINI region (GINI-core helix) forms an essential part of the
408 binding surface that is necessary and sufficient for detectable interaction with GINS. This helix
409 cooperates with a second binding site situated in BRCT4 to form a composite high-affinity
410 GINS-interaction surface; involving a hereinto unknown mode of BRCT-interaction that relies
411 on a specific type of BRCT fold found in TopBP1-BRCT4, which lacks helix 2. Notably, our
412 *in vitro* experiments show that each individual GINS interaction site is capable of binding
413 GINS, albeit with reduced efficiency compared to the complete composite interaction surface.
414 This was consistent with the two GINS binding sites being able to support significant levels of
415 replication in *Xenopus* egg extracts, which is in line with an earlier study focussing on the GINI
416 region [31]. These results indicate that even a low affinity TopBP1^{Dpb11}-GINS interaction is
417 sufficient to allow origin firing. *In vivo*, contacts between other pre-LC components may
418 compensate for a weak TopBP1^{Dpb11}-GINS interaction. A high degree of inter-dependence
419 between association of the components was also observed for the yeast pre-LC complex [69].

420 Simultaneous mutation of both GINS binding domains in TopBP1 suppressed origin firing.
421 This suggests that neither interaction site has a unique molecular role beyond GINS binding.
422 The simplest scenario is that their common essential molecular role is to bind GINS
423 chaperoning it onto pre-RCs.
424 An alternative interpretation of our TopBP1 mutant analysis seems feasible: TopBP1-Δ4/5 and
425 B4mut only resulted in weak, if any, DNA synthesis and origin firing defects. This is consistent
426 with the possibility that the BRCT4-GINS interaction plays an unidentified role in replication,
427 for example in elongation, which could contribute to aggravating observed defects of GINI site
428 mutants.
429
430 Consistent with published Y2H experiments [31], our structural data indicate that the GINI core
431 helix region interacts with both Psf1 and Psf3, at a position close to the distal end of the Psf1
432 A domain, whereas BRCT4 interacts with both the base of the Psf1-A domain and the linker
433 that connects it to the B domain. Notably, the two receiving interfaces in GINS are fully
434 accessible both in the free GINS tetramer and in the CMG context, consistent with a model
435 where TopBP1^{Dpb11} recruits GINS using both motifs (supplementary Fig. S16b). TopBP1^{Dpb11}
436 may simultaneously bind phosphorylated Treslin^{Sld3}-MTBP^{Sld7} via its N-terminal BRCT0-2
437 module [21, 22, 70], with Treslin^{Sld3} bringing Cdc45 along through its Sld3-Treslin homology
438 domain [18, 71]. One open question in the field had been the biological role of the BRCT3 domain
439 in TopBP1, which has no equivalent in Dpb11. We now know that an essential role of BRCT3
440 is the binding to DONSON [36 37].
441
442 After delivery of GINS and Cdc45, the subsequent release of TopBP1^{Dpb11} and Treslin^{Sld3}-
443 MTBP^{Sld7} is also likely to be important, as presumably they must be 'recycled' to allow the use
444 of late firing origins [34]. The action of phosphatases could help disassemble the Treslin^{Sld3}-
445 MTBP^{Sld7}-TopBP1^{Dpb11} complex as part of factor recycling, which may assist release from the
446 helicase [35, 72]. Moreover, the low affinities of the two individual GINS-interacting sites in
447 TopBP1^{Dpb11} offer the idea that release of one site would significantly destabilise the complex
448 to trigger TopBP1^{Dpb11} dissociation. Competition of DNA Polε with TopBP1 binding may also
449 be involved in TopBP1 dissociation, because simultaneous binding of the two proteins is
450 sterically impossible without a significant conformational change. Whether TopBP1^{Dpb11}
451 dissociation is a prerequisite for DNA Polε association, or whether the polymerase acts to
452 displace TopBP1^{Dpb11} remains unclear; the important but mechanistically unclear role of DNA
453 Polε in CMG formation therefore remains open [25, 26]. The reconfiguration of the Psf1-B domain
454 during CMG formation suggests another potential mechanism for TopBP1 release. The B
455 domain seems flexible in the TopBP1-GINS complex and establishes an extensive set of
456 interactions with Cdc45 when it reconfigures to form CMG, which might favour Polε binding
457 over TopBP1^{Dpb11}-BRCT4.
458
459 Recent insights have suggested that formation of the CMG complex is tightly associated with
460 (i) splitting of Mcm2-7 double hexamers into single hexamers; (ii) the exchange of ADP for
461 ATP in the Mcm2-7 nucleotide-binding sites; and (iii) limited untwisting of dsDNA inside the
462 central channels [6, 11, 12]. How TopBP1, Treslin and MTBP relates to these steps will be key to

463 understanding whether their mechanistic roles go beyond just a simple chaperoning function,
464 guiding Cdc45 and GINS to pre-RCs. For example, the reported homo-dimerization of TopBP1
465 and MTBP might play a role in the cooperative conversion of Mcm2-7 hexamers into
466 replisomes, thus guaranteeing bi-directional replication [66, 73].
467
468 Taken together, our data provide insight into, and a testable hypothesis for, the series of
469 molecular events leading to CMG formation, and its regulation; potentially leading to future
470 therapeutic routes for the treatment of cancer, due the high reliance of tumours on high levels
471 of replication initiation [74]. Targeted interference with origin firing could be one potential
472 avenue, consistent with the testing of DDK inhibitors as candidates in clinical trials [75].
473

474 # Methods
475
476 **Antibodies**
477

name	Antigen/source
Anti-DB4	human TopBP1-aa1-360, rabbit, self-made
Anti Sld5	human Sld5-aa1-100, rabbit monoclonal ERP9318, Abcam ab139683
Anti-Flag	Flag peptide, mouse, clone M2, Sigma F1804
Anti-53BP1	Human 53BP1 aa 350-400, rabbit, Invitrogen PA1-16565
Anti-Myc	Myc tag, mouse, clone 9E10
Anti-TopBP1 #1	Xenopus TopBP1-aa1-365, rabbit, self-made
Anti-TopBP1 #2	Xenopus TopBP1-aa999-1299, rabbit, self-made
Anti-XCdc45	Xenopus Cdc45, rabbit, self-made
Anti-XSld5	Xenopus Sld5, rabbit, self-made
Anti-XPolE2	Xenopus PolE2, rabbit, self-made
Anti-Mcm6	Mcm6-aa775-821, rabbit, BETHYL A300-194A
Anti-Mcm4	Mcm4-aa750-850, rabbit, Abcam ab4459
Anti-PCNA	Human PCNA, mouse, clone PC10
Anti-MBP	MBP tag, mouse, New England BioLabs E8032S

478
479
480 **DNA plasmids**
481

plasmid name	vector backbone	recombinant protein
BT702	pLib	TopBP1-1-766 L489P/L490P-Strep
BT707	pLib	TopBP1-1-766-Strep
BT708	pLib	TopBP1-1-766 RegionI-Strep
BT709	pLib	TopBP1-1-766 RegionII-Strep
BT710	pLib	TopBP1-1-766 RegionIII-Strep
BT711	pLib	TopBP1-1-766 Gcore-Strep
BT712	pLib	TopBP1-1-766 Gcc-Strep
BT735	pLib	TopBP1-1-766 S654V/K661R/K704E-Strep
BT759	pLib	TopBP1-1-549-Strep
BT760	pLib	TopBP1-1-549 Gcc-Strep
BT761	pLib	TopBP1-1-549-L489P/L490P-Strep
BT770	pLib	TopBP1-1-766 B4mut-Strep
BT772	pLib	TopBP1-1-766Gcc/B4mut-Strep
BT805	pLib	6xHis-3xFlag-Sld5
BT806	pLib	Psf1
BT807	pLib	Psf2
BT808	pLib	Psf3
BT781	pLib	Psf1 N43A/K51E
MD106	pBIG1a	Psf1 Psf2 Psf3 6xHis-3xFlag-Sld5
MD101	pLib	Psf1(1-151)
MD107	pBIG1a	Psf1(1-151) Psf2 Psf3 6xHis-3xFlag-Sld5

MD146	pET17b	HIS-TopBP1-1-766-Strep
MD147	pET17b	HIS-TopBP1-331-766-Strep
BT764	pcDNA5	APEX2-TopBP1
MP784	pcDNA5	TopBP1-APEX2
BT818	pMal	MBP-PolE2-N-1-75 (PolE2-N)

482
483
484 **Protein purification**
485
486 **Purification of recombinant TopBP1**
487 Purification of TopBP1-331-766 (BRCT3-5) for structural studies was done using bacterial
488 expression. BL21(DE3) cells carrying a pET17 plasmid encoding HIS-(3C)-TopBP1-331-766-
489 Strep was were grown in TurboBroth at 37 °C to an OD600 of 2.0 and induced by with 0.5
490 mM IPTG prior to overnight incubation at 16 °C. Lysis by sonication was done in lysis buffer
491 (25 mM HEPES pH 7.5, 200 mM NaCl, 0.5 mM TCEP, 10 U DNASE Turbo and complete,
492 EDTA-free Protease Inhibitor Cocktail (Merck). The resulting lysate was clarified by
493 centrifugation at 40,000 x g for 60 min at 4°C. The supernatant was applied to a 5 ml HiTrap
494 TALON crude column (GE Healthcare, Little Chalfont, UK), washed with lysis buffer,
495 followed by a wash with lysis buffer containing 10 mM imidazole. Elution followed by
496 increasing imidazole to 250 mM. The eluted protein was separated on a 5 ml HiTrap STREP
497 column (GE Healthcare, Little Chalfont, UK), and eluted with 2 mM desthiobiotin. The eluate
498 was concentrated before separation on a Superdex200increase 10 300 column (GE Healthcare,
499 Little Chalfont, UK) equilibrated in 10 mM HEPES pH 7.5, 150 mM NaCl, 0.5 mM TCEP.
500 Recombinant TopBP1-1-766-Strep-WT (BRCT0-5) and mutants for interaction studies and
501 experiments in *Xenopus* egg extract were purified using SF9 insect cells. The cells were grown
502 in suspension in insect cell media (Pan biotech, P04-850 500) at 27°C. Baculoviruses were
503 generated using pLIB-based constructs (Addgene, 80610). 500 ml Sf9 cells ($1x10^6$/ml) were
504 infected with a 1:100 dilution of recombinant baculovirus carrying TopBP1-1-766-Strep-WT
505 or mutants, and were incubated at 27°C for 72 h. Cell pellets were lysed by douncing in 30 ml
506 of lysis buffer (20 mM HEPES pH 8.0, 150 mM NaCl, 0.1% (v/v) Tween-20, 0.5 mM TCEP,
507 protease inhibitor cocktail (Roche Complete protease inhibitor cocktail, 05056489001)). The
508 lysate was centrifuged at 44,800 g for 45 min and the supernatant was loaded onto the
509 StrepTrapHP-1ml column (Cytiva, 28907546). Elution was done using 2.5 mM desthiobiotin
510 in elution buffer (20 mM HEPES pH 8.0, 150 mM NaCl, 0.01% Tween-20 (v/v), 0.5 mM
511 TCEP, 2% (v/v) glycerol, 2.5 mM desthiobiotin).
512
513 **Purification of GINS**
514 **GINS for structural and fluorescence polarisation studies was purified in SF9 insect cells**.
515 Psf2, Psf3 and HIS-(3C)-Sld5 were expressed together with Psf1 or Psf1(1-151; B domain
516 deleted)) from a single baculovirus, respectively, produced using pBig1a. Cell pellets were re-
517 suspended in lysis buffer containing 25 mM HEPES pH 7.5, 200 mM NaCl, 0.5 mM TCEP,
518 10 U DNASE Turbo and complete, EDTA-free Protease Inhibitor Cocktail (Merck), then
519 disrupted by sonication. The resulting lysate was clarified by centrifugation at 40,000 x g for
520 60 min at 4°C. The supernatant was separated on a 5mL HiTrap TALON crude column (GE

521 Healthcare, Little Chalfont, UK), using washing in lysis buffer supplemented with 10 mM
522 imidazole. Elution was done using a gradient up to 250 mM imidazole. Peak fractions were
523 pooled and concentrated . For subsequent size exclusion chromatography (analytical and for
524 EM) a Superdex200increase 10 300 column (GE Healthcare, Little Chalfont, UK) equilibrated
525 in 10 mM HEPES pH 7.5, 150 mM NaCl, 0.5 mM TCEP was used while for FP experiments
526 a Superdex200 16 600 column (GE Healthcare, Little Chalfont, UK) equilibrated in 25 mM
527 HEPES pH 7.5, 150 mM NaCl, 1 mM EDTA, 0.25 mM TCEP, 0.02 % (v/v) Tween 20 was
528 used.
529 GINS for pulldown experiments was purified using 6xHis-3xFlag-Sld5. Sf9 insect cells in
530 suspension cultures were co-infected with 1:50 dilution of each four recombinant baculoviruses
531 for expressing 6xHis-3xFlag-Sld5, Psf1, Psf2 and Psf3, respectively. The viruses were made
532 using pLib-based plasmids. 72 h post infection, pellets from one litre cells were lysed by
533 douncing in 60 ml of lysis buffer (20 mM HEPES pH 8.0, 300 mM NaCl, 0.1% (v/v) Tween-
534 20, 25 mM imidazole, 0.5 mM TCEP, protease inhibitor cocktail (Roche Complete protease
535 inhibitor cocktail, 05056489001)). The lysate was centrifuged at 44,800 g for 45 min and the
536 supernatant was incubated with 2.5 ml Ni-NTA agarose beads (Qiagen,30210) for 1 h at 4°C.
537 The bound protein was eluted with six bead volumes elution buffer (20 mM HEPES pH 8.0,
538 300 mM NaCl, 0.01% (v/v) Tween-20, 250 mM imidazole, 0.5 mM TCEP, 2% (v/v) glycerol).
539 The eluate was dialysed into 20 mM HEPES pH 8.0, 150 mM NaCl, 0.01% (v/v) Tween-20,
540 0.5 mM TCEP, 2% (v/v) glycerol, and then applied onto an HiTrap HP Q column (Cytiva,
541 17115301). To elute the bound protein, a linear gradient of NaCl (from 150 mM to 1 M) in
542 elution buffer (20 mM HEPES pH8.0, 0.01% (v/v) Tween-20, 0.5mM TCEP, 2% (v/v)
543 glycerol) was applied. Peak fractions were pooled and separated by size exclusion
544 chromatography (equilibration buffer: 20 mM HEPES pH8.0, 300mM NaCl, 0.01% (v/v)
545 Tween-20, 0.5mM TCEP, 2% (v/v) glycerol).
546
547 **Purification of PolE2-N and geminin from *E.coli***
548 PolE2-N-1-75 (amino acids 1-75) with N-terminal MBP-TEV2 tag in pMal, and GST tagged
549 *Xenopus* geminin (Xgeminin) in pGEX were expressed in Rosetta *E. coli* culture. Expressions
550 were induced with 1 mM IPTG at OD600 = 0.6 at 20 °C (PolE2-N) or 25 °C (Xgeminin)
551 overnight. Cells were harvested by centrifugation at 6000 rpm (JLA-8.1, Avanti JXN-26
552 Beckman Culture) for 20 min. For PolE2-N, cell pellets were resuspended in lysis buffer (20
553 mM Hepes pH 8.0, 150 mM NaCl, 0.5 mM TCEP, 2 % (v/v) glycerol and protease inhibitor
554 cocktail (Roche Complete protease inhibitor cocktail, 05056489001)) and lysed by sonication.
555 Cell suspension was centrifuged at 20000 rpm (SS-34, Sorvall RC 6 PLUS) for 30 min at 4 °C.
556 Supernatant was incubated with amylose resin (New England Biolabs, E8021S) for 1 h before
557 elution with lysis buffer + 10 mM maltose. The peak fraction was dialysed into TopBP1 buffer
558 (20 mM HEPES pH 8.0, 150 mM NaCl, 0.5 mM TCEP, 0.01 % (v/v) Tween20 and 2 % (v/v)
559 glycerol). For Xgeminin, lysis by sonication was carried out in 5 mg/ ml lysozyme, 20 mM
560 Hepes pH 7.7, 200 mM NaCl, 5 mM β-mercaptoethanol, 5 % glycerin. After centrifugation at
561 20,000 rpm (SS-34, Sorvall RC 6 PLUS) for 20 min at 4 °C, the supernatant was incubated
562 with glutathione-sepharose (0.5 ml per liter culture; GE Healthcare 17513201) for 3 h before
563 elution with lysis buffer + 50 mM glutathione (Applichem A2084,0025). Peak fractions were
564 pooled and dialyzed into XBE2 buffer (100 mM KCl, 2 mM MgCl2, 0.1 mM CaCl2, 1.71 %

565 w:v sucrose, 5 mM K-EGTA, 10 mM HEPES-KOH, pH 7.7) and concentrated to 360 µM
566 Xgeminin. Aliquots were shock frozen and stored at - 80 °C.
567
568 **Size exclusion chromatography for isolating the TopBP1-GINS complex**
569 Recombinant TopBP1 and GINS proteins were mixed in an equimolar ratio to give a final
570 concentration of 20 µM of each component and incubated on ice for at least 30 minutes prior
571 to application to a Superdex200increase 10 300 column (GE Healthcare, Little Chalfont, UK)
572 equilibrated in 10 mM HEPES pH 7.5, 150 mM NaCl, 0.5 mM TCEP.
573
574 **Fluorescence polarisation experiments**
575 Fluorescein-labelled peptides (WT: 'Flu'-GYGAPSEKHEQADEDLLSQYENG or LLPP:
576 'Flu'-GYGAPSEKHEQADEDPPSQYENG) (Peptide Protein Research Ltd, Bishops
577 Waltham, UK) at a concentration of 100 nM, were incubated at room temperature with
578 increasing concentrations of GINS in 25 mM HEPES pH 7.5, 150 mM NaCl, 1 mM EDTA,
579 0.25 mM TCEP, 0.02 % (v/v) Tween 20 in a black 96-well polypropylene plate (VWR,
580 Lutterworth, UK). Fluorescence polarisation was measured in a POLARstar Omega multimode
581 microplate reader (BMG Labtech GmbH, Offenburg, Germany). Binding curves represent the
582 mean of three independent experiments, with error bars of 1 standard deviation.
583
584 **Immunoprecipitations from transiently transfected 293T cells**
585 Transient transfections of 6xMyc-Tev2-TopBP1 into 293T cells (ATCC CRL-11268) were
586 carried out using PEI (polyethyleneimine) according to a protocol kindly shared by David
587 Cortez' lab. 4 µg plasmid DNA in 100 µl DMEM (Thermofisher, 41965039) without
588 penicillin-streptomycin were combined with 2.4 µl Polyethylenimin (Sigma, 408727; 10
589 mg/ml) and incubated for 20 minutes before addition to 4 x 10^6 cells on a 10 cm dish.
590 Transfected cells were used 72 h post transfection. 72 h post transfection, 293T cells were lysed
591 by douncing in ten times cell pellet volume of lysis buffer (20 mM HEPES pH8.0, 150mM
592 NaCl, 0.1 % (v/v) Tween-20, 0.5mM TCEP, 2% (v/v) glycerol, protease inhibitor cocktail
593 (Roche, Complete protease inhibitor cocktail, 05056489001)), and centrifuged at 20,000 g for
594 15 min at 4 °C. The soluble supernatant was added to magnetic anti-Myc beads (5 µl slurry per
595 sample; Thermofischer, 88842) and incubated for two hours at 4 °C rotating. Cells equivalent
596 to 50 % of a 15 cm dish were used per sample. Beads were washed three times in lysis buffer
597 with 5 min incubation each, and finally boiled in 50 µl Laemmli loading buffer (6.5 % glycerol,
598 715 mM β-mercaptoethanol, 3% SDS, 62.5 mM Tris-HCl pH 7.9, 0.005 % bromphenol blue).
599
600 **Pulldown experiments of recombinant PolE2-N or TopBP1 using immobilised GINS**
601 Magnetic anti-Flag beads (1 µl slurry for western blot/silver staining-scale experiments, 4 µl
602 for Coomassie-scale experiments) were coupled with 600 ng (western/silver-scale) or 2400 ng
603 (coomassie-scale) GINS via 3xFlag-Sld5. 100 nM final concentration of TopBP1-BRCT0-5-
604 Strep (WT or mutants) in 20 µl (western/silver-scale) or 80 µl (coomassie-scale) of interaction
605 buffer (20 mM HEPES pH8.0, 150mM NaCl (or 100 mM NaCH3COO when indicated), 0.01%
606 (v/v) Tween-20, 0.5mM TCEP, 2% (v/v) glycerol) were added to GINS-coupled beads in 5 µl
607 (western/silver-scale) or 20 µl (coomassie-scale) interaction buffer. For PolE2-N, 1 µM PolE2-
608 N protein in 20 µl were used for GINS-coupled beads in 5 µl reaction buffer. After incubation

609 for 45 min at 4°C rotating, beads were washed three times for 5 min with interaction buffer and
610 boiled in 50 µl Laemmli buffer before SDS PAGE.
611
612 **Pulldown from cell lysates with recombinant TopBP1-1-766-strep (BRCT0-5)**
613 For pulldown assays from soluble lysates of non-transfected 293T cells, 5 µl streptactin
614 Sepharose HP (Cytiva, 28935599) beads were coupled with 10 µg recombinant TopBP1-1-
615 766-strep-WT or mutants in coupling buffer (20 mM HEPES pH8.0, 150mM NaCl, 0.1% (v/v)
616 Tween-20, 0.5mM TCEP, 2% (v/v) glycerol) for 45 min at 4 °C before washing two times with
617 coupling buffer and then once in cell lysis buffer (20 mM HEPES pH8.0, 150mM NaCl, 0.1%
618 (v/v) Tween-20, 0.5mM TCEP, 2% (v/v) glycerol, protease inhibitor cocktail (Roche Complete
619 protease inhibitor cocktail, 05056489001). Control pulldowns were done with Flag-peptide-
620 coupled beads or, when indicated, using GINS-coupled beads and the non-GINS binding
621 TopBP1-Gcc-B4mut. 293T cells were lysed in ten times pellet volume of cell lysis buffer, and
622 centrifuged at 20,000 g for 15 min at 4 °C. Soluble lysate from cells equivalent to 50 % of a 15
623 cm tissue culture plate was added to the TopBP1-coupled beads and incubated for 2 h at 4°C
624 rotating. Beads were washed three times with 5 min incubation in lysis buffer and boiled in 50
625 µl Laemmli buffer before SDS PAGE.
626
627 **Generation of replicating *Xenopus* egg extracts**
628 *Xenopus laevis* egg extracts were prepared from metaphase II arrested eggs as described in [76].
629 After washing with MMR (100 mM NaCl, 2 mM KCl, 1 mM $MgCl_2$, 2 mM $CaCl_2$, 0.1 mM
630 EDTA, 5 mM HEPES–NaOH, pH 7.8) eggs were dejellied (2% cysteine w:v in H_2O, pH 7.8
631 with NaOH). Eggs were rinsed in XBE2 (100 mM KCl, 2 mM $MgCl_2$, 0.1 mM $CaCl_2$, 1.71 %
632 w:v sucrose, 5 mM K-EGTA, 10 mM HEPES-KOH, pH 7.7). Then, the eggs were transferred
633 into centrifuge tubes containing 1 ml XBE2 + 10 µg/ ml protease inhibitor (aprotinin Sigma
634 A6279, leupeptin Merck 108975, pepstatin Carl Roth 2936.1) + 100 µg/ ml cytochalasin D
635 (Sigma C8273). For packing, eggs were centrifuged for 1 min at 1,400 g at 16 °C in a swingout
636 rotor. Excess buffer, activated and apoptotic eggs were removed before crushing the eggs at
637 16,000 g for 10 min at 16 °C. The extract was collected with a 20 G needle and supplemented
638 with 10 µg/ml cytochalasin D, 10 µg/ml protease inhibitors, 1:80 dilution of energy regenerator
639 (1M phosphocreatine K salt, 600 µg/ ml creatine phosphokinase in 10 mM HEPES–KOH pH
640 7.6) and LFB1/50 (10% w:v sucrose, 50 mM KCl, 2 mM $MgCl_2$, 1 mM EGTA, 2 mM DTT,
641 20 mM K_2HPO_4/KH_2PO_4 pH 8.0, 40 mM HEPES–KOH, pH 8.0) to 15 % (v:v). The extract
642 was cleared at 84,000 g at 4 °C for 20 min in a swingout rotor. The cytoplasmatic layer was
643 collected and supplemented with 2 % glycerol v:v. The extract was frozen by dropping 20 µl
644 aliqouts into liquid nitrogen and stored at - 80 °C.
645
646 **Immunodepletion of TopBP1 from *Xenopus* egg extract:**
647 For XTopBP1 depletion from *Xenopus* egg extract, 0.5 µg antibody #1, #2 or IgG (rabbit; self-
648 made) were coupled per µl magnetic Protein G dynabeads (Life Technologies 10004D) for 1 h
649 at RT. Freshly thawed extracts were supplemented with 1/40 energy regenerator and 250 µg/ml
650 cycloheximide and released into interphase by adding 0.3 mM $CaCl_2$ for 15 min at 23 °C.
651 Subsequently, extracts were depleted for 45 min on ice with 0.675 µg antibody per µl extract.

After depletion the extract was aliquoted, snap frozen and stored at - 80 °C for replication assays and chromatin isolations.

Xenopus egg extract replication assays

For TopBP1 addback experiments, 6 ng/ µl recombinant TopBP1 protein or buffer were added to TopBP1 immunodepleted interphase *Xenopus* egg extract containing 50 nCi/µl α^{32}P-dCTP (Perkin Elmer NEG513A250UC). To start the replication reaction the egg extracts were supplemented with 5 ng sperm DNA (kindly provided by the lab of O. Stemmann) per µl extract and incubated at 23°C. 1 µl extract was spotted for each time point onto a glass fibre membrane. Unbound α^{32}P-dCTP was removed by rinsing the membrane three times 15 min with ice cold 5 % TCA in water and once with ice cold EtOH. Newly replicated DNA was detected by phospho-imaging. Standard error of the mean was calculated from three independent experiments.

Chromatin isolation from *Xenopus* egg extracts and analysis by mass spectrometry (CHROMASS) and western blotting

For chromatin isolation, XTopBP1-depleted interphase egg extract was supplemented with 50 µg/ml aphidicolin and aliquoted into 15 µl samples before addition of buffer or recombinant TopBP1 to a final concentration 6 ng/µl. 2.25 µM Xgeminin or buffer were added before incubation for 10 min on ice. To start the replication, 9 ng sperm DNA/µl extract was added and incubated for 75 min at 23°C. Reactions were stopped with 300 µl ice cold ELB salt (10 mM HEPES-KOH pH 7.7, 50 mM KCl, 2.5 mM $MgCl_2$) + 250 mM sucrose + 0.6 % triton X-100. The diluted extract was loaded onto a sucrose cushion (150 µl ELB salt + 25 % sucrose) and centrifuged for 10 min at 2500 g at 4 °C in a swingout rotor. The supernatant above the sucrose cushion was removed and the cushion surface was washed twice with 200 µl ELB salt containing 250 mM sucrose. The cushion was removed leaving about 15 µl behind, followed by centrifugation for 2 min at 10,000 g at 4 °C in a fixed angle rotor. For western blotting, the chromatin pellet was resuspended in 24 µl 1x Laemmli SDS sample buffer (6.5 % glycerol, 715 mM β-mercaptoethanol, 3% SDS, 62.5 mM Tris-HCl pH 7.9, 0.005 % bromphenol blue) and 5 µl were separated by denaturing SDS PAGE. For MS analysis, four biological replicates of chromatin pellets were analysed by CHROMASS [43]. In brief, chromatin pellets were resuspended in 50 µl denaturation buffer (8 M Urea; 100 mM Tris pH 8). Dithiothreitol (DTT) was added to a final concentration of 5 mM and samples were incubated at 22 °C for 30 minutes. To alkylate peptides, iodoacetamide (20 mM) was added and samples were incubated at 37 °C for 30 minutes. DTT (25 mM) was added, and samples were incubated at 22 °C for 5 minutes. 500 ng Lys-C (add Supplier) were added, and samples were incubated at 37 °C for 3 hours. Samples were diluted with 100 mM ammonium bicarbonate to adjust the urea concentration to 1 M. Trypsin (Sigma, 500 ng per sample) was added and samples were incubated over night at 37 °C. Digested peptides were acidified with 1 % trifluoroacetic acid (TFA) and desalted on Empore C18 material according to Rappsilber et al. *https://www.nature.com/articles/nprot.2007.261).* Eluted peptides were dried in a vacuum concentrator and reconstituted with 9 µl of buffer A (0.1% formic acid) containing 0.2% acetonitrile and 0.01% trifluoro acetic acid. For MS analysis, 4 µl of the reconstituted peptides were separated on an EASY-nLC™ 1200 chromatography system (Thermo Scientific) coupled

696 to a Q Exactive HF-X Orbitrap LC-MS/MS System (Thermo Fisher Scientific) via a Nanoflex
697 ion source. Peptide separation was carried out in analytical columns (50 cm, 75 µm inner
698 diameter packed in-house with C18 resin ReproSilPur 120, 1.9 µm diameter Dr. Maisch) using
699 a 3-hour non-linear gradient at a flow rate of 250 nl/minute using buffer A (aqueous 0.1%
700 formic acid) and buffer B (80 % acetonitrile, 0.1% formic acid). MS data was acquired in data-
701 dependent fashion using a Top15 method. The exact parameters for chromatography and MS
702 instrument settings can be retrieved from the raw files available at ProteomeXchange
703 (PXD040024).
704 MS data files from single-shot experiments were processed with MaxQuant (version 2.0.1.0)
705 using a non-redundant *Xenopus laevis* data base available at ProteomExchange (PXD040024)
706 [43]. Raw data were normalized using the label-free quantitation (LFQ) algorithm implemented
707 in MaxQuant. MS Data with Perseus (version 1.6.15.0) [77]. Protein groups were filtered to
708 eliminate contaminants, reverse hits, and proteins identified by site only. For the heat map (Fig.
709 6a) LFQ intensities were log2 transformed and for each protein z-scores were calculated across
710 all replicates (N=4) of all four conditions. Subsequently, the average of the z-scores was
711 calculated for each condition and selected proteins were plotted (see suppl. table 2 for the z-
712 score of all proteins). Proteins were manually annotated and sorted according to their function
713 in DNA replication and DNA repair. To identify proteins with significant abundance changes
714 between the four conditions, LFQ intensities were log2 transformed and missing values were
715 imputed with random values drawn from a normal distribution centred around the detection
716 limit of the MS instrument (Perseus imputation; width=0.3, down shift = 1.8). Two sample
717 Student's t-tests with permutation-based FDR control were carried out in Perseus. For these
718 tests three valid values in at least one quadruplicate of either of the tested conditions was
719 required. FDR was adjusted for multiple testing by the Benjamini-Hochberg procedure using
720 a significance threshold of FDR<0.05 (see suppl. table 2). Data visualisation was carried out
721 in R. All scripts are available upon request.
722
723 **Determination of TopBP1-proximal proteins by APEX2 biotinylation**
724 *Sample preparation:*
725 Proximity labelling was performed in isogenic stable 293 Flip-In (Thermo Fisher; R75007)
726 cells stably expressing TopBP1 N-terminal tagged with APEX2 or in 293T cells transiently
727 expressing either N-terminal or C-terminally APEX2-tagged TopBP1. 24 h before transfection,
728 0.8 x 10^6 cells were seeded onto a 6 cm plate. For each condition, four dishes were separately
729 transfected (biological replicates). One day after transfection, cells were incubated for 30 min
730 with 500 µM biotin phenol at 37 °C, before incubation for 1 min at RT with or without
731 (controls) 1 mM H_2O_2. The medium was discarded, and cells were washed three times with
732 quenching buffer (10 mM sodium azide, 10 mM sodium ascorbate and 5 mM Trolox in
733 Dulbecco's PBS (Life Technologies 14190169). Cells were rinsed off the dishes with DPBS,
734 transferred into reaction tubes before washing again with DPBS. Cells were lysed at 95 °C for
735 10 min in TSD buffer (50 mM Tris pH 7.5, 5 mM DTT and 1 % SDS). Samples were diluted
736 ten times with TNN buffer (20 mM Tris pH 7.9, 200 mM NaCl and 0.5 % NP-40 alternative)
737 and benzonase (75 U per sample) (Sigma E1014). Samples were incubated for 15 min at 4 °C
738 and centrifuged at 21000 g for 2 min at 4 °C. Supernatants were incubated over night with 15
739 µl streptavidin sepharose beads (Sigma GE17-5113-01) at 4 °C. Beads were washed once with

740 TNN buffer + 0.1% SDS and twice with 25 mM ammonium bicarbonate before processing for
741 mass spectrometry. For this, captured proteins were washed two times with H_2O prior to on-
742 bead digestion to remove MS incompatible buffer components. The beads were taken up in
743 100 µl 0.8 M urea, 50 mM ammonium bicarbonate buffer (ABC) and supplemented with 5 mM
744 DTT. After incubation at 37°C for 30 min, 10 mM iodoacetamide (IAM) was added and
745 incubated for 30 min at room temperature in the dark while shaking at 1500 rpm (Thermomixer
746 C, Eppendorf). The IAM was quenched with 11 mM DTT. Trypsin was added to a total of 300
747 ng Trypsin per sample. The samples were incubated over night at 37°C, shaking at 1150 rpm
748 before stopping by 1% (vol/vol) formic acid (FA). After bead collection by centrifugation (650
749 g, 5 min) 100 µl supernatant were transferred to a Eppendorf Lo-bind 1.5 mL tube. The
750 remaining beads were incubated with 50 µl 1 % formic acid for (1150 rpm, 5 min rpm, RT)
751 and after collecting the beads once more by centrifugation (650 g, 5 min) the supernatant was
752 combined with the first one. The sepharose beads were discarded. To remove residual
753 sepharose beads, the combined peptide containing solutions were passed over pre-equilibrated
754 (50 µl 0.5 % formic acid) home-made 2-disc Glass microfiber StageTip (disc material: GE
755 Healthcare; pore size: 1.2 µM; thickness: 0.26 mm; 50× g 2 min). The cleared tryptic digests
756 were then desalted on home-made C18 StageTips as described [78]. Briefly, peptides were
757 immobilized and washed on a 2 disc C18 (Empore) StageTip. After elution from the StageTips,
758 samples were dried using a vacuum concentrator (Eppendorf) and the peptides were taken up
759 in 0.1% formic acid solution (10-15 µL) and directly used for LC-MS/MS experiments.
760 *LC-MS/MS settings:*
761 MS Experiments were performed on an Orbitrap Fusion LUMOS instrument (Thermo) coupled
762 to an EASY-nLC 1200 ultra-performance liquid chromatography (UPLC) system (Thermo).
763 The UPLC was operated in the one-column mode. The analytical column was a fused silica
764 capillary (75 µm × 46 cm) with an integrated fritted emitter (CoAnn Technologies) packed in-
765 house with Kinetex 1.7 µm C18-XB core shell beads (Phenomenex). The analytical column
766 was encased by a column oven (Sonation PRSO-V2) and attached to a nanospray flex ion
767 source (Thermo). The column oven temperature was set to 50 °C during sample loading and
768 data acquisition. The LC was equipped with two mobile phases: solvent A (0.2% FA, 2%
769 Acetonitrile, ACN, 97.8% H_2O) and solvent B (0.2% FA, 80% ACN, 19.8% H_2O). All solvents
770 were of UPLC grade (Honeywell). Peptides were directly loaded onto the analytical column
771 with a maximum flow rate that would not exceed the set pressure limit of 980 bar (usually
772 around 0.4 – 0.6 µL/min). Peptides were subsequently separated on the analytical column by
773 running a 105 min gradient of solvent A and solvent B (start with 3% B; gradient 3% to 9% B
774 for 6:30 min; gradient 9% to 30% B for 62:30 min; gradient 30% to 50% B for 24:00 min; 50%
775 to 100% B for 2:30 min; 100% for 9:30 min) at a flow rate of 300 nl/min. The mass
776 spectrometer was controlled by the Orbitrap Fusion Lumos Tune Application (version
777 3.3.2782.28) and operated using the Xcalibur software (version 4.3.73.11). The mass
778 spectrometer was set in the positive ion mode. The ionization potential (spray voltage) was set
779 to 2.5 kV. Source fragmentation was turned off. Precursor ion scanning was performed in the
780 Orbitrap analyser (FT; fourier transform mass spectrometer) in the scan range of m/z 370-1500
781 and at a resolution of 240000 with the internal lock mass option turned on (lock mass was
782 445.120025 m/z, polysiloxane) [79]. AGC (automatic gain control) was set to "standard" and
783 acquisition time to "auto". Product ion spectra were recorded in a data dependent fashion in

784 the IT (IT; ion trap mass spectrometer) in a variable scan range ("auto") and at "rapid" scan
785 rate. Peptides were analysed using a "top speed" regime (repeating cycle of full precursor ion
786 scan (AGC target "300%"; acquisition time "auto") followed by dependent MS2 scans for 3
787 seconds (minimum intensity threshold 4×10^3)). The MS2 precursor ions were isolated using
788 the quadrupole (isolation window 1.6 m/z) and fragmentation was achieved by Higher-energy
789 C-trap dissociation (HCD) (normalized collision mode set to "stepped" and normalized
790 collision energy set to "27, 32, 40%"). During MS2 data acquisition dynamic ion exclusion
791 was set to 20 seconds. Only charge states between 2-7 were considered for fragmentation.
792 *Data processing:*
793 RAW spectra were submitted to an Andromeda [80] search in MaxQuant (v2.0.3.0) using the
794 default settings (Cox & Mann 2008) [81]. Label-free quantification and match-between-runs was
795 activated [82]. The MS/MS spectra data were searched against the Uniprot *H. sapiens* reference
796 database (one protein per gene; UP000005640_9606_OPPG.fasta, 20585 entries, downloaded
797 1/10/2022) and a dedicated database containing the APEX2-myc sequence
798 (ACE_0741_SOI_v01.fasta; 1 entry). All searches included a contaminants database search (as
799 implemented in MaxQuant, 246 entries). The contaminants database contains known MS
800 contaminants and was included to estimate the level of contamination. Andromeda searches
801 allowed oxidation of methionine residues (16 Da) and acetylation of the protein N-terminus
802 (42 Da) as dynamic modifications and the static modification of cysteine (57 Da, alkylation
803 with iodoacetamide). Enzyme specificity was set to "Trypsin/P" with two missed cleavages
804 allowed. The instrument type in Andromeda searches was set to Orbitrap and the precursor
805 mass tolerance was set to ± 20 ppm (first search) and ± 4.5 ppm (main search). The MS/MS
806 match tolerance was set to ± 0.5 Da. The peptide spectrum match FDR and the protein FDR
807 were set to 0.01 (based on target-decoy approach). Minimum peptide length was 7 aa. For
808 protein quantification unique and razor peptides were allowed. Modified peptides were allowed
809 for quantification. The minimum score for modified peptides was 40. Label-free protein
810 quantification was switched on, and unique and razor peptides were considered for
811 quantification with a minimum ratio count of 2. Retention times were recalibrated based on the
812 built-in nonlinear time-rescaling algorithm. MS/MS identifications were transferred between
813 LC-MS/MS runs with the "match between runs" option in which the maximal match time
814 window was set to 0.7 min and the alignment time window set to 20 min. The quantification is
815 based on the "value at maximum" of the extracted ion current. At least two quantitation events
816 were required for a quantifiable protein. Further analysis and filtering of the results was done
817 in Perseus v1.6.10.0. [77]. For quantification we combined related biological replicates to
818 categorical groups and investigated only those proteins that were found in at least one
819 categorical group in a minimum of 3 out of 4 biological replicates. Comparison of protein
820 group quantities (relative quantification) between different MS runs is based solely on the
821 LFQ's as calculated by MaxQuant, MaxLFQ algorithm [82].
822
823 **Analysis of the TopBP1-GINS by cross-linking mass spectrometry**
824 *Sample preparation*
825 50 µg (1.15 µg/µl) of each GINS and TopBP1-BRCT0-5-strep (amino acids 1-766) were
826 incubated for 45 min on ice in cross-linking buffer (20mM HEPES pH8.0, 150mM NaCl,
827 0.01% Tween20, 2% Glycerol, 0.5mM TCEP). 600 µM or 2500 µM of BS^3 crosslinker were

828 added and incubated for 30 min at 35 °C shaking. The reaction was stopped by adding
829 ammonium bicarbonate to a final concentration of 100 mM. 90 % of the cross-linked sample
830 was used for mass spectrometry analysis of crosslinks. 10% of the reaction were separated by
831 SDS-PAGE . The coomassie-stained gel was cut in slices above the molecular weight of
832 monomeric TopBP1-BRCT0-5-strep for subsequent mass spectrometry.
833 Sample *processing for mass spectrometry*
834 Sample preparation of crosslinked samples for LC/MS/MS is based on the SP3 protocol [83]. 30
835 µg of protein from each cross-linking sample was taken up in 100 µl 1× SP3 lysis buffer (final
836 concentrations: 5% (wt/vol) SDS; 10 mM TCEP; 200 µL 40 mM chloracetamide; 200 mM
837 HEPES pH 8) and heated for 5 min at 90 °C. After cooling the samples to room temperature
838 (on ice) a mix of 150 µg hydrophobic (#65152105050250) and 150 µg hydrophilic
839 (#45152105050250) SeraMag Speed Beads (Cytiva) was added (bead to protein ratio 10 to 1)
840 and gently mixed. Then 100 µL 100% vol/vol Ethanol (EtOH) was added before incubation
841 for 20 min at 24°C shaking vigorously. The beads were collected on a magnet and the
842 supernatant aspirated. The beads were then washed 4 times with 180 µL 80 % EtOH (collection
843 time on the magnet minimum of 4 min). The beads were then finally taken up in 100 µL 25
844 mM ammoniumbicarbonate (ABC) containing 1 µg Trypsin (Protein:Trypsin ratio 30:1). To
845 help bead dissociation, samples were incubated for 5 min in a sonification bath (preheated to
846 37°C). Samples were incubated over night shaking at vigorously. Samples were acidified with
847 formic acid (FA, final 1% vol/vol) before collection on a magnet. The supernatants were
848 transferred to a fresh Eppendorf tube, before removing trace beads using a magnet for 5 min.
849 The tryptic digests were then desalted on home-made C18 StageTips as described [78]. Briefly,
850 peptides were immobilized and washed on a 2 disc C18 StageTip. Samples were then dried
851 using a vacuum concentrator (Eppendorf) and the peptides were taken up in 0.1% formic acid
852 solution (10 µL) and directly used for LC-MS/MS experiments.
853 *LC-MS/MS settings crosslinking mass spectrometry:*
854 MS Experiments were performed on an Orbitrap Fusion LUMOS instrument (Thermo) coupled
855 to an EASY-nLC 1200 ultra-performance liquid chromatography (UPLC) system (Thermo).
856 The UPLC was operated in the one-column mode. The analytical column was a fused silica
857 capillary (75 µm × 41 cm) with an integrated fritted emitter (CoAnn Technologies) packed in-
858 house with Kinetex 1.7 µm C18-XB core shell beads (Phenomenex). The analytical column
859 was encased by a column oven (Sonation PRSO-V2) and attached to a nanospray flex ion
860 source (Thermo). The column oven temperature was set to 50 °C during sample loading and
861 data acquisition. The LC was equipped with two mobile phases: solvent A (0.2% FA, 2%
862 Acetonitrile, ACN, 97.8% H_2O) and solvent B (0.2% FA, 80% ACN, 19.8% H_2O). All solvents
863 were of UPLC grade (Honeywell). Peptides were directly loaded onto the analytical column
864 with a maximum flow rate that would not exceed the set pressure limit of 980 bar (usually
865 around 0.4 – 0.6 µL/min). Peptides were subsequently separated on the analytical column by
866 running a 70 min gradient of solvent A and solvent B (start with 2% B; gradient 2% to 6% B
867 for 5:00 min; gradient 6% to 25% B for 42:00 min; gradient 25% to 40% B for 15:00 min; 40%
868 to 98% B for 1:00 min; 98% for 7:00 min) at a flow rate of 350 nl/min. The mass spectrometer
869 was controlled by the Orbitrap Fusion Lumos Tune Application (version 3.3.2782.28) and
870 operated using the Xcalibur software (version 4.3.73.11). The mass spectrometer was set in the
871 positive ion mode. The ionization potential (spray voltage) was set to 2.5 kV. Source

872 fragmentation was turned off. Precursor ion scanning was performed in the Orbitrap analyser
873 (FT; fourier transform mass spectrometer) in the scan range of m/z 370-1600 and at a resolution
874 of 120000 with the internal lock mass option turned on (lock mass was 445.120025 m/z,
875 polysiloxane) [79]. AGC (automatic gain control) was set to "standard" and acquisition time to
876 "auto". Product ion spectra were recorded in a data dependent fashion in the FT in a variable
877 scan range ("auto") and at 15000 resolution. Peptides were analysed using a "top speed" regime
878 (repeating cycle of full precursor ion scan (AGC target "standard"; acquisition time "200ms")
879 followed by dependent MS2 scans for 5 seconds (minimum intensity threshold 2×10^4). The
880 MS2 precursor ions were isolated using the quadrupole (isolation window 2.0 m/z) and
881 fragmentation was achieved by Higher-energy C-trap dissociation (HCD) (normalized
882 collision mode set to "stepped" and normalized collision energy set to "27, 30, 33%"). During
883 MS2 data acquisition dynamic ion exclusion was set to 60 seconds. Only charge states between
884 3-7 were considered for fragmentation.
885 *Data processing protocol:*
886 The searches for crosslinked peptides were performed with two different search engines:
887 MetaMorpheus (MM) version 0.0.320 [84] and pLink2 version v2.3.9. [85]. Searches were
888 performed on the Thermo RAW files using the database ACE_0704_SOI_plus_con_v01.fasta
889 (244 entries). The database contains the sequences for TopBP1 (1-766), PsfI, PsFII, PsfIII,
890 Sld5 and 239 known contaminating proteins found in MS samples. The peptide spectrum match
891 FDR for MM was 0.01 and for pLink2 0.05 (based on target-decoy approach, decoys are
892 generated by the software). The settings for MetaMorpheus were: crosslinker name = DSS
893 _KSTY (note: DSS and BS^3 have identical crosslinker size); crosslinker type = non-cleavable;
894 crosslinker mass = 138.06808; crosslinker modification site 1 = K; crosslinker modification
895 site 2 = KSTY; protease = trypsin; maximum missed cleavages = 3; minimum peptide length
896 = 5; maximum peptide length = 60; initiator methionine behaviour = Variable; max
897 modification isoforms = 1024; fixed modifications = Carbamidomethyl on C, variable
898 modifications = Oxidation on M; parent mass tolerance(s) = ±10 ppm; product mass tolerance
899 = ±20 ppm. The settings for pLink2 were: crosslinker name = DSS-BS^3-KSTY; crosslinker
900 type = non-cleavable; crosslinker mass = 138.06808; crosslinker modification site 1 = K;
901 crosslinker modification site 2 = KSTY; protease = trypsin; maximum missed cleavages = 3;
902 minimum peptide length = 6; maximum peptide length = 60; fixed modifications =
903 Carbamidomethyl on C, variable modifications = Oxidation on M; parent mass tolerance(s) =
904 ±20 ppm; product mass tolerance = ±20 ppm. The results from both searches were converted
905 to the ProXL XML format using the respective converters (metaMorph2ProxlXML.jar,
906 plink2toProxlXML.jar, follow links on the ProXL website; https://proxl-ms.org/) and uploaded
907 to the ProXL server [86]. Analysis and evaluation of crosslinks was performed on our local ProXL
908 Server. The results from both searches was analysed together.
909
910 **Computational modeling**
911 Locally implemented AlphaFold2-Multimer version 2.2.0 [87] was used to predict the binding
912 interfaces of GINS and TopBP1 using the full-length sequences of each GINS subunit and
913 residues 301-766 of human TopBP1. 5 models were obtained, using 5 seeds per model, by
914 default and ranked with the combined score of ipTM+pTM implemented in AlphaFold2-

915 Multimer [87, 88]. The top ranked model used for figure production and statistical plots were
916 produced using Alphapickle 1.5.4 for the top seed from each model.
917 Blind molecular docking for insight into the GINI binding region used the GINI sequence
918 DEDLLSQY of TopBP1 (residues 487-494) in the servers Cluspro [89] (accessed on
919 13/06/2022), HPEPDOCK [90] (accessed on 13/06/2022), and MDockPeP [91 92, 93] (accessed on
920 13/06/2022) web servers with 200 solutions per server. We further extended, refined, and re-
921 scored the sampling, by generating 10 additional conformations per web server solution (for a
922 total of 6000 solutions) with FlexPepDock [94]. The top-10 best-scored solutions were selected
923 for analysis and visualization.
924 The binding free energies of GINS with BRCT4 and GINI were estimated based on the best
925 scored AlphaFold2 model using the web servers PRODIGY [95] and PPI-Affinity [96]. The region
926 of GINI employed for the estimation comprised residues 481 to 496. Both PRODIGY and PPI-
927 Affinity analyze the residues in the binding interface for free energy estimation. PRODIGY
928 uses a linear amino acid chain model, whilst PPI-Affinity uses a structure-based machine
929 learning algorithm.
930
931 **Cryo-electron microscopy**
932 ***Grid preparation***
933 Quantifoil 1.2/1.3, 300 mesh copper grids (Quantifoil) were glow discharged using a Tergeo
934 Plasma Cleaner (Pie Scientific) with an indirect plasma treatment for 30 seconds. Grids were
935 loaded into a Leica EM GP2 (Leica microsystems) and 3 µl of peak fractions from size
936 exclusion chromatography were diluted to 0.1 mg/ml and applied to the front of the grid, with
937 an additional 0.5 µl buffer applied to the grids rear, before back blotting for 3 seconds and
938 plunging into an ethane propane mix.
939 *Electron microscopy and data processing*
940 For dataset 1, grids were stored in liquid nitrogen prior to imaging at 300 kV on a FEI Titan
941 Krios (Thermo Fisher Scientific) equipped with K3 detector (Gatan). 18945 movies were
942 collected, using data acquisition software EPU (Thermo Fisher Scientific), at a magnification
943 of 105000 and a pixel size of 0.85Å using a total dose of 50 e-/Å2. These were motion corrected
944 in 5x5 patches using MOTIONCOR2 [97] implemented in RELION4.0 [42] before importing into
945 cryoSPARC [41]. Micrographs were CTF corrected prior to blob picking and extraction of an
946 initial set of particles. Subsequent filtering by 2D classification removed most of these leaving
947 a cleaned set of particles that were used to produce 4 initial models. The 2D classes and initial
948 models appeared to have at least two distinct sub populations, one containing just the GINS
949 complex alone and one that also had some additional density. In order to distinguish between
950 these two sets of particles heterorefinement was performed to split the two groups. The first
951 population of particles containing only the GINS complex were then imported into
952 RELION4.0 before several cycles of 3D classification, to yield a final set of 111455 particles
953 that gave a volume at 5.9 Å resolution used to produce the GINS alone volume used in
954 (supplementary Fig. S15c). The second group of TOPBP1-GINS particles were used to train a
955 TOPAZ model before implementing further picking using TOPAZ [98]. The resulting particles
956 were again filtered by rounds of 2D classification and heterorefinement before exporting the
957 particles, that appeared to consist of the full TOPBP1-GINS complex, into RELION4.0.
958 Several cycles of 3D classification were then performed with classes appearing to lack the

additional density eliminated, to yield a final set of 208115 particles. 3D refinement and post-processing of these gave a volume at 4.71Å resolution into which previously solved crystal structures of the GINS complex (29EX) and the central BRCT4/5 module of TopBP1 (3UEN) could be docked.

For dataset 2, grids were stored in liquid nitrogen prior to imaging at 300 kV on a FEI Titan Krios (Thermo Fisher Scientific) equipped with Fakcon 4i detector (Thermo Fisher Scientific). 8808 movies were collected, using data acquisition software EPU (Thermo Fisher Scientific), at a magnification of 120000 and a pixel size of 0.74Å using a total dose of 39.69 e-/Å2. The same processing schedule was followed as for dataset one to yield a final set of 154278 particles. 3D refinement and post-processing of these gave a volume at 4.1 Å resolution into which the previously solved model could be docked alongside the predicted GINI helix from the AlphaFold2-Multimer model. Minor adjustments to the model were made in Coot before refinement of the final model using PHENIX [99].

Data Presentation

Figure panels for all structural data were produced using ChimeraX-1.3

Data Availability

The mass spectrometry proteomics data for the proximity dependent biotinylation experiments, the cross-linking experiments and the chromatin mass spectrometry (CHROMASS) experiments have been deposited to the ProteomeXchange Consortium via the PRIDE[100] partner repository (https://www.ebi.ac.uk/pride/archive/) with the dataset identifiers PXD040000 (PDB experiments), PXD040156 (CL-MS experiments) and PXD040024 (CHROMASS experiments). During the review process the data can be accessed via the following Reviewer accounts:

PXD040000: (Username: reviewer_pxd040000@ebi.ac.uk; Password: Lk9VLXVF)

PXD040156: (Username: reviewer_pxd040156@ebi.ac.uk; Password: NLNLORQl)

PXD040024: (Username: reviewer_pxd040024@ebi.ac.uk; Password: 5OGweuE6)

Cryo-EM maps and refined coordinates have been deposited in the EMDB and Protein Databank as EMD- 16916 and PDB ID 8OK2 respectively.

Research animals

We have complied with ethical regulations. The protocol used in this study was approved by the Landesamt für Natur-, Umwelt- und Verbraucherschutz, Nordrhein-Westfalen (81-02.05.40.20.050)

References

Acknowledgements

We thank Nora Cronin, Rebecca Thompson and Daniel Maskell, Yehuda Halfon, Pascale Schelleberger and Fabienne Beuron for assistance with cryo-EM. We also thank Svenja Heimann and Jenny Bormann for technical assistance with crosslinking and APEX2 mass spectrometry and Ken L. Dreger for our local ProXL server. We further thank Stefan Westermann, Hemmo Meyer and Olaf Stemmann for sharing reagents and expertise on biochemistry and *Xenopus* egg extracts. The lab of D.B. was supported by the SFB1430 (Project-ID 424228829) and RTG1739 of the Deutsche Forschungsgemeinschaft (DFG, German Rersearch Foundation) and the NRW Rückkehrerförderprogramm (state of North-Rhine-Westphalia), the labs of A.W.O and L.H.P. by Cancer Research UK Programme Grants C302/A14532 and C302/A24386, and the lab of M.R. by the FOR2800 research group (DFG). E.S.G. acknowledges funding from the DFG under Germany´s Excellence Strategy (EXC 2033 – 390677874 – RESOLV), the instrumentation program of the DFG (436586093) and CRC1430. M.K. and F.K. are grateful for funding by the DFG (DFG, INST 20876/322-1 FUGG and CRC1430).

References

1. Siddiqui K, On KF, Diffley JF. Regulating DNA replication in eukarya. *Cold Spring Harb Perspect Biol* **5**, (2013).

2. Remus D, Beuron F, Tolun G, Griffith JD, Morris EP, Diffley JFX. Concerted loading of Mcm2-7 double hexamers around DNA during DNA replication origin licensing. *Cell* **139**, 719-730 (2009).

3. Evrin C*, et al.* A double-hexameric MCM2-7 complex is loaded onto origin DNA during licensing of eukaryotic DNA replication. *Proc Natl Acad Sci U S A* **106**, 20240-20245 (2009).

4. Li N*, et al.* Structure of the eukaryotic MCM complex at 3.8 A. *Nature* **524**, 186-191 (2015).

5. Georgescu R*, et al.* Structure of eukaryotic CMG helicase at a replication fork and implications to replisome architecture and origin initiation. *Proc Natl Acad Sci U S A* **114**, E697-E706 (2017).

6. Douglas ME, Ali FA, Costa A, Diffley JFX. The mechanism of eukaryotic CMG helicase activation. *Nature* **555**, 265-268 (2018).

7. Moyer SE, Lewis PW, Botchan MR. Isolation of the Cdc45/Mcm2-7/GINS (CMG) complex, a candidate for the eukaryotic DNA replication fork helicase. *Proc Natl Acad Sci U S A* **103**, 10236-10241 (2006).

1041 8. Ilves I, Petojevic T, Pesavento JJ, Botchan MR. Activation of the MCM2-7 helicase by
1042 association with Cdc45 and GINS proteins. *Mol Cell* **37**, 247-258 (2010).
1043
1044 9. Costa A*, et al.* DNA binding polarity, dimerization, and ATPase ring remodeling in the
1045 CMG helicase of the eukaryotic replisome. *Elife* **3**, e03273 (2014).
1046
1047 10. Yeeles JT, Deegan TD, Janska A, Early A, Diffley JF. Regulated eukaryotic DNA
1048 replication origin firing with purified proteins. *Nature* **519**, 431-435 (2015).
1049
1050 11. Lewis JS*, et al.* Mechanism of replication origin melting nucleated by CMG helicase
1051 assembly. *Nature* **606**, 1007-1014 (2022).
1052
1053 12. Meagher M, Epling LB, Enemark EJ. DNA translocation mechanism of the MCM
1054 complex and implications for replication initiation. *Nat Commun* **10**, 3117 (2019).
1055
1056 13. Kanemaki M, Labib K. Distinct roles for Sld3 and GINS during establishment and
1057 progression of eukaryotic DNA replication forks. *Embo J* **25**, 1753-1763 (2006).
1058
1059 14. Heller RC, Kang S, Lam WM, Chen S, Chan CS, Bell SP. Eukaryotic Origin-Dependent
1060 DNA Replication In Vitro Reveals Sequential Action of DDK and S-CDK Kinases. *Cell* **146**,
1061 80-91 (2011).
1062
1063 15. Francis LI, Randell JC, Takara TJ, Uchima L, Bell SP. Incorporation into the prereplicative
1064 complex activates the Mcm2-7 helicase for Cdc7-Dbf4 phosphorylation. *Genes Dev* **23**,
1065 643-654 (2009).
1066
1067 16. Greiwe JF*, et al.* Structural mechanism for the selective phosphorylation of DNA-
1068 loaded MCM double hexamers by the Dbf4-dependent kinase. *Nat Struct Mol Biol* **29**,
1069 10-20 (2022).
1070
1071 17. Saleh A*, et al.* The structural basis of Cdc7-Dbf4 kinase dependent targeting and
1072 phosphorylation of the MCM2-7 double hexamer. *Nat Commun* **13**, 2915 (2022).
1073
1074 18. Itou H, Muramatsu S, Shirakihara Y, Araki H. Crystal structure of the homology domain
1075 of the eukaryotic DNA replication proteins Sld3/Treslin. *Structure* **22**, 1341-1347
1076 (2014).
1077
1078 19. Deegan TD, Yeeles JT, Diffley JF. Phosphopeptide binding by Sld3 links Dbf4-dependent
1079 kinase to MCM replicative helicase activation. *EMBO J* **35**, 961-973 (2016).
1080
1081 20. Zegerman P, Diffley JFX. Phosphorylation of Sld2 and Sld3 by cyclin-dependent kinases
1082 promotes DNA replication in budding yeast. *Nature* **445**, 281-285 (2007).
1083
1084 21. Kumagai A, Shevchenko A, Dunphy WG. Direct regulation of Treslin by cyclin-
1085 dependent kinase is essential for the onset of DNA replication. *J Cell Biol* **193**, 995-
1086 1007 (2011).
1087

1088 22. Boos D*, et al.* Regulation of DNA Replication through Sld3-Dpb11 Interaction Is
1089 Conserved from Yeast to Humans. *Curr Biol* **21**, 1152-1157 (2011).
1090
1091 23. Tak YS, Tanaka Y, Endo S, Kamimura Y, Araki H. A CDK-catalysed regulatory
1092 phosphorylation for formation of the DNA replication complex Sld2-Dpb11. *Embo J* **25**,
1093 1987-1996 (2006).
1094
1095 24. Gambus A*, et al.* GINS maintains association of Cdc45 with MCM in replisome
1096 progression complexes at eukaryotic DNA replication forks. *Nat Cell Biol* **8**, 358-366
1097 (2006).
1098
1099 25. Sengupta S, van Deursen F, de Piccoli G, Labib K. Dpb2 integrates the leading-strand
1100 DNA polymerase into the eukaryotic replisome. *Curr Biol* **23**, 543-552 (2013).
1101
1102 26. Goswami P*, et al.* Structure of DNA-CMG-Pol epsilon elucidates the roles of the non-
1103 catalytic polymerase modules in the eukaryotic replisome. *Nat Commun* **9**, 5061
1104 (2018).
1105
1106 27. Jones ML, Baris Y, Taylor MRG, Yeeles JTP. Structure of a human replisome shows the
1107 organisation and interactions of a DNA replication machine. *EMBO J* **40**, e108819
1108 (2021).
1109
1110 28. Day M, Oliver AW, Pearl LH. Phosphorylation-dependent assembly of DNA damage
1111 response systems and the central roles of TOPBP1. *DNA Repair (Amst)* **108**, 103232
1112 (2021).
1113
1114 29. Makiniemi M*, et al.* BRCT domain-containing protein TopBP1 functions in DNA
1115 replication and damage response. *J Biol Chem* **276**, 30399-30406 (2001).
1116
1117 30. Kumagai A, Shevchenko A, Dunphy WG. Treslin collaborates with TopBP1 in triggering
1118 the initiation of DNA replication. *Cell* **140**, 349-359 (2010).
1119
1120 31. Tanaka S, Komeda Y, Umemori T, Kubota Y, Takisawa H, Araki H. Efficient initiation of
1121 DNA replication in eukaryotes requires Dpb11/TopBP1-GINS interaction. *Mol Cell Biol*
1122 **33**, 2614-2622 (2013).
1123
1124 32. Mantiero D, Mackenzie A, Donaldson A, Zegerman P. Limiting replication initiation
1125 factors execute the temporal programme of origin firing in budding yeast. *EMBO J* **30**,
1126 4805-4814 (2011).
1127
1128 33. Tanaka S, Nakato R, Katou Y, Shirahige K, Araki H. Origin association of Sld3, Sld7, and
1129 Cdc45 proteins is a key step for determination of origin-firing timing. *Curr Biol* **21**,
1130 2055-2063 (2011).
1131
1132 34. Collart C, Allen GE, Bradshaw CR, Smith JC, Zegerman P. Titration of four replication
1133 factors is essential for the Xenopus laevis midblastula transition. *Science* **341**, 893-896
1134 (2013).

1135
1136 35. Jenkinson F, Tan KW, Schopf B, Santos MM, Zegerman P. Dephosphorylation of the
1137 pre-initiation complex is critical for origin firing. *Mol Cell* **83**, 12-25 e10 (2023).
1138
1139 36. Lim Y*, et al.* In silico protein interaction screening uncovers DONSON's role in
1140 replication initiation. *Science*, eadi3448 (2023).
1141
1142 37. Xia Y*, et al.* DNSN-1 recruits GINS for CMG helicase assembly during DNA replication
1143 initiation in Caenorhabditis elegans. *Science*, eadi4932 (2023).
1144
1145 38. Kingsley G*, et al.* DONSON facilitates Cdc45 and GINS chromatin association and is
1146 essential for DNA replication initiation. *Nucleic Acids Res*, (2023).
1147
1148 39. Hashimoto Y, Sadano K, Miyata N, Ito H, Tanaka H. Novel role of DONSON in CMG
1149 helicase assembly during vertebrate DNA replication initiation. *EMBO J*, e114131
1150 (2023).
1151
1152 40. Bigot N, Day M, Baldock RA, Watts FZ, Oliver AW, Pearl LH. Phosphorylation-mediated
1153 interactions with TOPBP1 couple 53BP1 and 9-1-1 to control the G1 DNA damage
1154 checkpoint. *Elife* **8**, (2019).
1155
1156 41. Punjani A, Rubinstein JL, Fleet DJ, Brubaker MA. cryoSPARC: algorithms for rapid
1157 unsupervised cryo-EM structure determination. *Nat Methods* **14**, 290-296 (2017).
1158
1159 42. Leung CC*, et al.* Structural insights into recognition of MDC1 by TopBP1 in DNA
1160 replication checkpoint control. *Structure* **21**, 1450-1459 (2013).
1161
1162 43. Raschle M*, et al.* DNA repair. Proteomics reveals dynamic assembly of repair
1163 complexes during bypass of DNA cross-links. *Science* **348**, 1253671 (2015).
1164
1165 44. Kamada K, Kubota Y, Arata T, Shindo Y, Hanaoka F. Structure of the human GINS
1166 complex and its assembly and functional interface in replication initiation. *Nat Struct*
1167 *Mol Biol* **14**, 388-396 (2007).
1168
1169 45. Chang YP, Wang G, Bermudez V, Hurwitz J, Chen XS. Crystal structure of the GINS
1170 complex and functional insights into its role in DNA replication. *Proc Natl Acad Sci U S*
1171 *A* **104**, 12685-12690 (2007).
1172
1173 46. De Jesus-Kim L, Friedman LJ, Looke M, Ramsoomair CK, Gelles J, Bell SP. DDK regulates
1174 replication initiation by controlling the multiplicity of Cdc45-GINS binding to Mcm2-7.
1175 *Elife* **10**, (2021).
1176
1177 47. Looke M, Maloney MF, Bell SP. Mcm10 regulates DNA replication elongation by
1178 stimulating the CMG replicative helicase. *Genes Dev* **31**, 291-305 (2017).
1179

1180 48. Douglas ME, Diffley JFX. Recruitment of Mcm10 to Sites of Replication Initiation
1181 Requires Direct Binding to the Minichromosome Maintenance (MCM) Complex. *J Biol*
1182 *Chem* **291**, 5879-5888 (2016).
1183
1184 49. Costa A, Diffley JFX. The Initiation of Eukaryotic DNA Replication. *Annu Rev Biochem*
1185 **91**, 107-131 (2022).
1186
1187 50. Zegerman P, Diffley JFX. Checkpoint-dependent inhibition of DNA replication initiation
1188 by Sld3 and Dbf4 phosphorylation. *Nature* **467**, 474-478 (2010).
1189
1190 51. Lopez-Mosqueda J, Maas NL, Jonsson ZO, Defazio-Eli LG, Wohlschlegel J, Toczyski DP.
1191 Damage-induced phosphorylation of Sld3 is important to block late origin firing.
1192 *Nature* **467**, 479-483 (2010).
1193
1194 52. Natsume T*, et al.* Kinetochores coordinate pericentromeric cohesion and early DNA
1195 replication by Cdc7-Dbf4 kinase recruitment. *Mol Cell* **50**, 661-674 (2013).
1196
1197 53. Reusswig KU, Zimmermann F, Galanti L, Pfander B. Robust Replication Control Is
1198 Generated by Temporal Gaps between Licensing and Firing Phases and Depends on
1199 Degradation of Firing Factor Sld2. *Cell Rep* **17**, 556-569 (2016).
1200
1201 54. Tanaka S. Interaction of replication factor Sld3 and histone acetyl transferase Esa1
1202 alleviates gene silencing and promotes the activation of late and dormant replication
1203 origins. *Genetics* **217**, 1-11 (2021).
1204
1205 55. Sansam CG*, et al.* A mechanism for epigenetic control of DNA replication. *Genes Dev*
1206 **32**, 224-229 (2018).
1207
1208 56. Wittig KA, Sansam CG, Noble TD, Goins D, Sansam CL. The CRL4DTL E3 ligase induces
1209 degradation of the DNA replication initiation factor TICRR/TRESLIN specifically during
1210 S phase. *Nucleic Acids Res* **49**, 10507-10523 (2021).
1211
1212 57. Johnson MC, Can G, Santos MM, Alexander D, Zegerman P. Checkpoint inhibition of
1213 origin firing prevents inappropriate replication outside of S-phase. *Elife* **10**, (2021).
1214
1215 58. Ferreira P*, et al.* MTBP phosphorylation controls DNA replication origin firing. *Sci Rep*
1216 **11**, 4242 (2021).
1217
1218 59. Ciardo D*, et al.* Polo-like kinase 1 (Plk1) regulates DNA replication origin firing and
1219 interacts with Rif1 in Xenopus. *Nucleic Acids Res* **49**, 9851-9869 (2021).
1220
1221 60. Bohly N*, et al.* Increased replication origin firing links replication stress to whole
1222 chromosomal instability in human cancer. *Cell Rep* **41**, 111836 (2022).
1223
1224 61. Toledo LI*, et al.* ATR prohibits replication catastrophe by preventing global exhaustion
1225 of RPA. *Cell* **155**, 1088-1103 (2013).
1226

1227 62. Helmrich A, Ballarino M, Nudler E, Tora L. Transcription-replication encounters,
1228 consequences and genomic instability. *Nat Struct Mol Biol* **20**, 412-418 (2013).
1229
1230 63. Rhind N, Gilbert DM. DNA replication timing. *Cold Spring Harb Perspect Biol* **5**,
1231 a010132 (2013).
1232
1233 64. Boos D, Ferreira P. Origin Firing Regulations to Control Genome Replication Timing.
1234 *Genes (Basel)* **10**, (2019).
1235
1236 65. Burrell RA*, et al.* Replication stress links structural and numerical cancer chromosomal
1237 instability. *Nature* **494**, 492-496 (2013).
1238
1239 66. Volpi I, Gillespie PJ, Chadha GS, Blow JJ. The role of DDK and Treslin-MTBP in
1240 coordinating replication licensing and pre-initiation complex formation. *Open Biol* **11**,
1241 210121 (2021).
1242
1243 67. Gaggioli V, Zeiser E, Rivers D, Bradshaw CR, Ahringer J, Zegerman P. CDK
1244 phosphorylation of SLD-2 is required for replication initiation and germline
1245 development in C. elegans. *J Cell Biol* **204**, 507-522 (2014).
1246
1247 68. Fukuura M, Nagao K, Obuse C, Takahashi TS, Nakagawa T, Masukata H. CDK promotes
1248 interactions of Sld3 and Drc1 with Cut5 for initiation of DNA replication in fission yeast.
1249 *Mol Biol Cell* **22**, 2620-2633 (2011).
1250
1251 69. Muramatsu S, Hirai K, Tak YS, Kamimura Y, Araki H. CDK-dependent complex
1252 formation between replication proteins Dpb11, Sld2, Pol (epsilon}, and GINS in
1253 budding yeast. *Genes Dev* **24**, 602-612 (2010).
1254
1255 70. Rappas M, Oliver AW, Pearl LH. Structure and function of the Rad9-binding region of
1256 the DNA-damage checkpoint adaptor TopBP1. *Nucleic Acids Res*, (2010).
1257
1258 71. Ferreira P, Sanchez-Pulido L, Marko A, Ponting CP, Boos D. Refining the domain
1259 architecture model of the replication origin firing factor Treslin/TICRR. *Life Sci Alliance*
1260 **5**, (2022).
1261
1262 72. Chou DM, Petersen P, Walter JC, Walter G. Protein phosphatase 2A regulates binding
1263 of Cdc45 to the prereplication complex. *J Biol Chem* **277**, 40520-40527 (2002).
1264
1265 73. Kohler K*, et al.* The Cdk8/19-cyclin C transcription regulator functions in genome
1266 replication through metazoan Sld7. *PLoS Biol* **17**, e2006767 (2019).
1267
1268 74. Zimmerman KM, Jones RM, Petermann E, Jeggo PA. Diminished origin-licensing
1269 capacity specifically sensitizes tumor cells to replication stress. *Mol Cancer Res* **11**,
1270 370-380 (2013).
1271

75. Rainey MD, Quachthithu H, Gaboriau D, Santocanale C. DNA Replication Dynamics and Cellular Responses to ATP Competitive CDC7 Kinase Inhibitors. *ACS Chem Biol* **12**, 1893-1902 (2017).

76. Gillespie PJ, Gambus A, Blow JJ. Preparation and use of Xenopus egg extracts to study DNA replication and chromatin associated proteins. *Methods* **57**, 203-213 (2012).

77. Tyanova S*, et al.* The Perseus computational platform for comprehensive analysis of (prote)omics data. *Nat Methods* **13**, 731-740 (2016).

78. Rappsilber J, Mann M, Ishihama Y. Protocol for micro-purification, enrichment, pre-fractionation and storage of peptides for proteomics using StageTips. *Nat Protoc* **2**, 1896-1906 (2007).

79. Olsen JV*, et al.* Parts per million mass accuracy on an Orbitrap mass spectrometer via lock mass injection into a C-trap. *Mol Cell Proteomics* **4**, 2010-2021 (2005).

80. Cox J, Neuhauser N, Michalski A, Scheltema RA, Olsen JV, Mann M. Andromeda: a peptide search engine integrated into the MaxQuant environment. *J Proteome Res* **10**, 1794-1805 (2011).

81. Cox J, Mann M. MaxQuant enables high peptide identification rates, individualized p.p.b.-range mass accuracies and proteome-wide protein quantification. *Nat Biotechnol* **26**, 1367-1372 (2008).

82. Cox J, Hein MY, Luber CA, Paron I, Nagaraj N, Mann M. Accurate proteome-wide label-free quantification by delayed normalization and maximal peptide ratio extraction, termed MaxLFQ. *Mol Cell Proteomics* **13**, 2513-2526 (2014).

83. Hughes CS, Moggridge S, Muller T, Sorensen PH, Morin GB, Krijgsveld J. Single-pot, solid-phase-enhanced sample preparation for proteomics experiments. *Nat Protoc* **14**, 68-85 (2019).

84. Lu L*, et al.* Identification of MS-Cleavable and Noncleavable Chemically Cross-Linked Peptides with MetaMorpheus. *J Proteome Res* **17**, 2370-2376 (2018).

85. Chen ZL*, et al.* A high-speed search engine pLink 2 with systematic evaluation for proteome-scale identification of cross-linked peptides. *Nat Commun* **10**, 3404 (2019).

86. Riffle M, Jaschob D, Zelter A, Davis TN. ProXL (Protein Cross-Linking Database): A Platform for Analysis, Visualization, and Sharing of Protein Cross-Linking Mass Spectrometry Data. *J Proteome Res* **15**, 2863-2870 (2016).

87. Evans R*, et al.* Protein complex prediction with AlphaFold-Multimer. *bioRxiv*, 2021.2010.2004.463034 (2022).

88. Jumper J*, et al.* Highly accurate protein structure prediction with AlphaFold. *Nature* **596**, 583-589 (2021).

89. Kozakov D*, et al.* The ClusPro web server for protein-protein docking. *Nat Protoc* **12**, 255-278 (2017).

90. Zhou P, Jin B, Li H, Huang SY. HPEPDOCK: a web server for blind peptide-protein docking based on a hierarchical algorithm. *Nucleic Acids Res* **46**, W443-W450 (2018).

91. Yu C*, et al.* A mechanism for preventing asymmetric histone segregation onto replicating DNA strands. *Science* **361**, 1386-1389 (2018).

92. Xu X, Yan C, Zou X. MDockPeP: An ab-initio protein-peptide docking server. *J Comput Chem* **39**, 2409-2413 (2018).

93. Yan C, Xu X, Zou X. Fully Blind Docking at the Atomic Level for Protein-Peptide Complex Structure Prediction. *Structure* **24**, 1842-1853 (2016).

94. Raveh B, London N, Schueler-Furman O. Sub-angstrom modeling of complexes between flexible peptides and globular proteins. *Proteins* **78**, 2029-2040 (2010).

95. Xue LC, Rodrigues JP, Kastritis PL, Bonvin AM, Vangone A. PRODIGY: a web server for predicting the binding affinity of protein-protein complexes. *Bioinformatics* **32**, 3676-3678 (2016).

96. Romero-Molina S*, et al.* PPI-Affinity: A Web Tool for the Prediction and Optimization of Protein-Peptide and Protein-Protein Binding Affinity. *J Proteome Res* **21**, 1829-1841 (2022).

97. Zheng SQ, Palovcak E, Armache JP, Verba KA, Cheng Y, Agard DA. MotionCor2: anisotropic correction of beam-induced motion for improved cryo-electron microscopy. *Nat Methods* **14**, 331-332 (2017).

98. Bepler T*, et al.* Positive-unlabeled convolutional neural networks for particle picking in cryo-electron micrographs. *Nat Methods* **16**, 1153-1160 (2019).

99. Liebschner D*, et al.* Macromolecular structure determination using X-rays, neutrons and electrons: recent developments in Phenix. *Acta Crystallogr D Struct Biol* **75**, 861-877 (2019).

100. Vizcaino JA*, et al.* 2016 update of the PRIDE database and its related tools. *Nucleic Acids Res* **44**, D447-456 (2016).

1363 # Figure Legends
1364
1365 **Figure 1: GINS and TopBP1 interact.**
1366
1367 a: (i) Domain model of human (hs) TopBP1, its conservation with BRCT1/2 and 3/4 domains
1368 (grey boxes) of budding yeast Dpb11 (scDpb11). Arrows indicate binding domains of
1369 interacting proteins. (ii) Domain model overview of TopBP1 wild type (WT) and BRCT
1370 deletion (Δ) and point mutants. GINS binding capabilities are denoted in red and green.
1371 Numbers, amino acid position; capital letters indicate amino acid substitutions. Amino acid
1372 substitutions of point mutants in BRCT4 (B4mut) and 5 (B5mut) are coloured orange.
1373
1374 b: Elution profiles of size exclusion chromatography (Superdex200) of individual recombinant
1375 TopBP1-BRCT0-5 protein (grey) and GINS tetramers (green), or of both upon incubation
1376 (blue).
1377
1378 c: Recombinant GINS immobilised on Flag-beads and control beads (Flag beads coupled with
1379 Flag peptide) were used to pull down recombinant TopBP1-0-5-WT or TopBP1-ΔBRCT4/5
1380 (compare panel a(ii)). SDS gels were silver stained. (kDa) specifies molecular weight marker
1381 bands.
1382
1383
1384 **Figure 2: Protein structure of the GINS-TopBP1-BRCT4/5 complex.**
1385 a: Structural model of the GINS-TopBP1-BRCT4/5 complex. Crystal structures of the GINS
1386 subunits (shades of green, yellow), and the central BRCT4/5 domain of TopBP1 (grey) were
1387 docked into the cryo-EM volume.
1388
1389 b: Zoom-in of the BRCT4-Psf1 interface. The residues in stick representation appear crucial
1390 for the interface. Mutations to break the interaction are coloured pink (Psf1-I97R; see Fig.
1391 1a(ii)) and purple (TopBP1-B4mut; see Fig. 1a(ii)).
1392
1393 c: Pulldown of the indicated recombinant TopBP1-BRCT0-5-strep versions (see Fig. 1a(ii)) by
1394 Flag-beads-immobilised recombinant GINS or control beads (Flag peptide-coupled). Analysis
1395 was done by immunoblotting.
1396
1397 d: Pulldown of the indicated recombinant TopBP1-BRCT0-5-WT-strep using immobilised
1398 GINS-WT or GINS carrying a Ile97 to arginine mutation in Psf1.TopBP1-Gcc/B4mut-strep
1399 (Fig. 1a(ii)) was used as a non-GINS binding control.
1400
1401
1402 **Figure 3: The conserved core of the TopBP1-GINI domain is required for a stable**
1403 **interaction with GINS**
1404

1405 a: Domain model and T-COFFEE alignment (in one-letter aa code) of TopBP1 proteins from
1406 humans (Q92547) *Xenopus laevis* (Q7ZZY3), *Bos taurus* (A0A3Q1LWE4) and *Rattus*
1407 *norvegicus* (A0A8I6GFZ6). Coloured boxes indicate GINI region mutants in sub-regions I
1408 (blue), II (green) and III (orange), and in the GINI core helix (red) (details in supplementary
1409 Fig S7). Amino acid substitutions and names of GINI core region mutations are shown (ii). In
1410 the alignment, '.', ':' and '*' indicate low conservation, high conservation and identical amino
1411 acids, respectively.
1412
1413 b/c: Pulldown of recombinant TopBP1-BRCT0-5-strep-WT or the indicated GINI region
1414 mutants (panel a) by bead-immobilised GINS or Flag peptide-coupled control beads. Analysis
1415 was done by immunoblotting.
1416
1417 d: Fluorescence polarisation measurements using recombinant GINS tetramer and
1418 fluorescently labelled TopBP1-GINI-core peptides (WT or Gpp (panel a)).
1419
1420
1421 **Figure 4:**
1422
1423 a: Structural model of TopBP1-BRCT3-5 complexed to the GINS tetramer predicted using
1424 AlphaFold2-Multimer. Of TopBP1, only the GINS binding surfaces, GINI helix (residues 485-
1425 496) and BRCT4/5 (residues 551-766), are shown.
1426
1427 b: Cryo-EM volume showing extra helical density ascribed to the GINI helix (left). On the right
1428 a structural model based on this cryo-EM and an AlphaFold2-Multimer predicted structure.
1429
1430 c: Pulldown of recombinant TopBP1-BRCT0-5-WT-strep using immobilised GINS-WT or
1431 GINS carrying the indicated Psf1 mutations. TopBP1-BRCT0-5-Gcc/B4mut-strep served as a
1432 non-GINS binding control. Analysis was done by immunoblotting.
1433
1434
1435 **Figure 5: Both GINS binding surfaces in TopBP1 cooperate in supporting DNA**
1436 **replication.**
1437
1438 a: Immobilized recombinant GINS was used to pulldown of indicated recombinant TopBP1-
1439 strep versions using 100 mM NaAc in the binding buffer. The pulldown was analysed by
1440 immunoblotting.
1441
1442 b: (i) shows the AlphaFold2-Multimer model of the GINS-TopBP1 complex that was used to
1443 estimate the binding free energy using PPI-Affinity and PRODIGY (ii). Estimations were done
1444 for the binding interfaces involving TopBP1-GINI (blue) and TopBP1-BRCT4 (red), both
1445 together and alone.
1446
1447 c: Coomassie-stained SDS PAGE gel of the indicated recombinant TopBP1-BRCT0-5 proteins
1448 (see Fig. 1a(ii) and 3a for nomenclature).

1449
1450 d: The indicated relative amounts (100 % - 10 %) of immunodepleted and non-depleted
1451 *Xenopus* egg extracts (Xtract) were analysed by immunoblotting using anti-TopBP1 #2 and the
1452 indicated antibodies. TopBP1 antibodies #1 and #2, or unspecific IgG (mock) were used for
1453 immunodepletions. Ponc, ponceau staining. Error bars, SEM, n=3
1454
1455 e/f: Replication analysis of *Xenopus* egg extracts immunodepleted with antibodies anti-
1456 TopBP1#1, #2 or unspecific IgG (mock). Buffer (buf), recombinant wild-type (WT) or mutant
1457 TopBP1-BRCT0-5-strep (panel B) were added. Error bars, SEM, n=3
1458
1459
1460 **Figure 6: GINS binding to TopBP1 is required for the origin firing step of replication.**
1461 a-c: Label-free quantification of chromatin-bound proteins (four biological replicates; 75 min
1462 after sperm chromatin addition) by mass spectrometry upon chromatin isolation from
1463 aphidicolin-treated interphase *Xenopus* egg extracts upon replacing endogenous TopBP1 with
1464 indicated TopBP1 mutants using immunodepletion as described in Fig. 5. (a) semi-quantitative
1465 heat map, (b) schematic model of DNA replication, (c) volcano plots highlighting a selection
1466 of differentially detected proteins (detailed volcanos in supplementary Fig. S14). Heatmaps (a)
1467 show hierarchical clustering performed on z-score normalized log2 transformed label-free
1468 intensity values. Label-free intensities prior z-score normalization are provided in
1469 supplementary Table 2.
1470
1471 d: Experiment as in a) was analysed by chromatin isolation and immunoblotting with the
1472 indicated antibodies. Coomassie staining of the gel part containing histones served as a loading
1473 control.
1474
1475
1476 **Figure 7: Exclusive binding of TopBP1 and DNA polymerase epsilon to GINS in the CMG**
1477 **context.**
1478
1479 a/b: Structure of human CMG (PBD 7PFO), in panel a with our GINS-TopBP1 superposed in
1480 panel b with DNA Polε (CMGE; PBD 7PFO) both shown from the same angle, demonstrating
1481 accessibility of the TopBP1 binding sites in CMG, and strong overlap between BRCT4 and
1482 PolE2 occupied spaces .
1483
1484 c: In-detail views of GINS-TopBP1 and GINS-PolE2 (PBD 7PFO) interaction sites.
1485

1486 ## Supplementary figure legends
1487
1488
1489 **Figure S1: Schematic model of the origin firing reaction in yeast**
1490 Details are described in the main text.
1491
1492 **Figure S2: Interaction of GINS and TopBP1 in cell lysates.**
1493 a: Volcano plots showing label-free mass spectrometry quantification (four biological
1494 replicates) of proteins biotinylated by TopBP1 fused to APEX2. The top plot shows the results
1495 for stable isogenic Hek293-FlipIn cells while the middle and lower plots are based on results
1496 from transiently transfected Hek293T cells. Non-APEX2-biotinylated samples (-H_2O_2) were
1497 used as controls. Four biological replicates were analysed per experiment. Red dots and text
1498 indicate significantly enriched known TopBP1 interactors. Black dots and text indicate non-
1499 significantly enriched TopBP1 interactors.
1500
1501 b: Immunoblots showing immunoprecipitation of 6Myc-TEV2-TopBP1-BRCT0-5 from
1502 transiently transfected 293T cell lysates using anti-Myc antibodies. Non-transfected cell lysates
1503 were used for control IPs. Immunoprecipitated TopBP1 was detected using Ponceau (Ponc.)
1504 staining. A weak but specific co-IP of Sld5 was detectable.
1505
1506 c: Myc-immunoprecipitation as in B, except that 6Myc-TEV2-TopBP1-BRCT0-5-WT was
1507 compared with 6Myc-TEV2-TopBP1-ΔBRCT4/5. The specific co-IP of Sld5 with TopBP1
1508 found in b could be confirmed. TopBP1-ΔBRCT4/5 bound GINS less efficiently compared to
1509 WT.
1510
1511
1512 **Figure S3: Characterisation of the GINS-TopBP1 interaction.**
1513 a: Coomassie-stained SDS gel of fractions from the size exclusion chromatography experiment
1514 testing complexation of TopBP1-BRCT0-5-strep and GINS tetramer shown in Fig. 1b. Where
1515 both GINS and TopBP1 were mixed there is a shift of the individual components to the earlier
1516 fractions indicating a stable complex was formed.
1517
1518 b: Recombinant TopBP1-ΔBRCT0-2 was incubated with recombinant GINS before size
1519 exclusion chromatography using a Superdex200 increase 10/300 column. The individual
1520 recombinant proteins were run separately for comparison. Elution profiles are shown with
1521 GINS coloured green, TopBP1 grey and the complex is coloured cyan. The clear shift upon
1522 complex formation suggests the N-terminal BRCT0-2 module of TopBP1 is dispensable for
1523 the interaction.
1524
1525 c: Recombinant GINS immobilised on Flag-beads and control beads (Flag beads coupled with
1526 Flag peptide) were used to pull down recombinant TopBP1-0-5-WT (same as in Fig1c) or the
1527 deletion mutant ΔBRCT3 (Fig 1a(ii)). SDS gels were silver stained.
1528

1529 d: The TopBP1 triple point mutant inactivating the phospho-binding pocket of BRCT5 (B5mut)
1530 that carries the mutations S654V, K661R and K704A (Fig. 1a(ii)) binds 53BP1 weakly in
1531 pulldowns from HEK293T cell lysates.
1532
1533 e: *In vitro* pulldown of TopBP1-WT and TopBP1-BRCT0-5-B5mut (Fig. 1a(ii)) with
1534 immobilised GINS (or Flag peptide for controls). The phospho-binding pocket of BRCT5 is
1535 inactive in B5mut (panel c). The B5mut mutant binds to GINS as well as TopBP1-BRCT0-5-
1536 WT, suggesting that the phospho-binding pocket of BRCT5 is dispensable for GINS binding.
1537
1538
1539 **Figure S4: Cryo electron microscopy analysis of GINS-TopBP1-BRCT4.**
1540
1541 EM processing diagram for the initial dataset including representative micrograph and final
1542 FSC curves.
1543
1544
1545 **Figure S5: TopBP1-BRCT4 diverts from the canonical BRCT fold**
1546 a) Superposition of BRCA1-BRCT1 (canonical BRCT; blue) and BRCT4 of TopBP1 (black).
1547 The canonical helix between beta strands three and four is missing in TopBP1-BRCT4.
1548
1549 b) This structural model of BRCT4 binding to Psf1 indicates that the missing helix in BRCT4
1550 helps create space for the interaction to take place. V590 and T606 are residues important for
1551 the interaction that were mutated in TopBP1-B4mut.
1552
1553 c) Multiple sequence alignment of the diverting region in BRCT4 in a wide range of metazoa
1554 shows that the binding region for Psf1 constitutes a highly conserved patch. Residues mutated
1555 in TopBP1-B4mut show high similarity.
1556
1557
1558 **Figure S6: Experiments to control quality of recombinant proteins.**
1559
1560 a: Recombinant TopBP1 point mutants of the GINI and BRCT4 regions bind 53BP1 phospho-
1561 dependently. TopBP1-BRCT0-5-strep-WT and indicated mutants (Figs. 1a and 3a summarize
1562 the TopBP1 mutants) were used to pull down endogenous 53BP1 from Hek293T cell lysates.
1563 Lysates and pulldowns were analysed by immunoblotting. 53BP1 has two binding domains in
1564 TopBP1, BRCT0-2 and BRCT4/5 that both interact phosphorylation-dependently, as PPase-
1565 treatments showed (last two lanes). TopBP1-BRCT0-5 contains both binding sites, explaining
1566 its stronger binding to 53BP1 compared to the TopBP1-BRCT-ΔBRCT4/5 [40].
1567
1568 b: Psf1 I97R and Psf1 N43A/K51A form GINS tetramers normally. 100 nM of GINS-WT or
1569 the mutants were immobilized to the magnetic αFlag beads through 6xHis-3xFlag-Sld5 and
1570 then washed. Tetramer formation was detected by SDS PAGE and coomassie staining. GINS
1571 subunits were present in similar amounts, indicating normal GINS tetramer formation.
1572

Figure S7: Alignment of TopBP1 proteins from different vertebrate species using T-COFFEE and relative position to the TopBP1 BRCT domains.
Xenopus, *Xenopus laevis* (Q7ZZY3), Cow, *Bos taurus* (A0A3Q1LWE4), Rat, *Rattus norvegicus* (A0A8I6GFZ6). Coloured labelling shows the amino acids mutated in the TopBP1 region I (RI), region II (RII), region III (RIII), and GINI core centre (Gcc) mutants.

Fig. S8: Probability plots for AlphaFold2-Multimer prediction of Fig. 4a.

Fig. S9: Molecular docking simulations of the GINI centre core peptide (487-DEDLLSQY-494) on the GINS tetramer using Cluspro (a), MDockPep (b) and HPEPDOCK (c). Docking refinement with FlexPepDock (d).

Figure S10: Crosslinking mass spectrometry to analyse the GINS-TopBP1 complex.
a: Schematic representation of BS^3-mediated cross-links between TopBP1-BRCT0-5-Strep and GINS (detailed description below). (i) shows crosslinks involving the GINI domain of TopBP1, (ii) shows circle plots of all inter-protein crosslinks detected. Recombinant TopBP1-BRCT0-5-strep (amino acids 1-766) and GINS were crosslinked with 600µM or 2500µM of BS^3 crosslinker and analysed by mass spectrometry. Crosslinked samples were either analysed directly (in solution, left) or after resolving cross links by SDS-PAGE and in-gel digestion (right). ProXL (Protein Cross-Linking Database) was used to analyse and visualize the data. Cross-links in (i) are coloured according to the number of peptide spectrum matches showing this link.

b: AlphaFold2 structure prediction of the TopBP1-Psf1-Psf3 complex with violet highlighted amino acids involved in crosslinking in panel a.

c: Structure of the GINS crystal structure superposed onto AlphaFold2 TopBP1-Psf1-Psf2 complex with Sld5 amino acids involved in crosslinking highlighted in violet.

GINI region crosslinks:
Most GINI region crosslinks were found with Psf1 lysines 63, and Psf3 Lys80 that cluster in the GINS structure. Fewer crosslinks were found with Psf1 Lys61 that is situated in the same region but facing the other direction. The distance between Lys482 in the GINI helix and Thr61 of Psf1 is 27,25 Å. Between TopBP1-Ser480 and Psf3-Lys74, it is 26,16 Å. The most extended distances with about 50 Å show crosslinks from TopBP1 lysines 466 and 468, which are furthest away from the GINI helix. This large distance is probably explained by the flexibility of this unstructured part. Crosslinking with Psf3 lysine 65 on the other face of this structural part of GINS supports this interpretation.

Crosslinks involving other regions of TopBP1 and GINS:

1616 The GINI region also crosslinks with Sld5 residues 112, 113, 142, 164 and 208. These residues
1617 are located sufficiently close for BS^3 crosslinks to be permissible with the predicted GINI
1618 interaction site on the surface of the GINS tetramer as seen in panel c.
1619 The GINI region appears the main GINS-crosslinking region in TopBP1. Further crosslinks
1620 were detected in the BRCT0-2 region of TopBP1, mainly with Sld5 and Psf1. These residues
1621 are situated in positions 102, 112, 113, 142, 164, 208 and 209 in Sld5, and 51, 61, 63, 154 and
1622 171 in Psf1.
1623 To our surprise, crosslinking between BRCT4 and GINS is not apparent. Only a single
1624 crosslink was detected between residue 576 of BRCT4 and 210 on Psf3. An explanation for
1625 this crosslink scarcity could be that the region of Psf1 that binds BRCT4 is crosslinked in a
1626 conformation that prevents BRCT4 binding. The presence of crosslinks between the C-terminal
1627 helix of Psf3 and the Psf1 B domain might suggest that crosslinking has locked the GINS
1628 complex into its CMG bound state where these two regions are brought into close proximity.
1629 It is possible this form of the GINS tetramer interferes with TopBP1 BRCT4-GINS complex
1630 formation.
1631
1632
1633 **Figure S11: EM processing diagram for the initial dataset including representative**
1634 **micrograph and final FSC curves.**
1635
1636
1637 **Figure S12: Characterisation of TopBP1 mutants**
1638 a: Pulldowns of the indicated TopBP1 mutants with bead-immobilised GINS at reduced ionic
1639 strength of 100 mM sodium acetate compared to previous pulldown experiments in 150 mM
1640 sodium chloride. Mutating the individual sites revealed a reduced but specific pulldown
1641 efficiency compared to TopBP1-WT. Double mutants did not show pulldown.
1642
1643 b: Immuno-depletion and add-back experiment as described in Figures 5e/f and 6. Western blot
1644 with the indicated antibodies upon re-isolating sperm chromatin from egg extract 120 minutes
1645 after starting the replication reaction. TopBP1-Gcc mutant shows slightly stronger signals than
1646 the double mutant for Cdc45, but clearly weaker than WT and Δ4/5.
1647
1648
1649 **Figure S13: Replication analyses**
1650 a: Replication analysis of experiment as described in Fig. 5e/f, but using anti-TopBP1 antibody
1651 number one. Two independent experiments are shown.
1652
1653 b: Replication analysis using *Xenopus* egg extracts upon replacing endogenous TopBP1 with
1654 indicated recombinant TopBP1 versions to test the consequences of the TopBP1-B4mut triple
1655 point mutations that were identified by our structural studies (Fig. 2b,c). TopBP1 antibody #2
1656 was used. TopBP1-B4mut and Δ4/5 behave similarly. The mutations in B4mut do not affect
1657 grossly the replication-inducing capacity compared to TopBP1-BRCT0-5-WT. However, the
1658 mutations in B4m aggravate the replication defect by the GINI site mutant Gcc. This

aggravation effect is consistent with the model that the residues in BRCT4 that are required for normal GINS binding are also required for the normal replication-inducing activity of TopBP1. The time points shown in this experiment are different from the others in this study, because the egg extract used here replicated quicker.

Figure S14: Volcano plots of mass spectrometry-based chromatin analysis

Data of experiment described in Figure 5a/b is shown. Here all differentially detected proteins are labelled.

Figure S15: The PolE2 N-terminus-binding Psf1-B domain is dispensable for TopBP1-BRCT4 interaction.

a/b: The Psf1-B domain is dispensable for binding TopBP1 in vitro. a) Pulldown experiments comparing the binding of bead-immobilised GINS-WT and mutant GINS containing Psf1 lacking the B domain to TopBP1-0-5-WT. Deletion of the B domain, which is the main binding site for PolE2, has moderate effects, if any, on TopBP1 association. b) Ten times molar excess of MBP-PolE2-N does not compete TopBP1-0-5-WT off of bead-immobilised GINS.

c: The Psf1-B domain is not visible in our cryo-EM data of the GINS tetramer and the GINS-TopBP1 complex. GINS alone map volume with docked crystal structure of GINS (PDB:2E9X) shown alongside the B domain of Psf1 taken from a superposed model of the full GINS complex from a cryo-EM reconstruction of the full CMG structure (PDB:6XTX) demonstrating no density for the B domain of Psf1 can be seen when the GINS complex is free suggesting a flexible conformation.

d: GINS-TopBP1 volume shown with TopBP1-GINS model from this paper, alongside the B-domain of Psf1 as for panel a, showing in our dataset no density for the B domain of Psf1 can be seen when GINS is bound to TopBP1. Taken together these two volumes suggest the B domain of Psf1 is flexible when not bound to the MCM ring and CDC45.

Figure S16: Models of TopBP1-mediated loading of GINS onto pre-RCs.

a: TopBP1 functions as a regulated scaffold of pre-LC. TopBP1's numerous interaction domains are key to assemble pre-LC. The CDK and DDK controlled interaction with Treslin couples CMG formation to S phase. Here we demonstrate and characterise the essential interaction with GINS. A second scaffold, DONSON, is an integral part of vertebrate pre-LC, whereas the yeast pre-LC component Sld2 is not part of vertebrate pre-LC. An interesting situation is present in pre-LCs of the metzoan *C. elegans* that possesses a yeast-like Sld2 in addition to DONSON

b: Hypothetical model of TopBP1's role in the CMG formation process. TopBP1 is recruited through a phosphorylation dependent interaction between the N-terminal BRCT0-2 module

and Treslin (i). This allows delivery of the GINS tetramer to the MCM-CDC45 complex (ii). The Psf1-B domain orders, packing against CDC45, simultaneously locking the MCM ring and weakening the interface between TopBP1 BRCT4 and GINS complex (iii). TopBP1 dissociates, exchanging with Polε to form the CMGE complex.

1709 ## Supplementary raw data file legends
1710
1711 (Data not included with the manuscript file)
1712
1713 **Figure S17: Models of TopBP1-mediated loading of GINS onto pre-RCs.**
1714 Uncropped gel images and blots
1715
1716 **Supplementary table 1**
1717 List of crosslinked GINI region peptides found by mass spectrometry (experiment
1718 supplementary Fig. S10).
1719
1720 **Supplementary table 2**
1721 List with statistical analysis of peptides found on chromatin by chromass (experiment Fig. 6a-
1722 c).
1723
1724 **Supplementary table 3**
1725 Raw data of replication analyses shown in Figures 5 and S13.

Figure 1

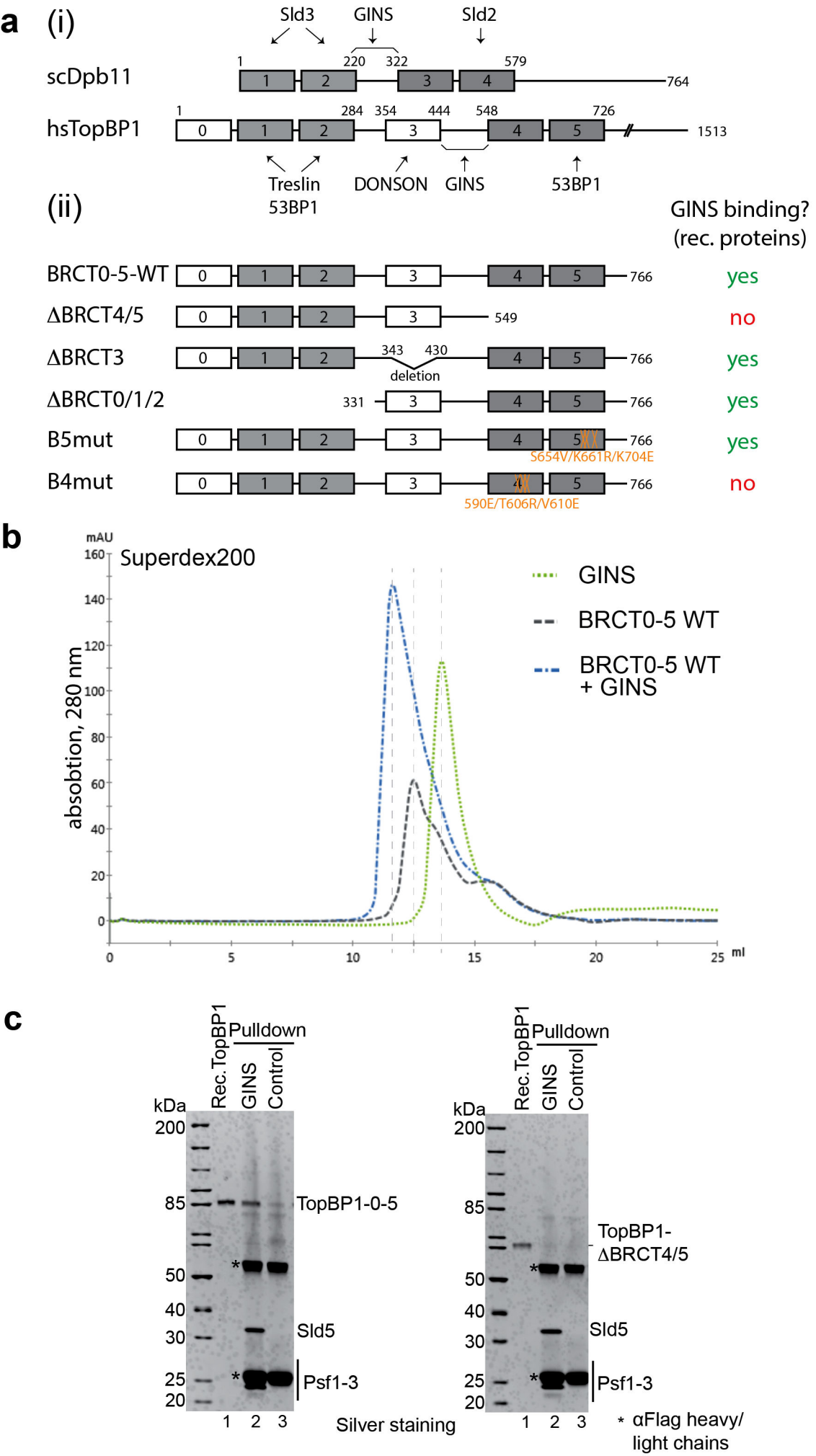
a
(i)
Sld3
GINS
Sld2
scDpb11
1
220
322
579
764
hsTopBP1
1
284
354
444
548
726
1513
Treslin
53BP1
DONSON
GINS
53BP1
(ii)
GINS binding?
(rec. proteins)
BRCT0-5-WT
766
yes
ΔBRCT4/5
549
no
ΔBRCT3
343
430
deletion
766
yes
ΔBRCT0/1/2
331
766
yes
B5mut
766
S654V/K661R/K704E
yes
B4mut
766
590E/T606R/V610E
no
b
mAU
Superdex200
absobtion, 280 nm
GINS
BRCT0-5 WT
BRCT0-5 WT
+ GINS
ml
c
Rec.TopBP1
Pulldown
GINS
Control
kDa
200
85
50
40
30
25
20
TopBP1-0-5
Sld5
Psf1-3
1 2 3
Silver staining
TopBP1-
ΔBRCT4/5
* αFlag heavy/
light chains

Figure 2

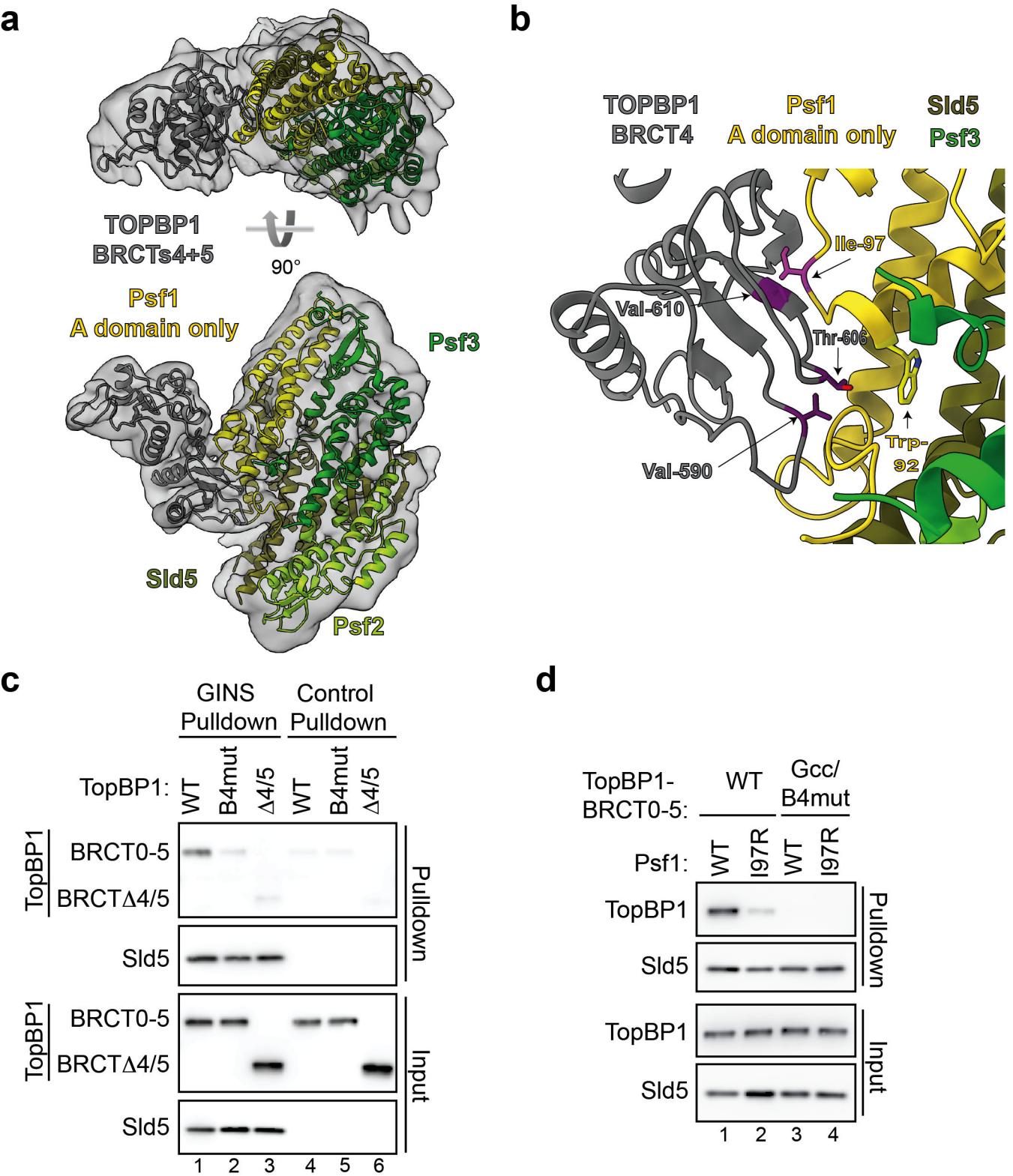
a
TOPBP1
BRCTs4+5
90°
Psf1
A domain only
Psf3
Sld5
Psf2
b
TOPBP1
BRCT4
Psf1
A domain only
Sld5
Psf3
Ile-97
Val-610
Thr-606
Trp-92
Val-590
c
GINS Pulldown
Control Pulldown
TopBP1:
WT
B4mut
Δ4/5
WT
B4mut
Δ4/5
TopBP1
BRCT0-5
BRCTΔ4/5
Sld5
Pulldown
Input
1 2 3 4 5 6
d
TopBP1-BRCT0-5:
WT
Gcc/B4mut
Psf1:
WT
I97R
WT
I97R
TopBP1
Sld5
Pulldown
Input
1 2 3 4

Figure 3

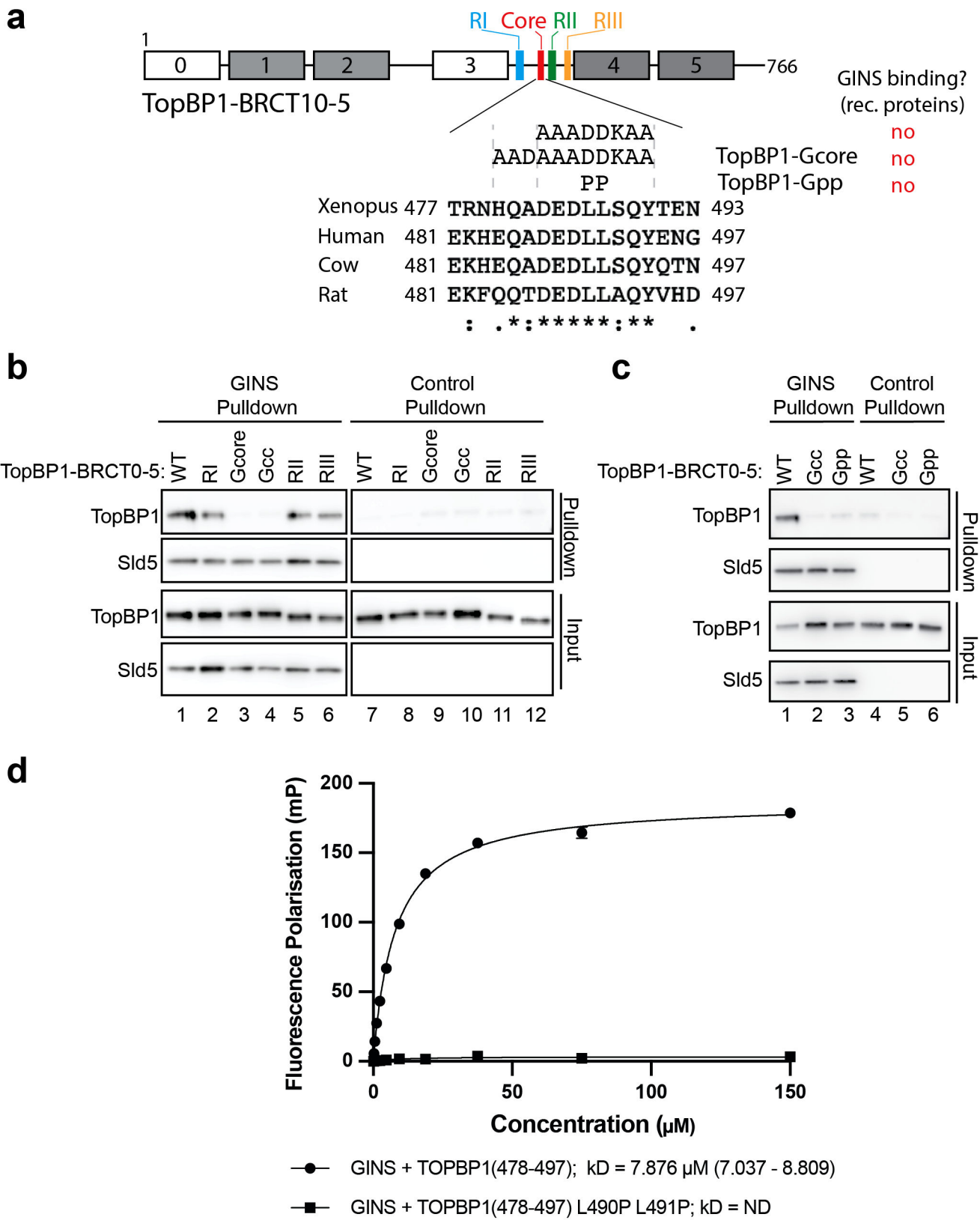
a
RI
Core
RII
RIII
1
0
1
2
3
4
5
766
TopBP1-BRCT10-5
GINS binding?
(rec. proteins)
AAADDKAA
AADAAADDKAA
PP
TopBP1-Gcore
TopBP1-Gpp
no
no
no
Xenopus 477 TRNHQADEDLLSQYTEN 493
Human 481 EKHEQADEDLLSQYENG 497
Cow 481 EKHEQADEDLLSQYQTN 497
Rat 481 EKFQQTDEDLLAQYVHD 497
: .*:*****:** .
b
GINS Pulldown
Control Pulldown
TopBP1-BRCT0-5:
WT
RI
Gcore
Gcc
RII
RIII
TopBP1
Sld5
Pulldown
Input
1 2 3 4 5 6 7 8 9 10 11 12
c
GINS Pulldown
Control Pulldown
TopBP1-BRCT0-5:
WT
Gcc
Gpp
TopBP1
Sld5
Pulldown
Input
1 2 3 4 5 6
d
Fluorescence Polarisation (mP)
200
150
100
50
0
0
50
100
150
Concentration (μM)
GINS + TOPBP1(478-497); kD = 7.876 μM (7.037 - 8.809)
GINS + TOPBP1(478-497) L490P L491P; kD = ND

Figure 4

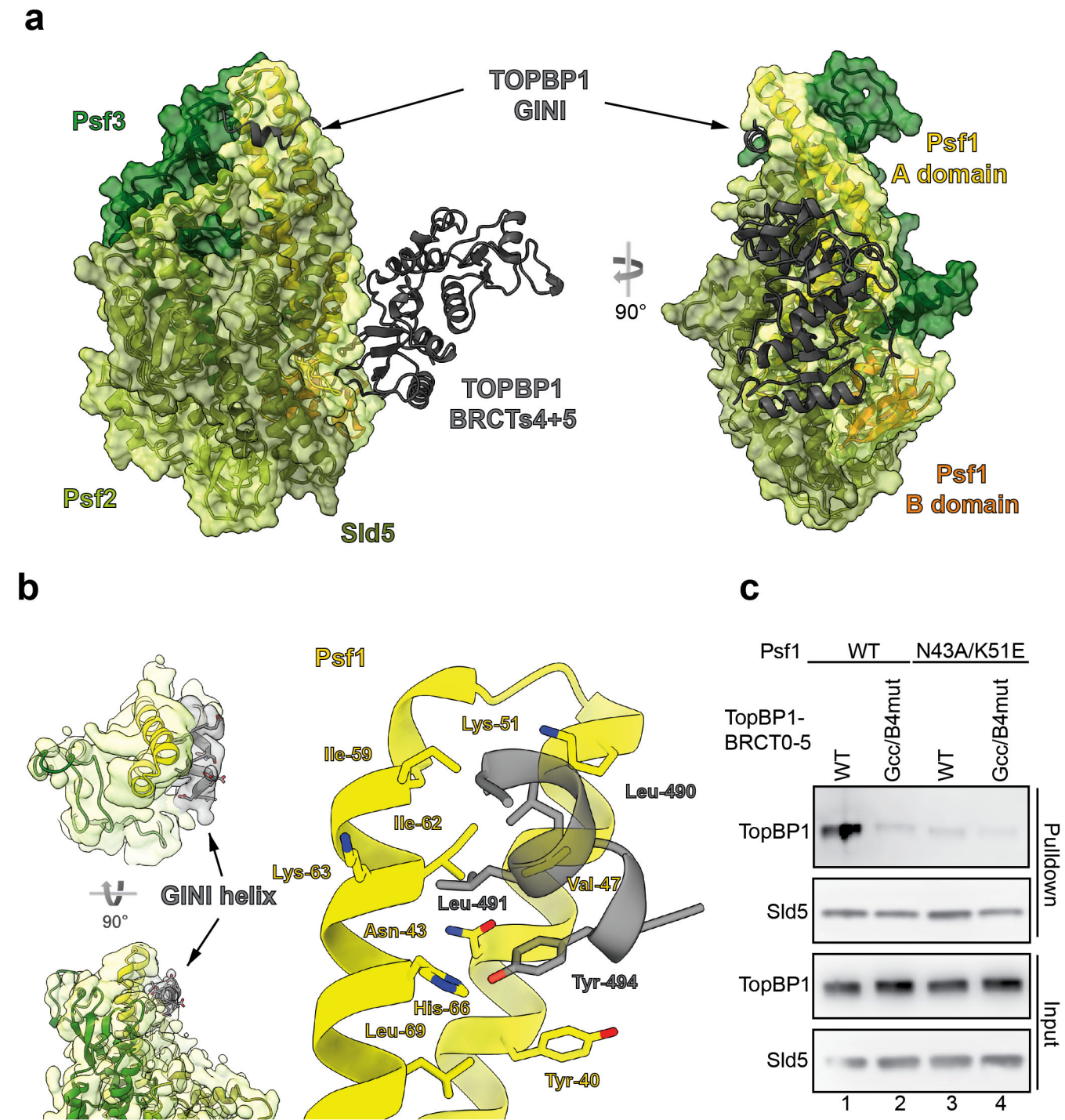
a
TOPBP1
GINI
Psf3
Psf1
A domain
90°
TOPBP1
BRCTs4+5
Psf2
Sld5
Psf1
B domain
b
Psf1
GINI helix
90°
Lys-51
Ile-59
Leu-490
Ile-62
Lys-63
Val-47
Leu-491
Asn-43
Tyr-494
His-66
Leu-69
Tyr-40
c
Psf1
WT
N43A/K51E
TopBP1-
BRCT0-5
WT
Gcc/B4mut
WT
Gcc/B4mut
TopBP1
Sld5
Pulldown
TopBP1
Sld5
Input
1
2
3
4

Figure 5

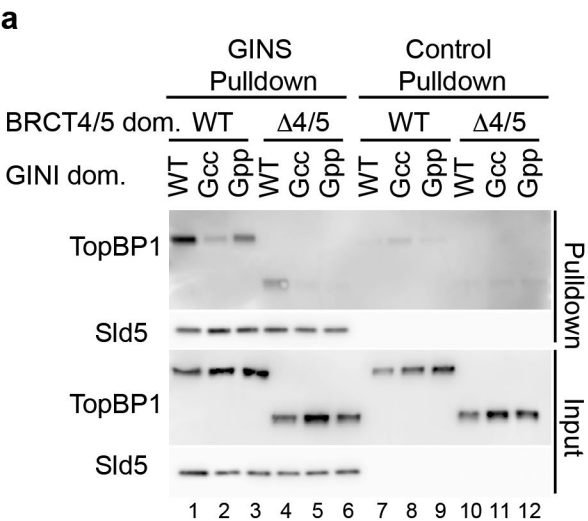

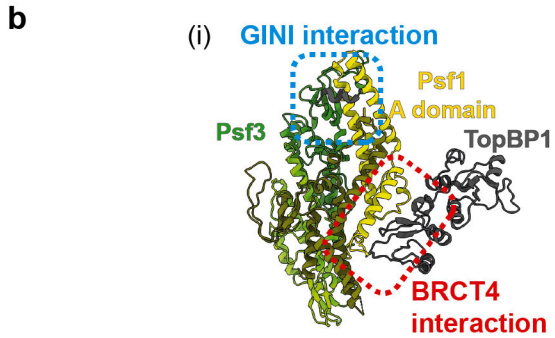

(ii)

interaction sites	Binding free energy [kcal/mol]	
	PPI-Affinity	PRODIGY
BRCT4 + GINI	-10.3	-15.0
BRCT4	-1.7	-8.4
GINI	-9.8	-10.9

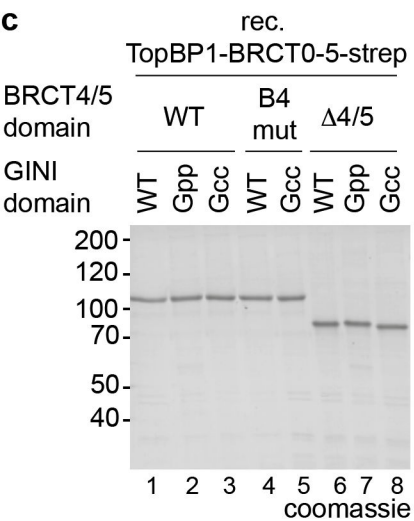

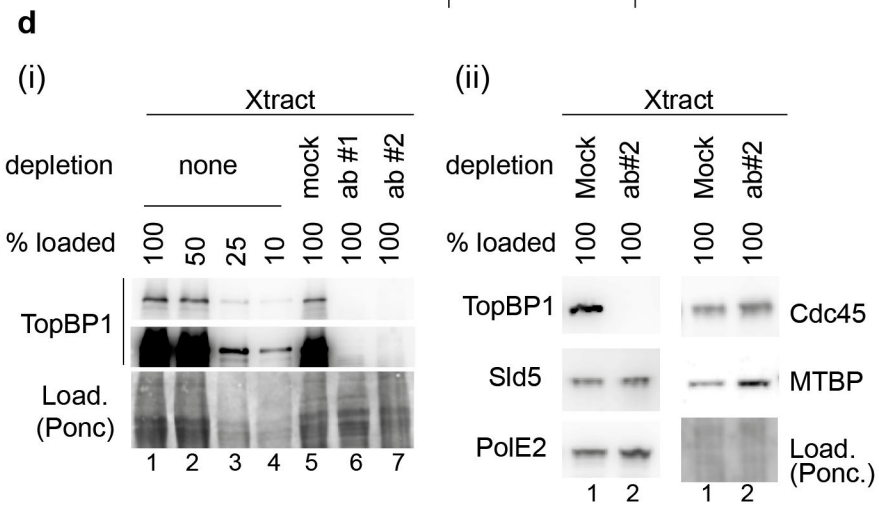

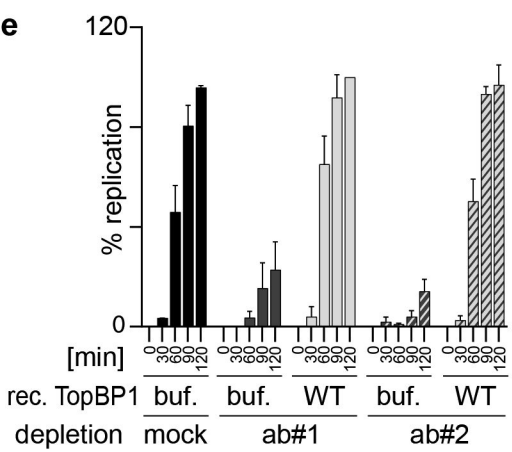

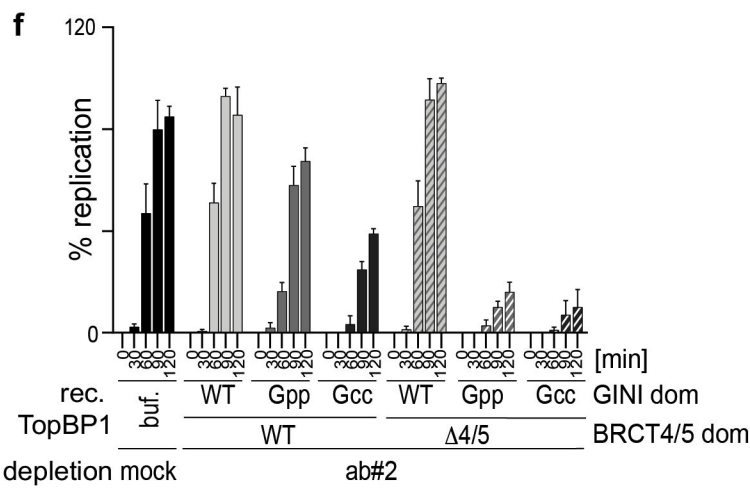

Figure 6

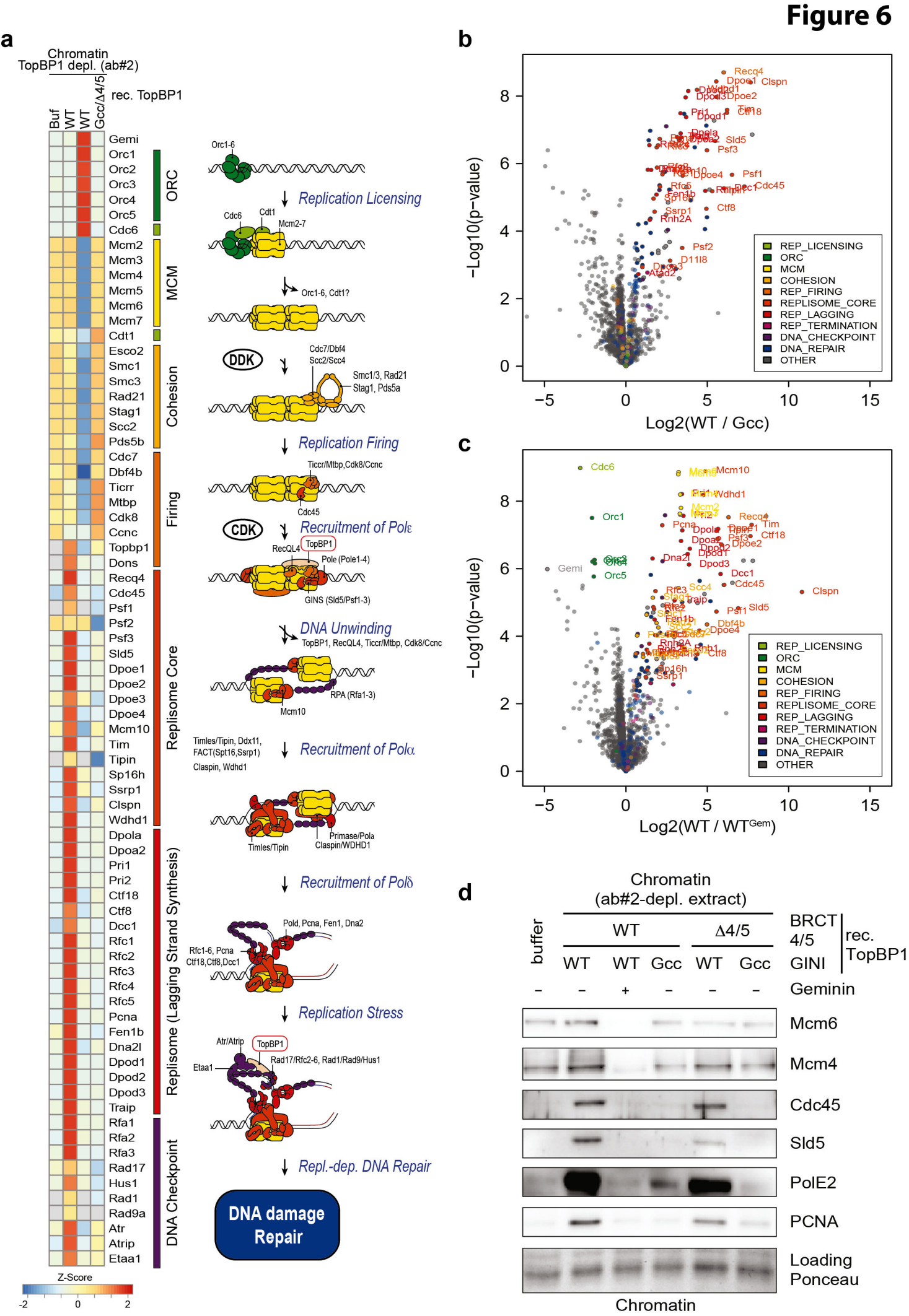
a
Chromatin
TopBP1 depl. (ab#2)
rec. TopBP1
Buf
WT
WT
Gcc/Δ4/5
Gemi
Orc1
Orc2
Orc3
Orc4
Orc5
Cdc6
Mcm2
Mcm3
Mcm4
Mcm5
Mcm6
Mcm7
Cdt1
Esco2
Smc1
Smc3
Rad21
Stag1
Scc2
Pds5b
Cdc7
Dbf4b
Ticrr
Mtbp
Cdk8
Ccnc
Topbp1
Dons
Recq4
Cdc45
Psf1
Psf2
Psf3
Sld5
Dpoe1
Dpoe2
Dpoe3
Dpoe4
Mcm10
Tim
Tipin
Sp16h
Ssrp1
Clspn
Wdhd1
Dpola
Dpoa2
Pri1
Pri2
Ctf18
Ctf8
Dcc1
Rfc1
Rfc2
Rfc3
Rfc4
Rfc5
Pcna
Fen1b
Dna2l
Dpod1
Dpod2
Dpod3
Traip
Rfa1
Rfa2
Rfa3
Rad17
Hus1
Rad1
Rad9a
Atr
Atrip
Etaa1
ORC
MCM
Cohesion
Firing
Replisome Core
Replisome (Lagging Strand Synthesis)
DNA Checkpoint
Z-Score
-2
0
2
Orc1-6
Replication Licensing
Cdc6
Cdt1
Mcm2-7
Orc1-6, Cdt1?
DDK
Cdc7/Dbf4
Scc2/Scc4
Smc1/3, Rad21
Stag1, Pds5a
Replication Firing
Ticcr/Mtbp,Cdk8/Ccnc
Cdc45
CDK
Recruitment of Polε
RecQL4
TopBP1
Pole (Pole1-4)
GINS (Sld5/Psf1-3)
DNA Unwinding
TopBP1, RecQL4, Ticcr/Mtbp, Cdk8/Ccnc
RPA (Rfa1-3)
Mcm10
Timles/Tipin, Ddx11,
FACT(Spt16,Ssrp1)
Claspin, Wdhd1
Recruitment of Polα
Timles/Tipin
Primase/Pola
Claspin/WDHD1
Recruitment of Polδ
Pold, Pcna, Fen1, Dna2
Rfc1-6, Pcna
Ctf18,Ctf8,Dcc1
Replication Stress
Atr/Atrip
TopBP1
Etaa1
Rad17/Rfc2-6, Rad1/Rad9/Hus1
Repl.-dep. DNA Repair
DNA damage
Repair
b
−Log10(p−value)
Log2(WT / Gcc)
REP_LICENSING
ORC
MCM
COHESION
REP_FIRING
REPLISOME_CORE
REP_LAGGING
REP_TERMINATION
DNA_CHECKPOINT
DNA_REPAIR
OTHER
c
−Log10(p−value)
Log2(WT / WTGem)
Gemi
d
Chromatin
(ab#2-depl. extract)
buffer
WT
Δ4/5
WT
WT
Gcc
WT
Gcc
BRCT
4/5
GINI
rec.
TopBP1
Geminin
Mcm6
Mcm4
Cdc45
Sld5
PolE2
PCNA
Loading
Ponceau
Chromatin

Figure 7

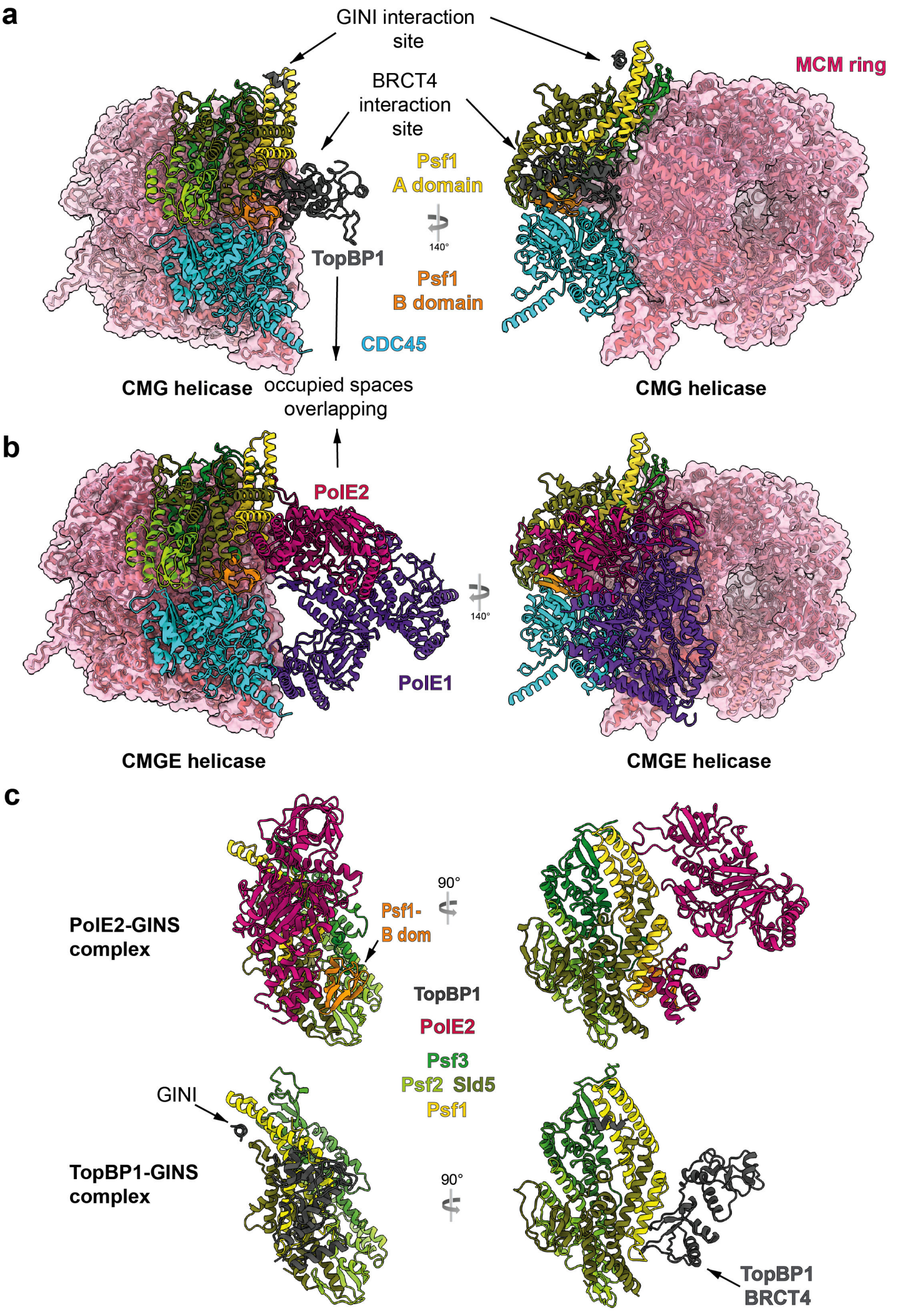
a
GINI interaction site
BRCT4 interaction site
MCM ring
Psf1 A domain
140°
TopBP1
Psf1 B domain
CDC45
CMG helicase
occupied spaces overlapping
CMG helicase
b
PolE2
140°
PolE1
CMGE helicase
CMGE helicase
c
PolE2-GINS complex
Psf1-B dom
90°
TopBP1
PolE2
Psf3
Psf2 Sld5
Psf1
GINI
TopBP1-GINS complex
90°
TopBP1 BRCT4

Figure S1

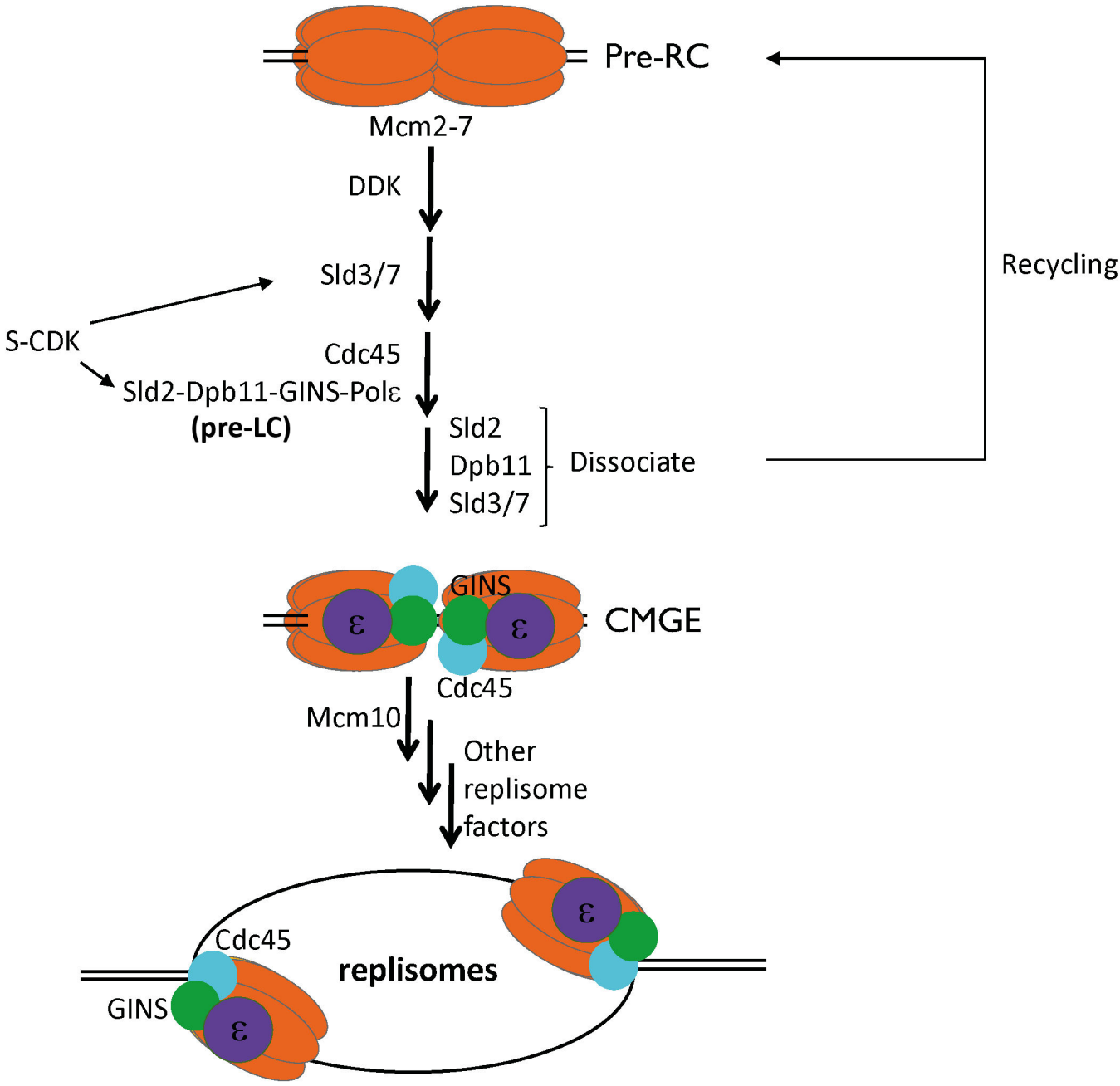
Pre-RC
Mcm2-7
DDK
Sld3/7
S-CDK
Cdc45
Sld2-Dpb11-GINS-Polε
(pre-LC)
Sld2
Dpb11
Sld3/7
Dissociate
Recycling
GINS
ε
ε
CMGE
Cdc45
Mcm10
Other
replisome
factors
Cdc45
GINS
ε
replisomes
ε

Figure S2

a

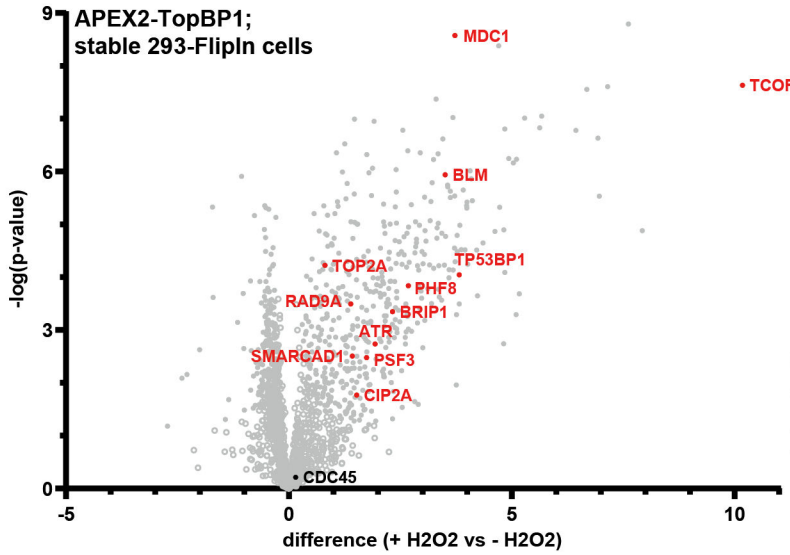

open grey circles: no significant difference
closed grey circles: significant difference
black: described TopBP1 interactor, not enriched
red: described TopBP1 interactor, significantly enriched

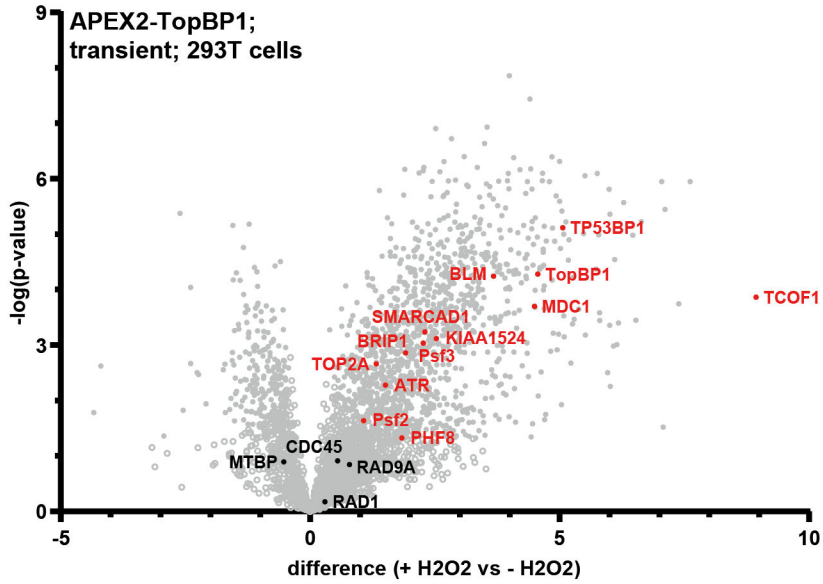

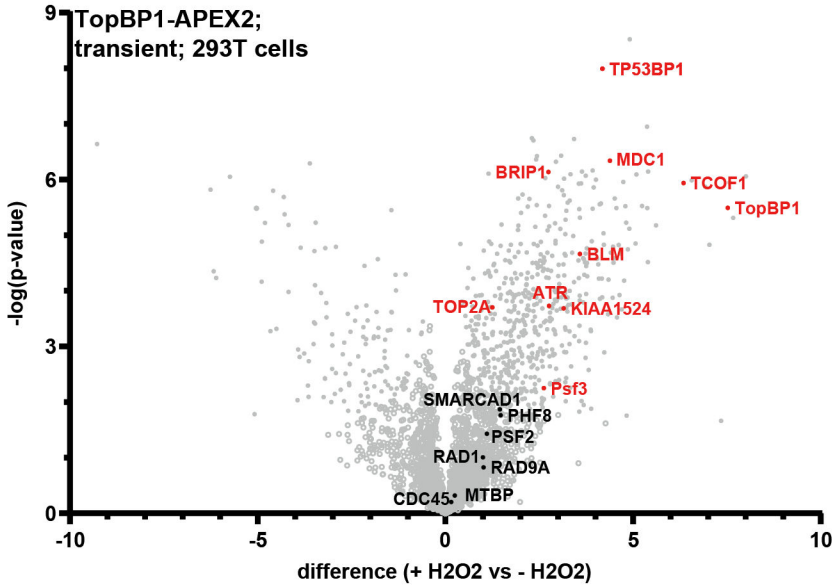

b

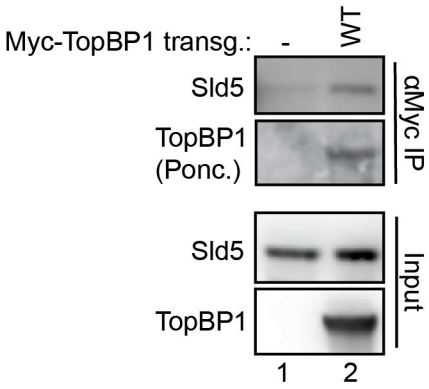

c

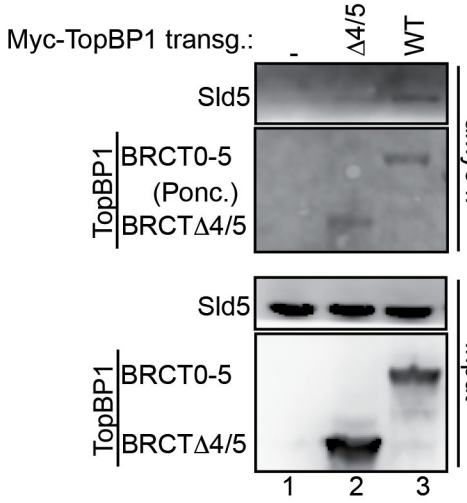

Figure S3

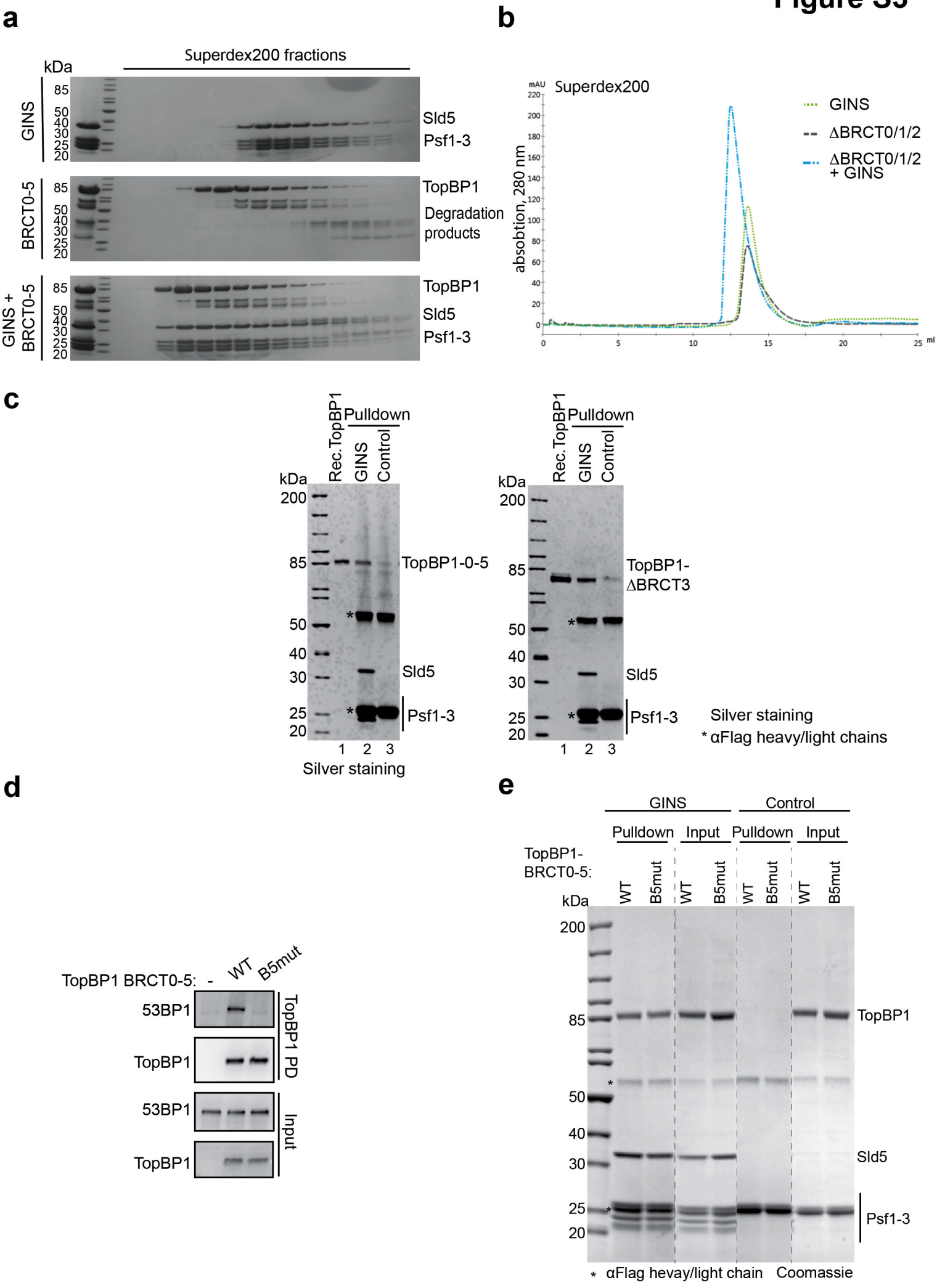
a
Superdex200 fractions
kDa
GINS
BRCT0-5
GINS + BRCT0-5
85
50
40
30
25
20
Sld5
Psf1-3
TopBP1
Degradation products
b
Superdex200
mAU
absobtion, 280 nm
GINS
ΔBRCT0/1/2
ΔBRCT0/1/2 + GINS
ml
c
Rec.TopBP1
Pulldown
GINS
Control
TopBP1-0-5
TopBP1-ΔBRCT3
Silver staining
* αFlag heavy/light chains
d
TopBP1 BRCT0-5:
WT
B5mut
53BP1
TopBP1
TopBP1 PD
Input
e
GINS
Control
Pulldown
Input
TopBP1-BRCT0-5:
* αFlag hevay/light chain
Coomassie

Figure S4

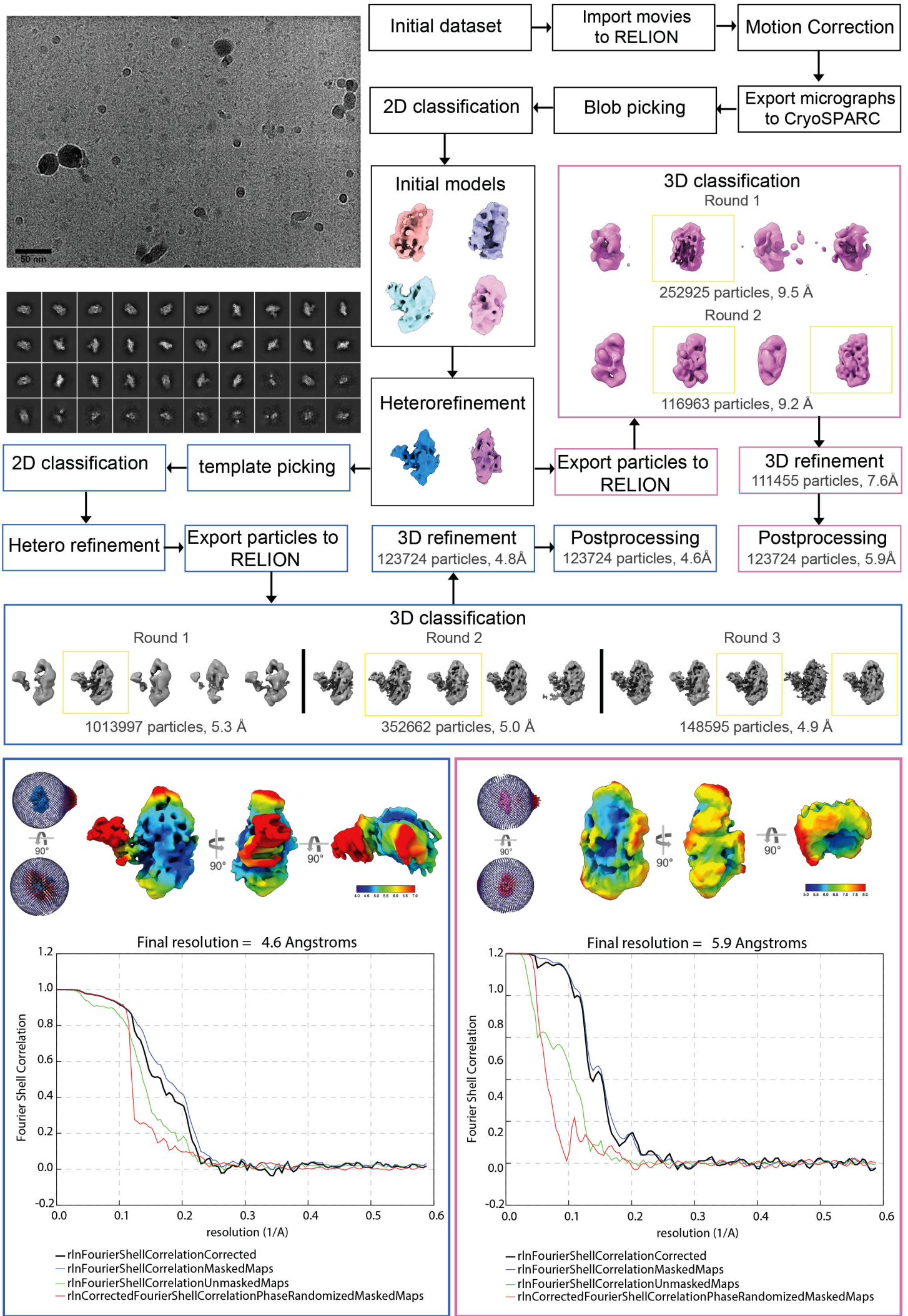
50 nm
Initial dataset
Import movies to RELION
Motion Correction
Export micrographs to CryoSPARC
Blob picking
2D classification
Initial models
Heterorefinement
template picking
2D classification
Hetero refinement
Export particles to RELION
3D refinement
123724 particles, 4.8Å
Postprocessing
123724 particles, 4.6Å
Export particles to RELION
3D refinement
111455 particles, 7.6Å
Postprocessing
123724 particles, 5.9Å
3D classification
Round 1
252925 particles, 9.5 Å
Round 2
116963 particles, 9.2 Å
3D classification
Round 1
Round 2
Round 3
1013997 particles, 5.3 Å
352662 particles, 5.0 Å
148595 particles, 4.9 Å
90°
Final resolution = 4.6 Angstroms
Final resolution = 5.9 Angstroms
Fourier Shell Correlation
resolution (1/A)
rlnFourierShellCorrelationCorrected
rlnFourierShellCorrelationMaskedMaps
rlnFourierShellCorrelationUnmaskedMaps
rlnCorrectedFourierShellCorrelationPhaseRandomizedMaskedMaps

Figure S5

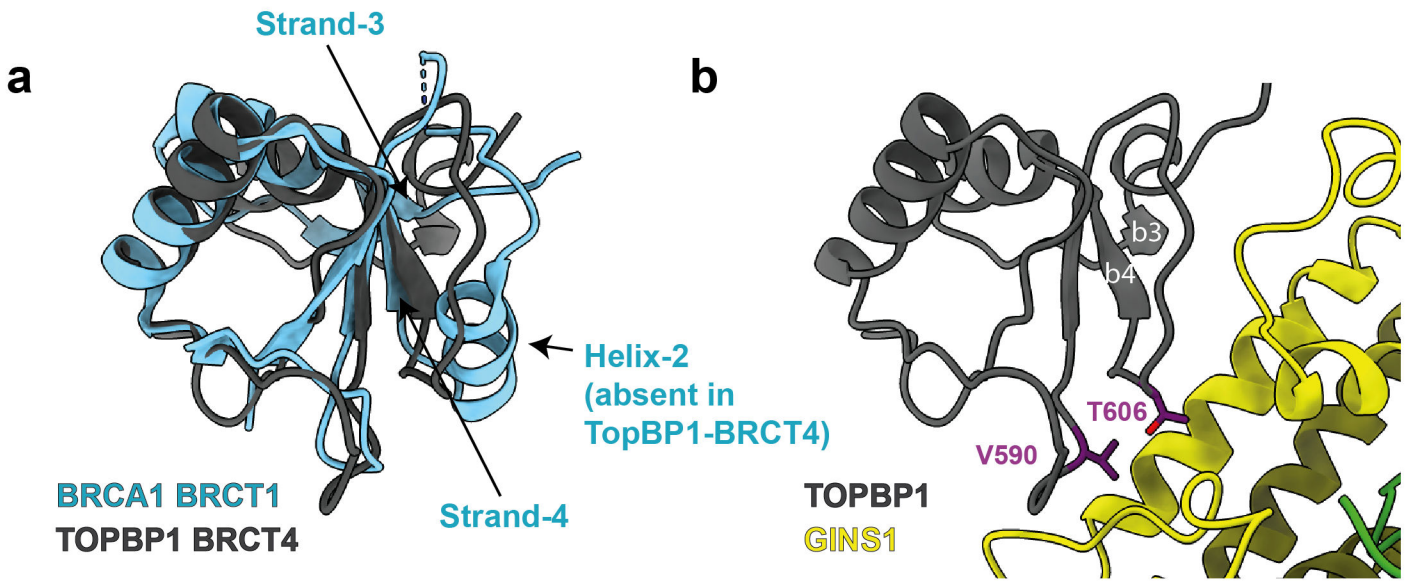
a
Strand-3
Helix-2
(absent in
TopBP1-BRCT4)
Strand-4
BRCA1 BRCT1
TOPBP1 BRCT4
b
b3
b4
T606
V590
TOPBP1
GINS1

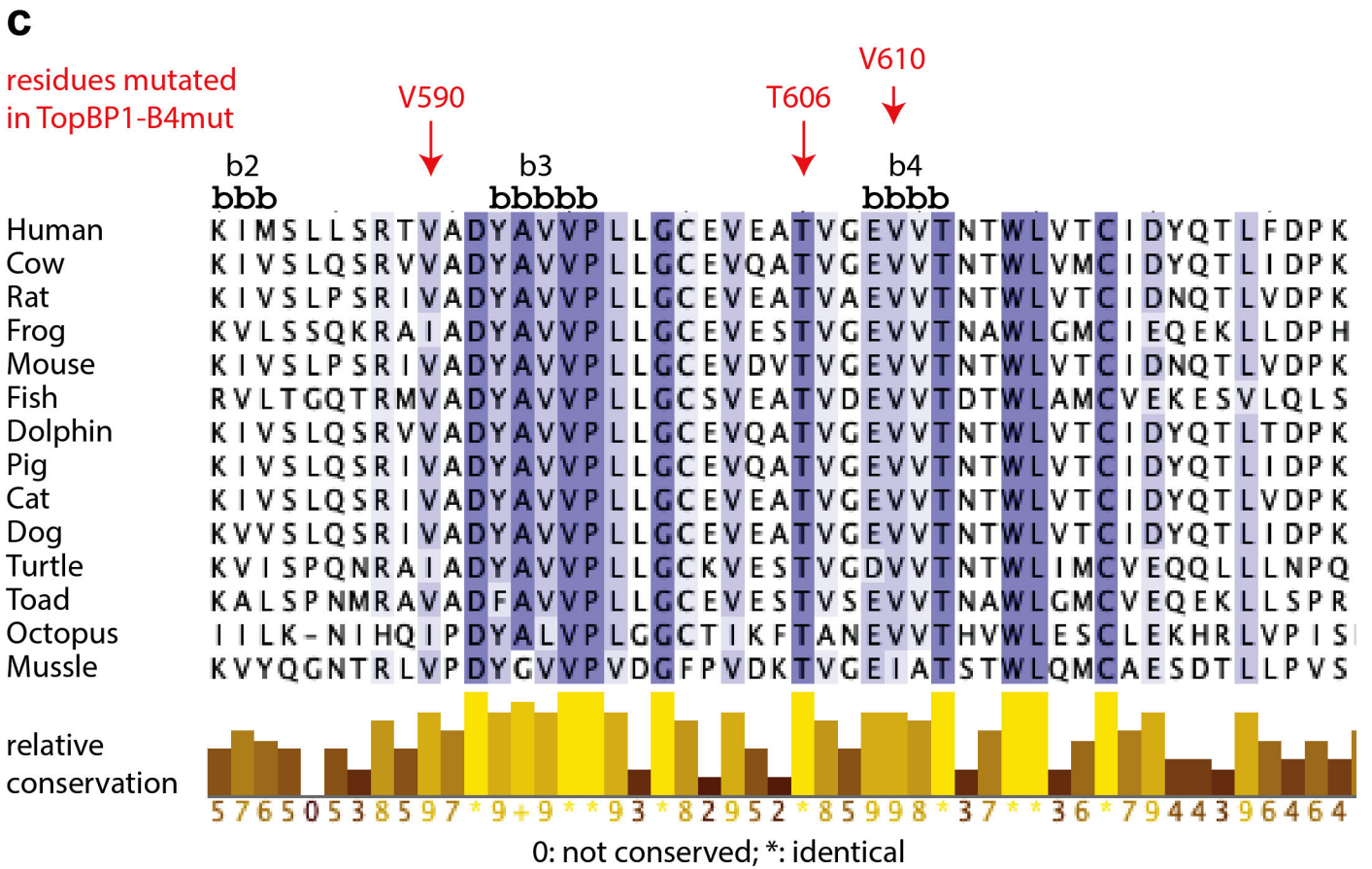
c
residues mutated
in TopBP1-B4mut
V590
T606
V610
b2
b3
b4
Human KIMSLLSRTVADYAVVPLLGCEVEATVGEVVTNTWLVTCIDYQTLFDPK
Cow KIVSLQSRVVADYAVVPLLGCEVQATVGEVVTNTWLVMCIDYQTLIDPK
Rat KIVSLPSRIVADYAVVPLLGCEVEATVAEVVTNTWLVTCIDNQTLVDPK
Frog KVLSSQKRAIADYAVVPLLGCEVESTVGEVVTNAWLGMCIEQEKLLDPH
Mouse KIVSLPSRIVADYAVVPLLGCEVDVTVGEVVTNTWLVTCIDNQTLVDPK
Fish RVLTGQTRMVADYAVVPLLGCSVEATVDEVVTDTWLAMCVEKESVLQLS
Dolphin KIVSLQSRVVADYAVVPLLGCEVQATVGEVVTNTWLVTCIDYQTLTDPK
Pig KIVSLQSRIVADYAVVPLLGCEVQATVGEVVTNTWLVTCIDYQTLIDPK
Cat KIVSLQSRIVADYAVVPLLGCEVEATVGEVVTNTWLVTCIDYQTLVDPK
Dog KVVSLQSRIVADYAVVPLLGCEVEATVGEVVTNTWLVTCIDYQTLIDPK
Turtle KVISPQNRAIADYAVVPLLGCKVESTVGDVVTNTWLIMCVEQQLLLNPQ
Toad KALSPNMRAVADFAVVPLLGCEVESTVSEVVTNAWLGMCVEQEKLLSPR
Octopus IILK-NIHQIPDYALVPLGGCTIKFTANEVVTHVWLESCLEKHRLVPIS
Mussle KVYQGNTRLVPDYGVVPVDGFPVDKTVGEIATSTWLQMCAESDTLLPVS
relative
conservation
5765053859 7*9+9**93*82952*85998*37**36*7944396464
0: not conserved; *: identical

Figure S6

a

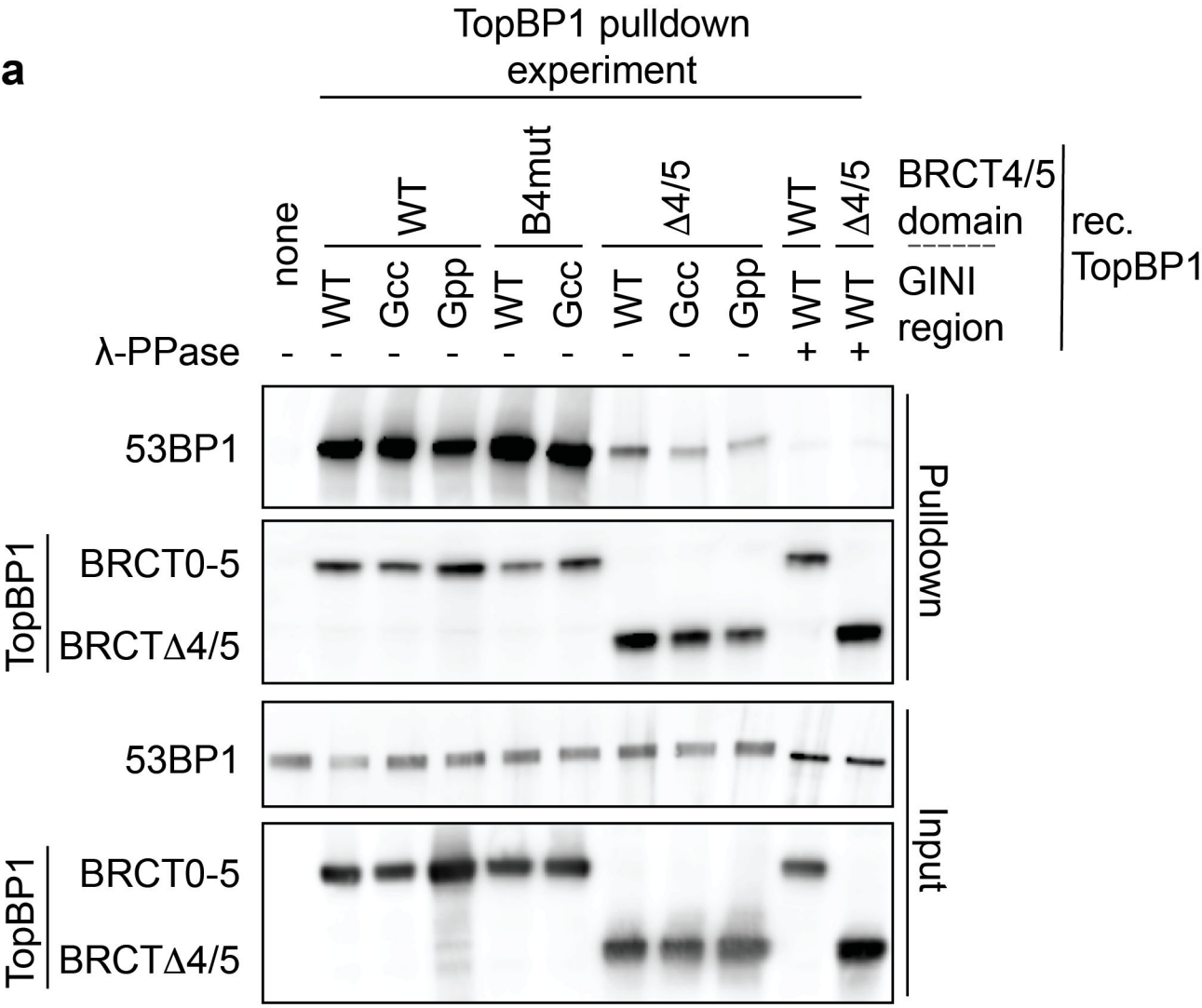
TopBP1 pulldown experiment
none
WT
Gcc
Gpp
B4mut
Δ4/5
BRCT4/5 domain
GINI region
rec. TopBP1
λ-PPase
53BP1
TopBP1
BRCT0-5
BRCTΔ4/5
Pulldown
Input

b

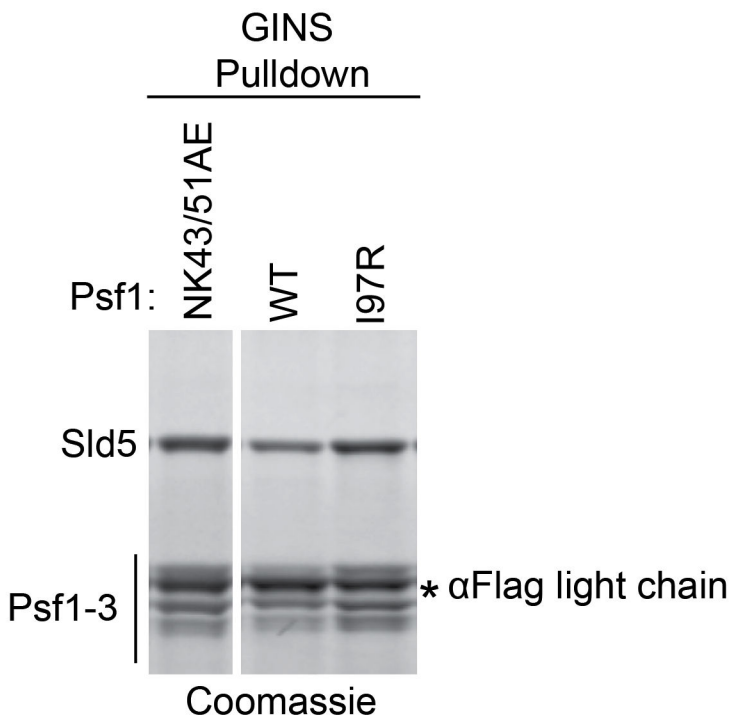
GINS Pulldown
Psf1:
NK43/51AE
WT
I97R
Sld5
Psf1-3
* αFlag light chain
Coomassie

Figure S7

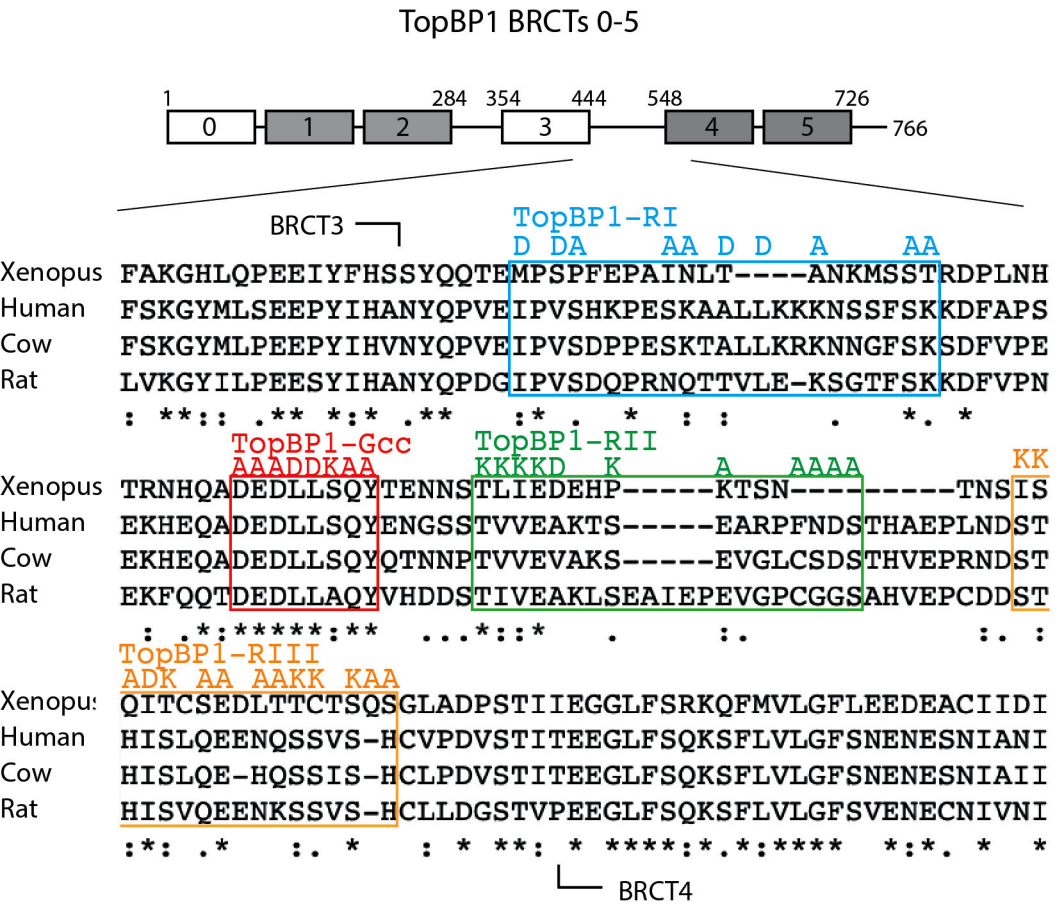
TopBP1 BRCTs 0-5
1
284
354
444
548
726
766
0
1
2
3
4
5
BRCT3
TopBP1-RI
D DA AA D D A AA
Xenopus FAKGHLQPEEIYFHSSYQQTEMPSPFEPAINLT----ANKMSSTRDPLNH
Human FSKGYMLSEEPYIHANYQPVEIPVSHKPESKAALLKKKNSSFSKKDFAPS
Cow FSKGYMLPEEPYIHVNYQPVEIPVSDPPESKTALLKRKNNGFSKSDFVPE
Rat LVKGYILPEESYIHANYQPDGIPVSDQPRNQTTVLE-KSGTFSKKDFVPN
: **:: .** *:* .** :* . * : : . *. *
TopBP1-Gcc
AAADDKAA
TopBP1-RII
KKKKD K A AAAA
KK
Xenopus TRNHQADEDLLSQYTENNSTLIEDEHP-----KTSN----------TNSIS
Human EKHEQADEDLLSQYENGSSTVVEAKTS-----EARPFNDSTHAEPLNDST
Cow EKHEQADEDLLSQYQTNNPTVVEVAKS-----EVGLCSDSTHVEPRNDST
Rat EKFQQTDEDLLAQYVHDDSTIVEAKLSEAIEPEVGPCGGSAHVEPCDDST
: .*:*****:** ...*::* . :. :. :
TopBP1-RIII
ADK AA AAKK KAA
Xenopus QITCSEDLTTCTSQSGLADPSTIIEGGLFSRKQFMVLGFLEEDEACIIDI
Human HISLQEENQSSVS-HCVPDVSTITEEGLFSQKSFLVLGFSNENESNIANI
Cow HISLQE-HQSSIS-HCLPDVSTITEEGLFSQKSFLVLGFSNENESNIAII
Rat HISVQEENKSSVS-HCLLDGSTVPEEGLFSQKSFLVLGFSVENECNIVNI
:*: .* :. * : * **: * ****:*.*:**** *:*. * *
BRCT4

Figure S8

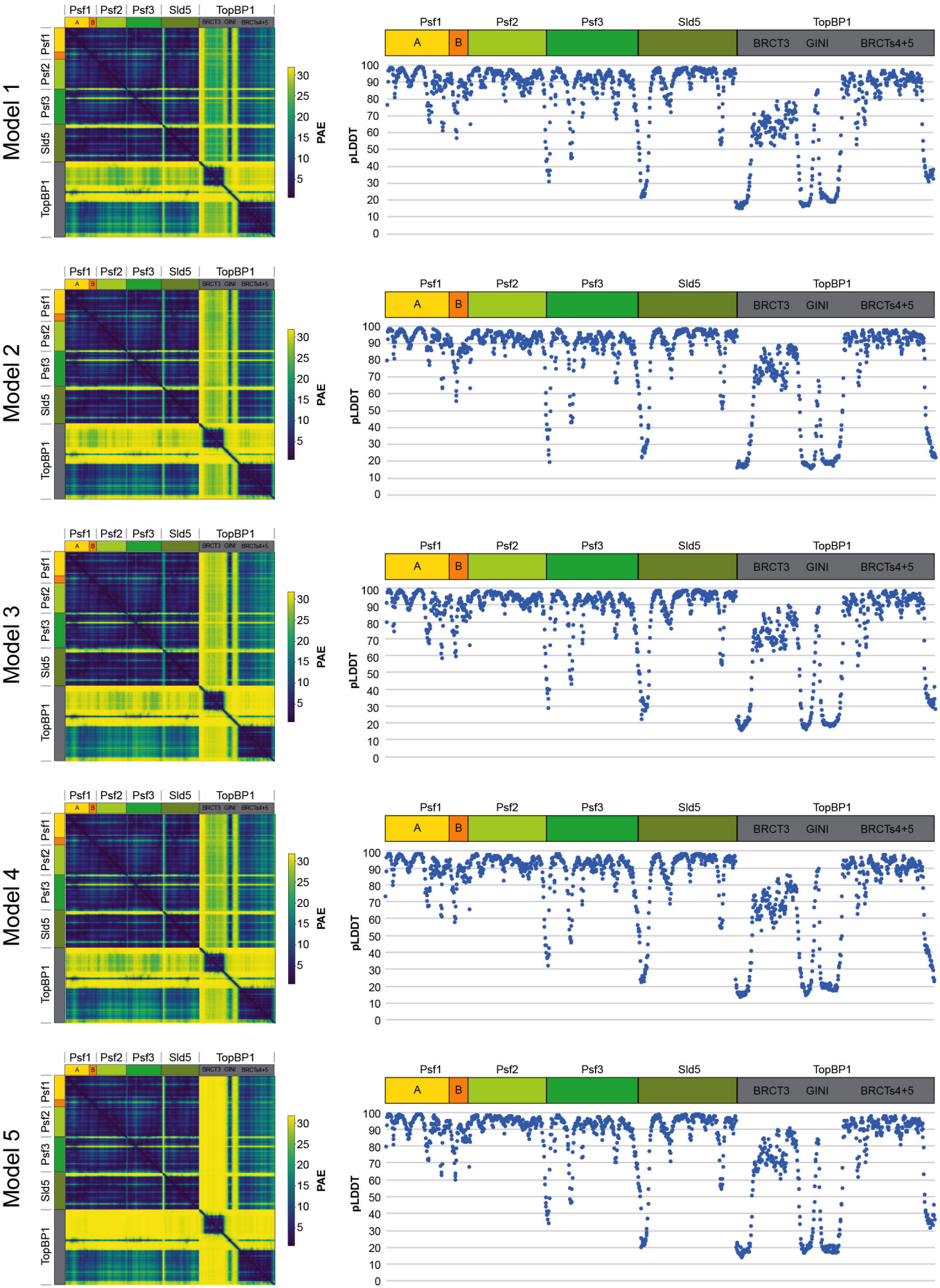
Model 1
Model 2
Model 3
Model 4
Model 5
Psf1
Psf2
Psf3
Sld5
TopBP1
A
B
BRCT3
GINI
BRCTs4+5
PAE
pLDDT

Figure S9

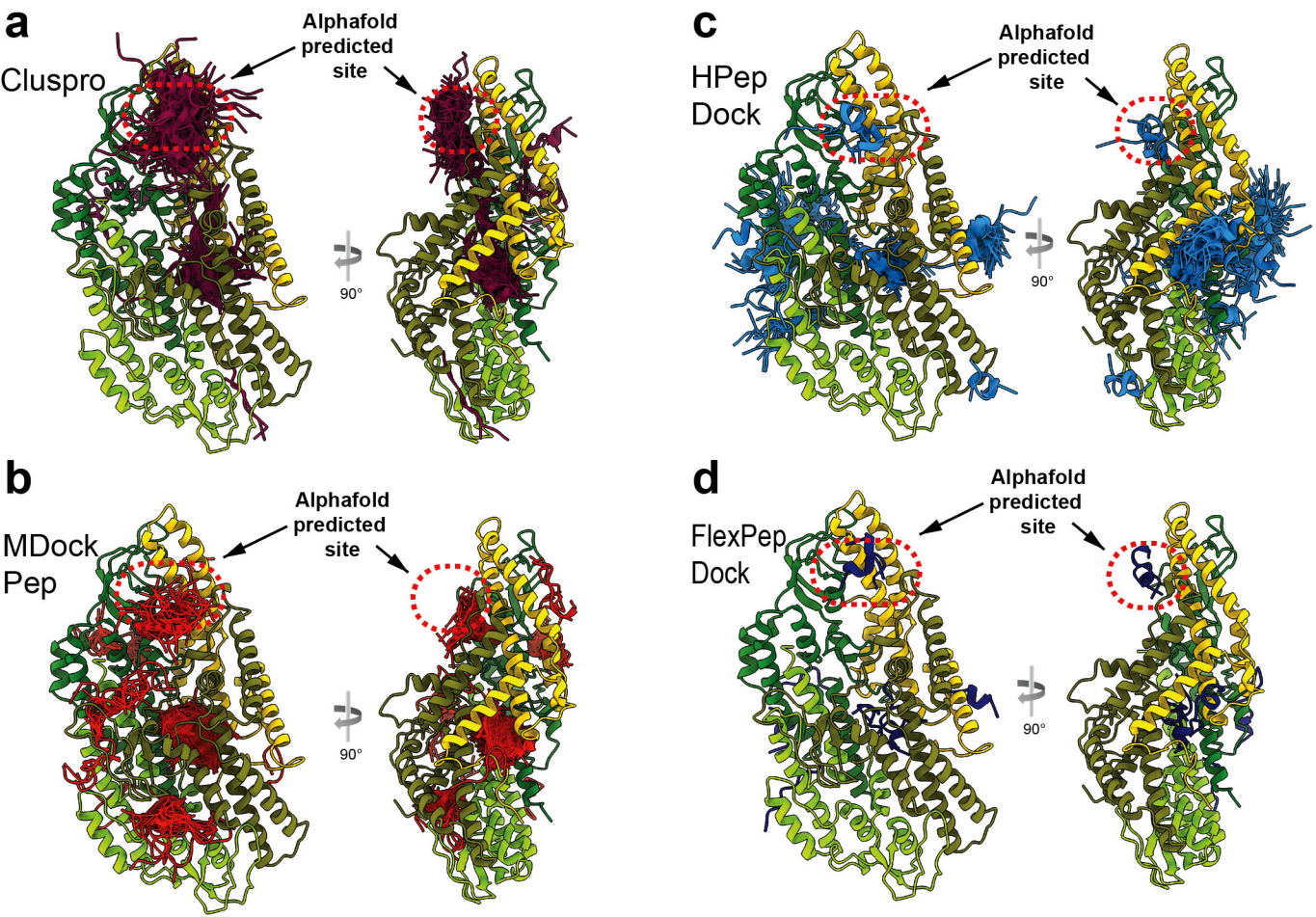
a
Cluspro
Alphafold predicted site
90°
b
MDock Pep
Alphafold predicted site
90°
c
HPep Dock
Alphafold predicted site
90°
d
FlexPep Dock
Alphafold predicted site
90°

Figure S10

a

TopBP1-GINS BS3 crosslinks; in solution

TopBP1-GINS BS3 crosslinks; gel-extracted

(i) GINI core region crosslinks

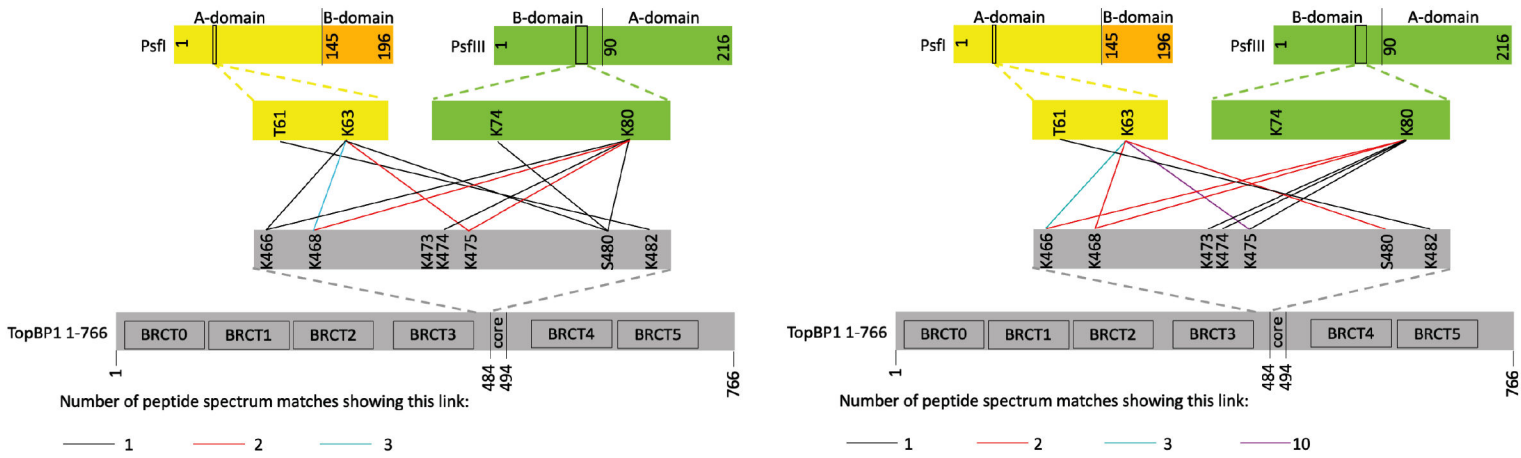

(ii) All inter-protein crosslinks

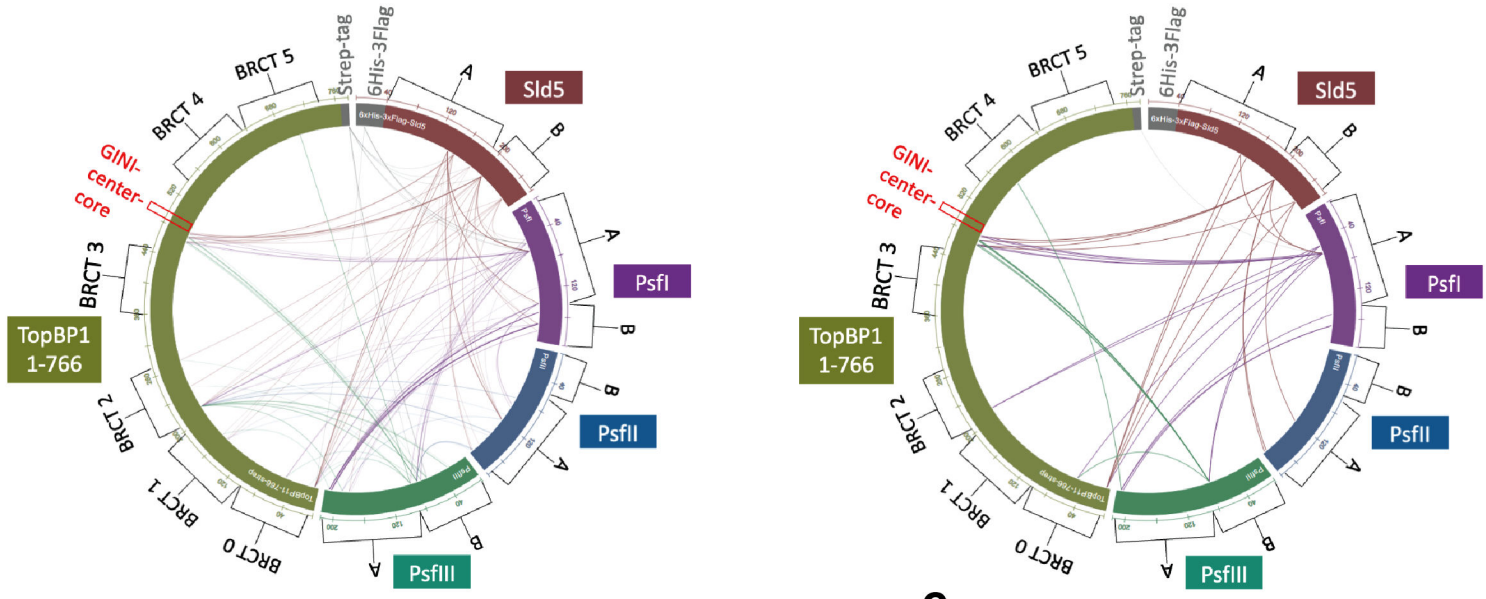

b

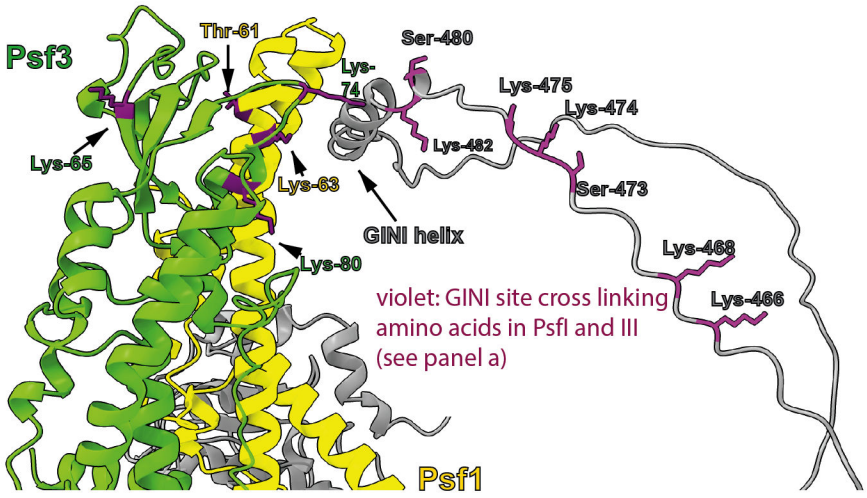

c

violet: Sld5 residues crosslinking with the GINI helix regions

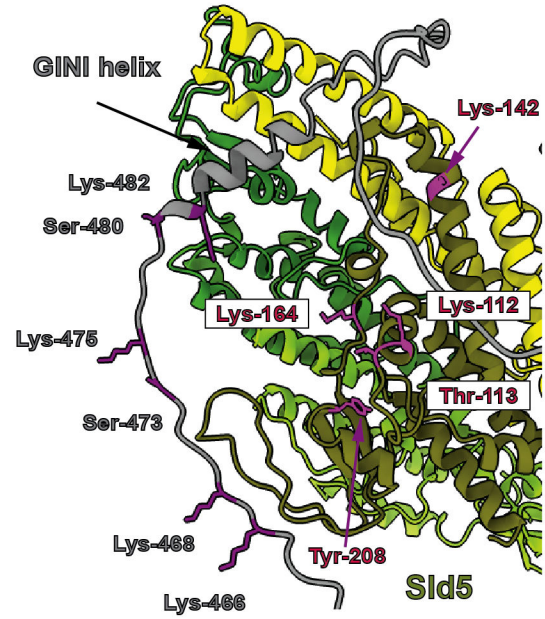

Figure S11

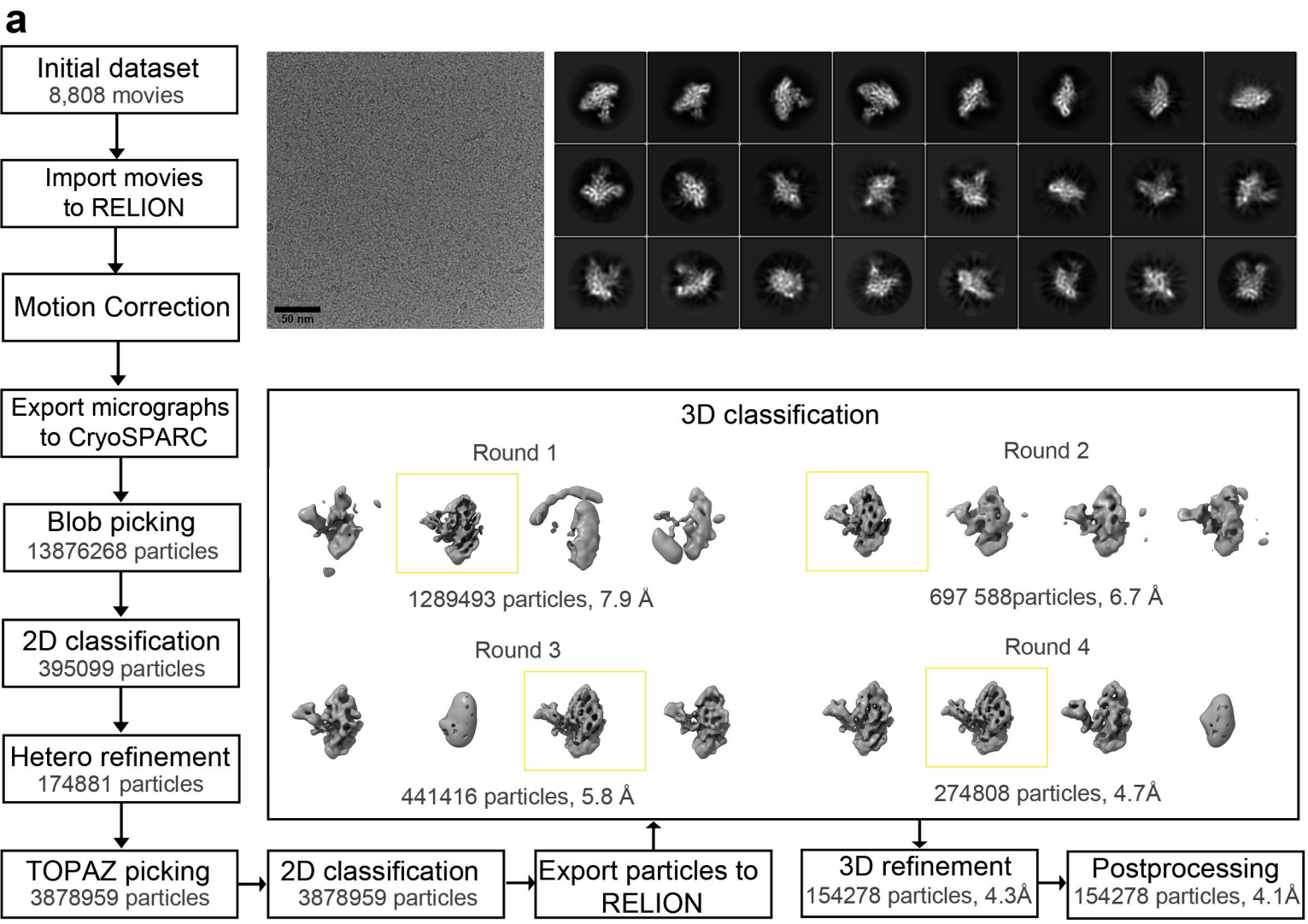
a
Initial dataset
8,808 movies
Import movies to RELION
Motion Correction
Export micrographs to CryoSPARC
Blob picking
13876268 particles
2D classification
395099 particles
Hetero refinement
174881 particles
TOPAZ picking
3878959 particles
2D classification
3878959 particles
Export particles to RELION
3D refinement
154278 particles, 4.3Å
Postprocessing
154278 particles, 4.1Å
50 nm
3D classification
Round 1
1289493 particles, 7.9 Å
Round 2
697 588particles, 6.7 Å
Round 3
441416 particles, 5.8 Å
Round 4
274808 particles, 4.7Å

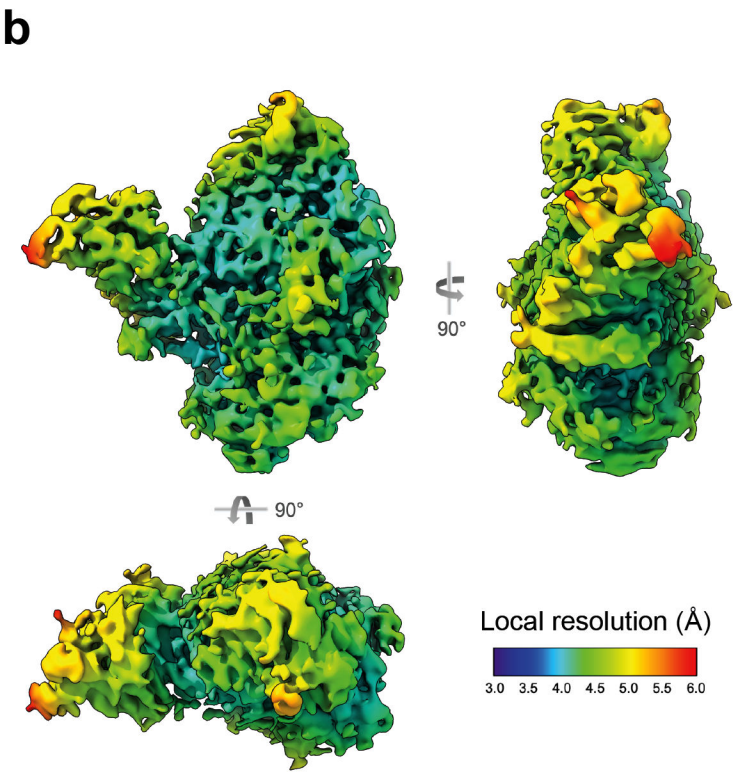
b
90°
90°
Local resolution (Å)
3.0 3.5 4.0 4.5 5.0 5.5 6.0

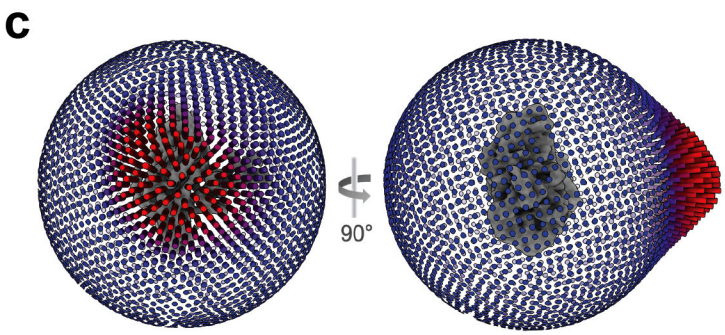
c
90°

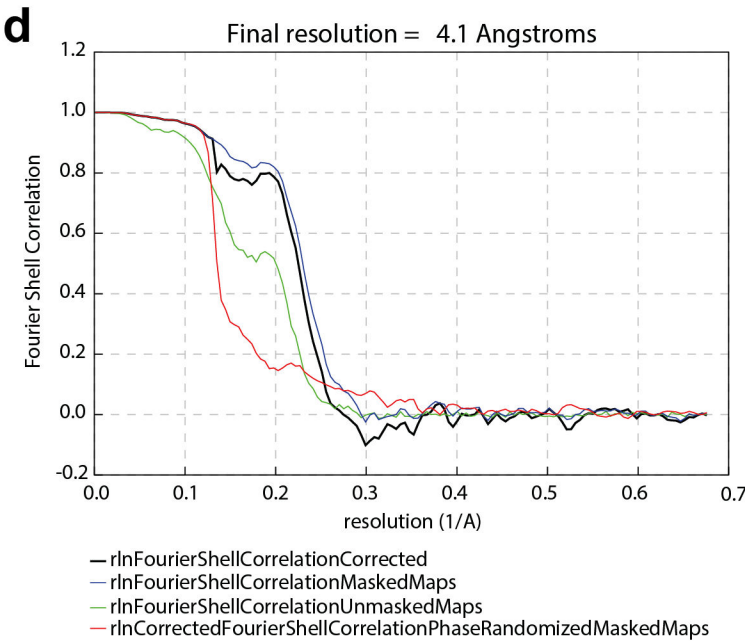
d
Final resolution = 4.1 Angstroms
Fourier Shell Correlation
resolution (1/A)
1.2
1.0
0.8
0.6
0.4
0.2
0.0
-0.2
0.0 0.1 0.2 0.3 0.4 0.5 0.6 0.7
rlnFourierShellCorrelationCorrected
rlnFourierShellCorrelationMaskedMaps
rlnFourierShellCorrelationUnmaskedMaps
rlnCorrectedFourierShellCorrelationPhaseRandomizedMaskedMaps

Figure S12

a

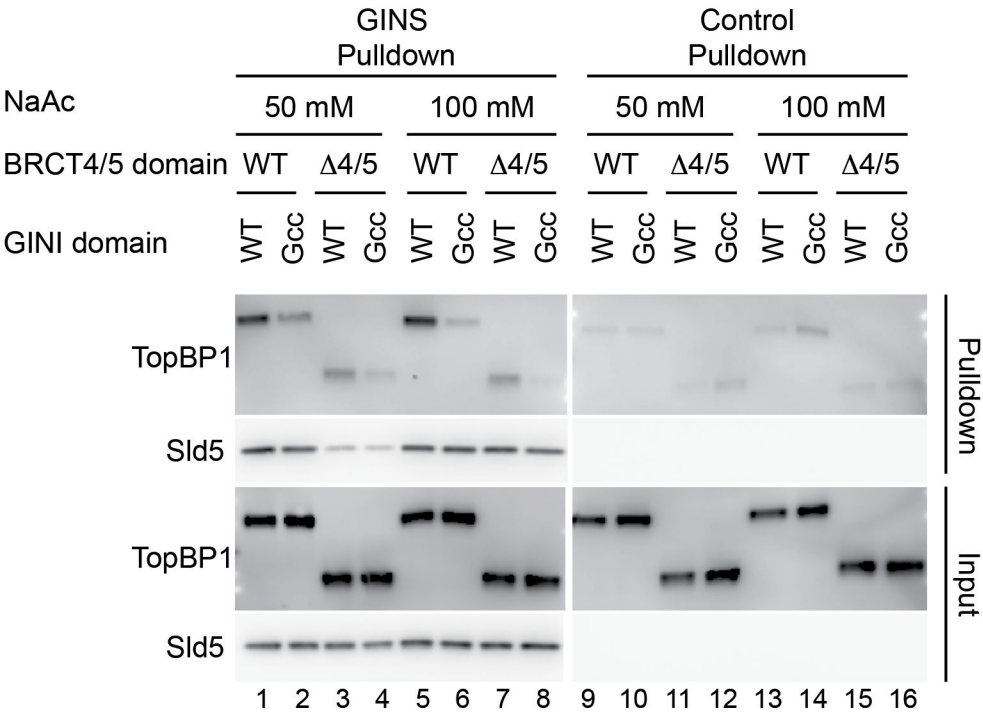

b

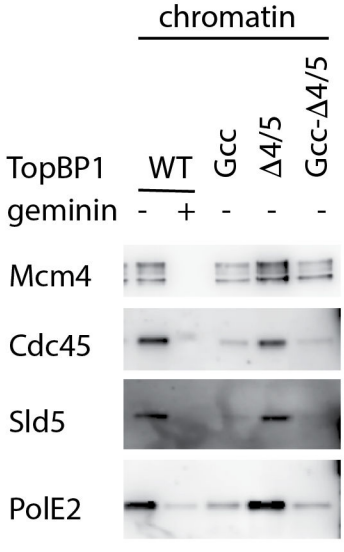

Figure S13

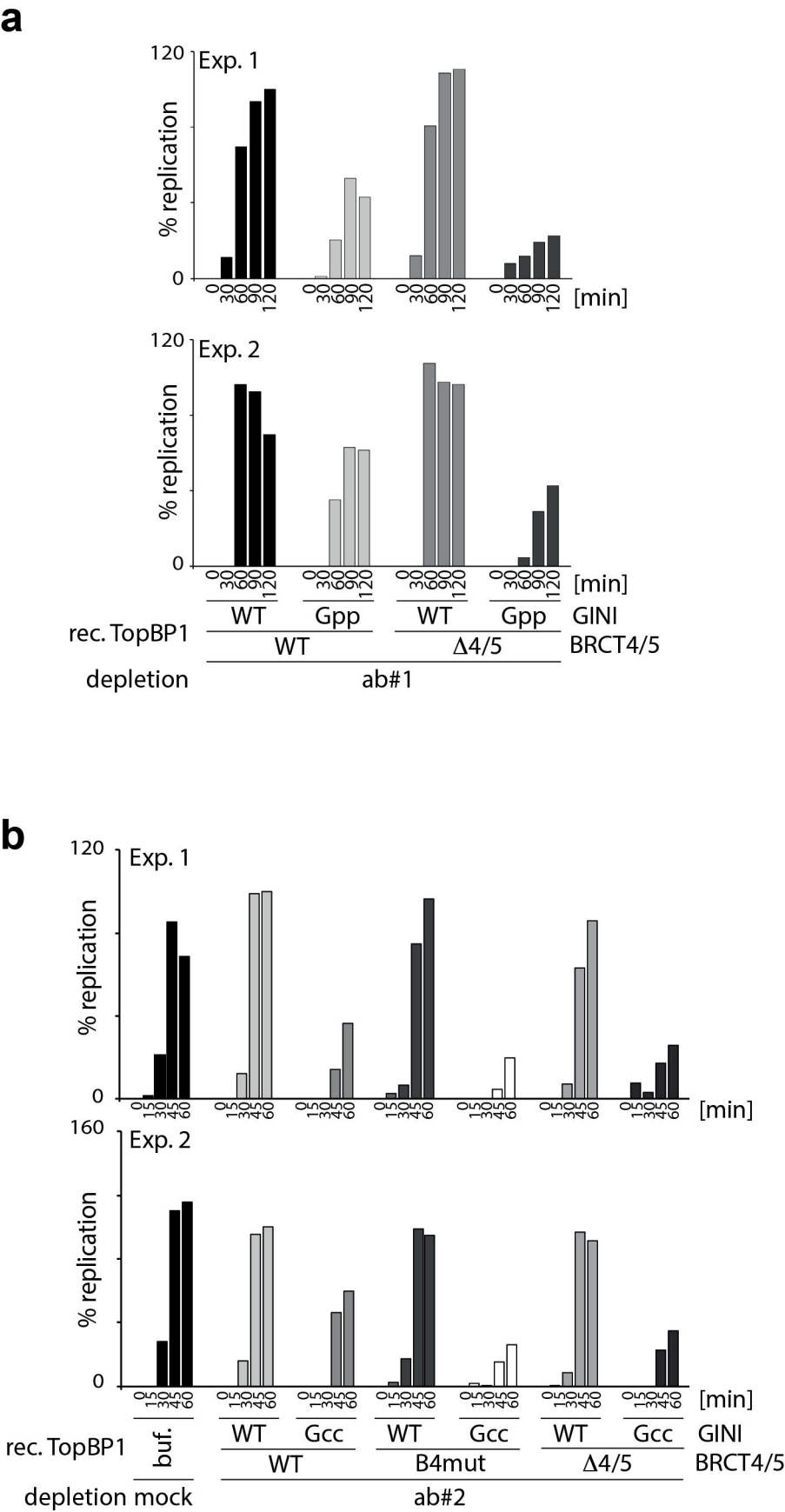
a
Exp. 1
% replication
120
0
0 30 60 90 120
[min]
Exp. 2
WT
Gpp
GINI
rec. TopBP1
BRCT4/5
Δ4/5
depletion
ab#1
b
0 15 30 45 60
160
buf.
Gcc
B4mut
mock
ab#2

Figure 14

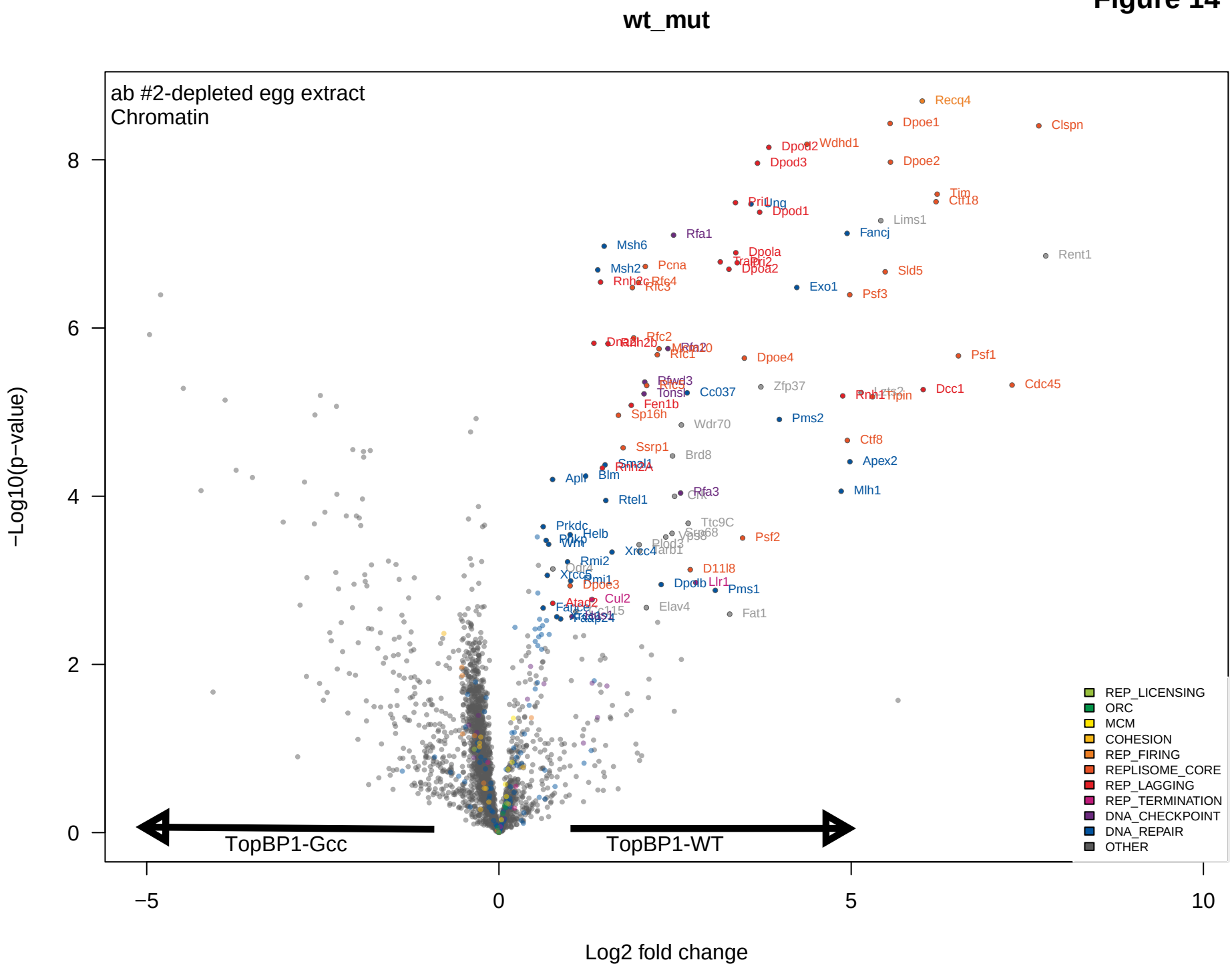
wt_mut
ab #2-depleted egg extract
Chromatin
−Log10(p−value)
Log2 fold change
TopBP1-Gcc
TopBP1-WT
REP_LICENSING
ORC
MCM
COHESION
REP_FIRING
REPLISOME_CORE
REP_LAGGING
REP_TERMINATION
DNA_CHECKPOINT
DNA_REPAIR
OTHER

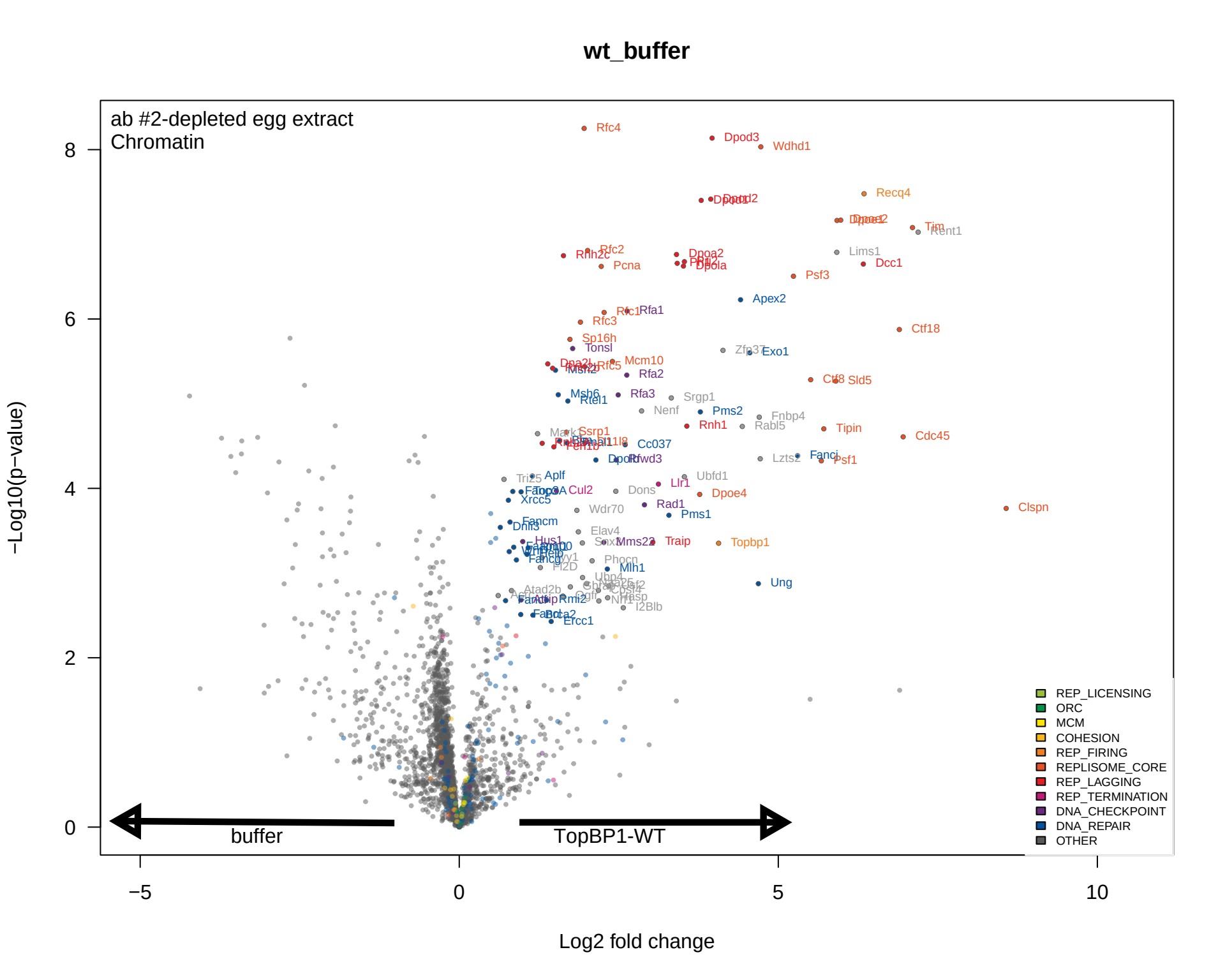
wt_buffer
ab #2-depleted egg extract
Chromatin
−Log10(p−value)
Log2 fold change
buffer
TopBP1-WT
REP_LICENSING
ORC
MCM
COHESION
REP_FIRING
REPLISOME_CORE
REP_LAGGING
REP_TERMINATION
DNA_CHECKPOINT
DNA_REPAIR
OTHER

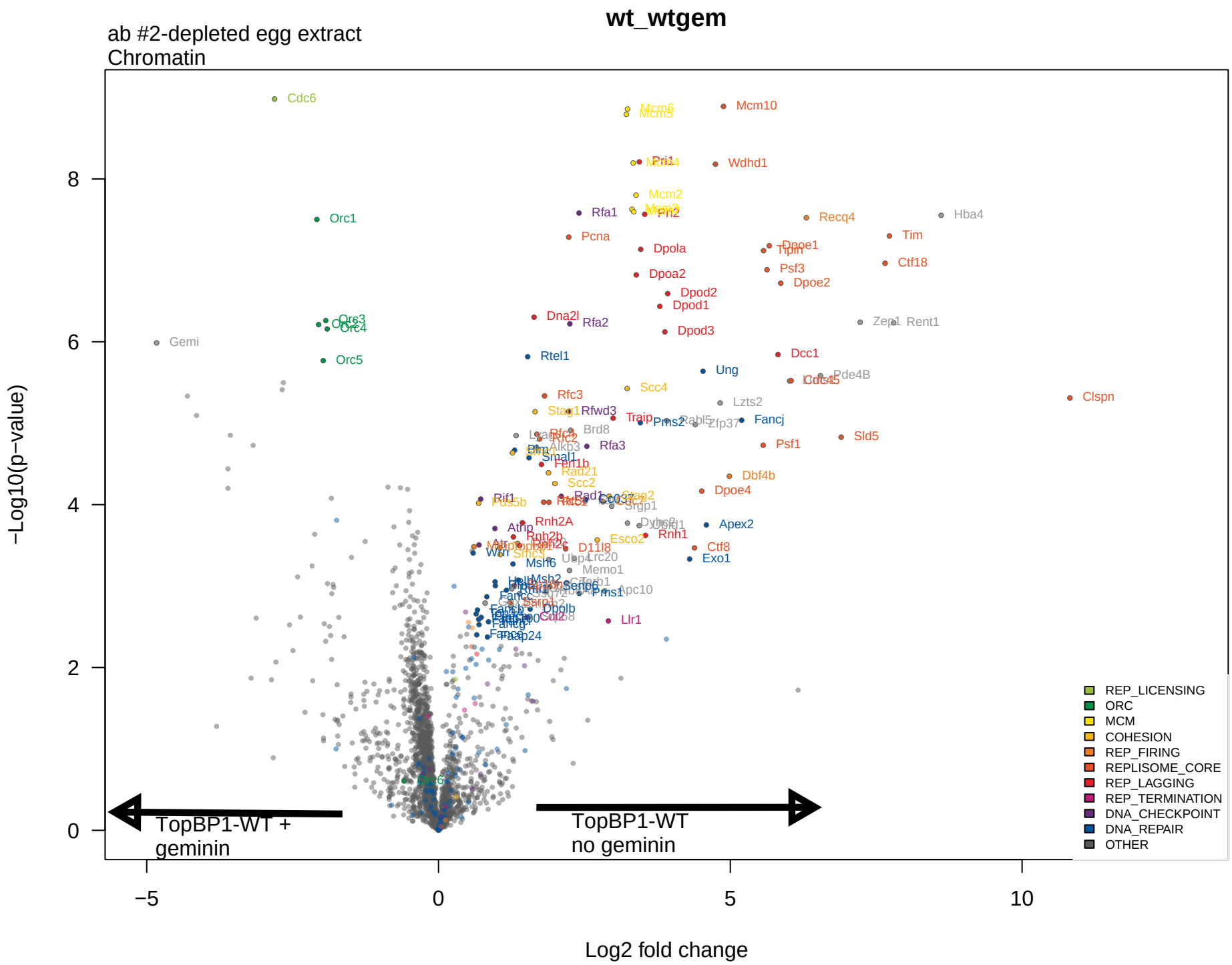
wt_wtgem
ab #2-depleted egg extract
Chromatin
−Log10(p−value)
Log2 fold change
TopBP1-WT +
geminin
TopBP1-WT
no geminin
REP_LICENSING
ORC
MCM
COHESION
REP_FIRING
REPLISOME_CORE
REP_LAGGING
REP_TERMINATION
DNA_CHECKPOINT
DNA_REPAIR
OTHER

Figure S15

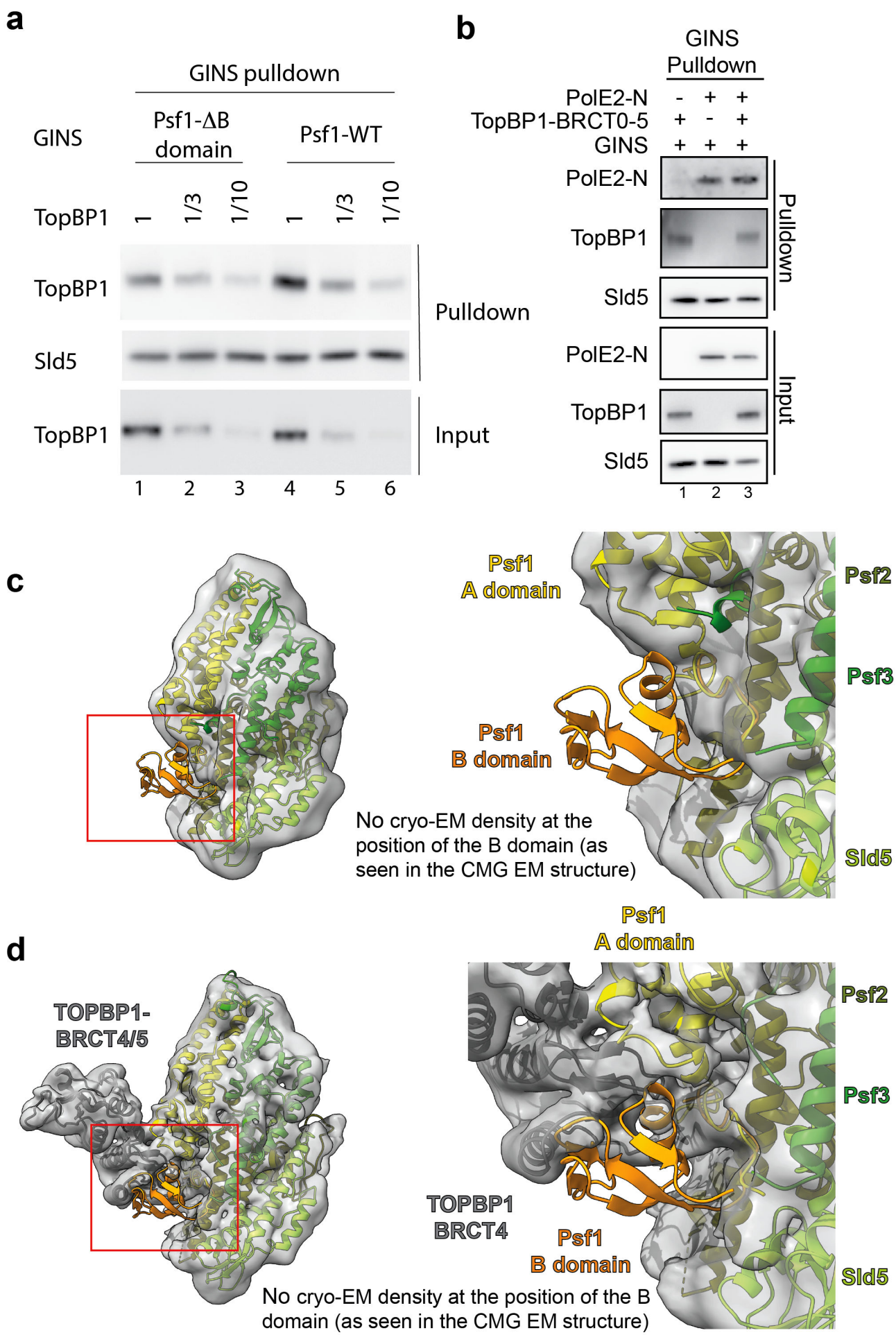
a
GINS pulldown
GINS
Psf1-ΔB domain
Psf1-WT
TopBP1
1
1/3
1/10
1
1/3
1/10
TopBP1
Sld5
Pulldown
TopBP1
Input
1 2 3 4 5 6
b
GINS Pulldown
PolE2-N - + +
TopBP1-BRCT0-5 + - +
GINS + + +
PolE2-N
TopBP1
Sld5
Pulldown
PolE2-N
TopBP1
Sld5
Input
1 2 3
c
Psf1 A domain
Psf2
Psf3
Psf1 B domain
Sld5
No cryo-EM density at the position of the B domain (as seen in the CMG EM structure)
d
TOPBP1-BRCT4/5
Psf1 A domain
Psf2
Psf3
TOPBP1 BRCT4
Psf1 B domain
Sld5
No cryo-EM density at the position of the B domain (as seen in the CMG EM structure)

Figure S16

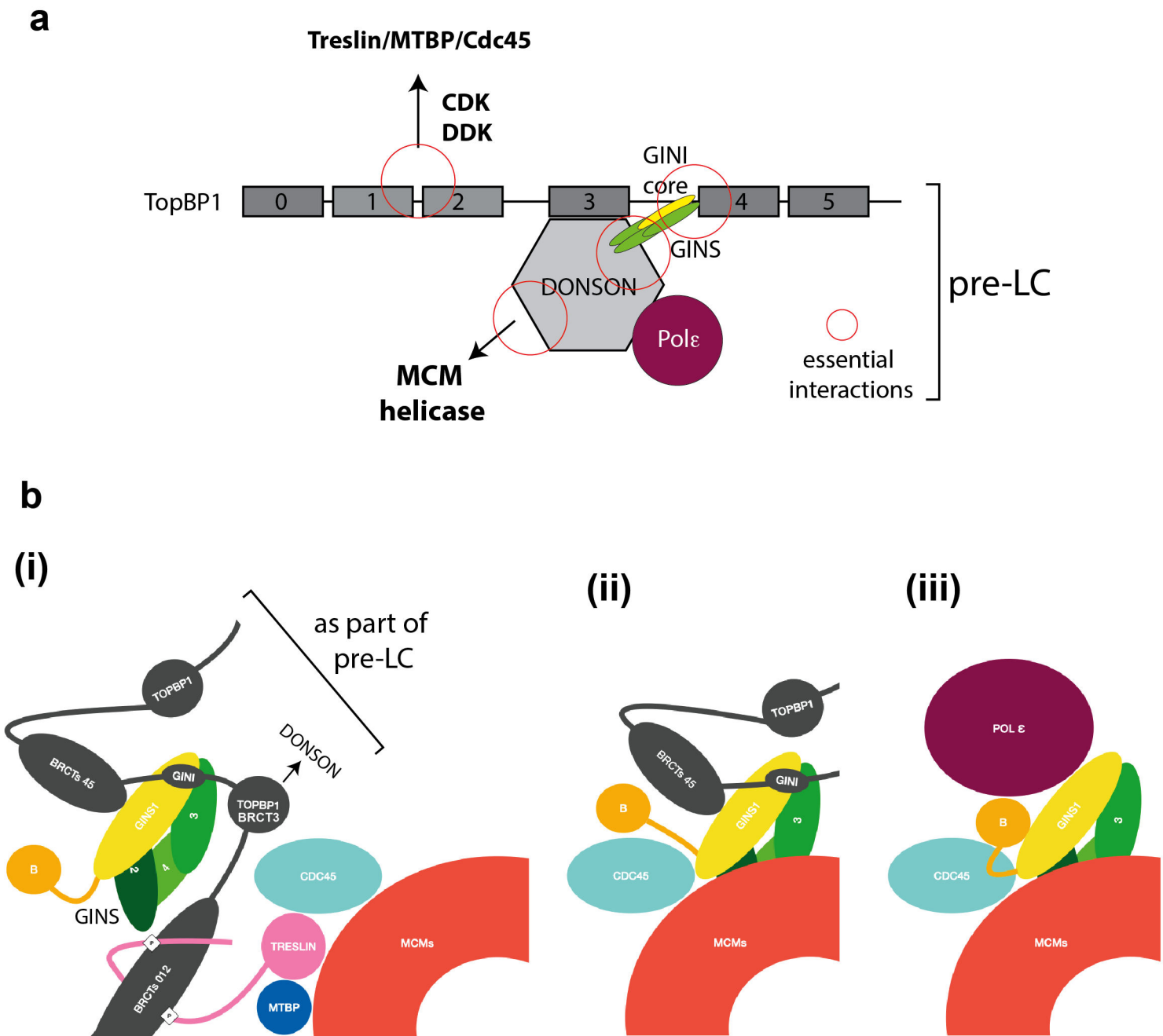
a
Treslin/MTBP/Cdc45
CDK
DDK
GINI
core
TopBP1
0
1
2
3
4
5
GINS
DONSON
Polε
MCM
helicase
pre-LC
essential
interactions
b
(i)
(ii)
(iii)
as part of
pre-LC
TOPBP1
BRCTs 45
GINI
GINS1
3
2
4
B
GINS
TOPBP1
BRCT3
DONSON
CDC45
TRESLIN
MTBP
BRCTs 012
MCMs
POL ε